PRECISION MEASUREMENT OF QUASI-ELASTIC TRANSVERSE AND LONGITUDINAL RESPONSE FUNCTIONS IN THE RANGE 0.55 GeV/c$\leq|\ \overrightarrow{q}\ |\leq$1.0 GeV/c

---

A Dissertation
Submitted to
the Temple University Graduate Board

In Partial Fulfillment
of the Requirements for the Degree
DOCTOR OF PHILOSOPHY

---

by
Hamza Atac
December 2017

Examining Committee Members:

Zein-Eddine Meziani, Department of Physics, Advisory Chair
Nikolaos Sparveris, Department of Physics
Andreas Metz, Department of Physics
Jian-Ping Chen, External Member, Thomas Jefferson National Accelerator Facility

ABSTRACT

The Coulomb Sum is defined by the quasi-elastic nucleon knock-out process and it is the integration of the longitudinal response function over the energy loss of the incident electron. The Coulomb sum goes to the total charge at large q. The existing measurements of the Coulomb Sum Rule show disagreement with the theoretical calculations for the medium and heavy nuclei. To find the reason behind the disagreement might answer the question of whether the properties of the nucleons are affected by the nuclear medium or not. In order to determine the Coulomb Sum in nuclei, a precision measurement of inclusive electron scattering in the quasi-elastic region was performed at the Thomas Jefferson National Accelerator Facility. Incident electrons with energies ranging from 0.4 GeV to 4 GeV scattered off ^{4}He,^{12}C,^{56}Fe and ^{208}Pb nuclei at four scattering angles $(15^{\circ}, 60^{\circ}, 90^{\circ}, 120^{\circ})$ and scattered energies ranging from 0.1 GeV to 4 GeV. The Born cross sections were extracted for the Left High Resolution Spectrometer (LHRS) and the Right High Resolution Spectrometer ^{56}Fe data. The Rosenbluth separation was performed to extract the transverse and longitudinal response functions at 650 MeV three-momentum transfer. The preliminary results of the longitudinal and transverse functions were extracted for ^{56}Fe target at 650 MeV three-momentum transfer.

DEDICATION

to my parents and Maggie

ACKNOWLEDGEMENTS

First I would like to thank my advisor Dr.Zein-Eddine Meziani for giving me the oppurtinity to work in his research group. His great experience and knowledge gave me great motivation and guidance to become a nuclear physicist. Also, his great personality and love in physics inspired me.

I would like to give special thanks to Dr.Michael Paolone who advised me and helped me through every step of the analysis. His deep knowledge in physics and programming helped me learn the analysis procedure faster. His easy-going and friendly attitude made this project enjoyable.

I want to thank the spokespeople of the experiment Dr.Seonho Choi, Dr.Jian-Ping Chen, Dr.Alexandre Camsonne and Dr.Zein-Eddine Meziani for their advice and guidance during the weekly analysis meetings. I learnt so many things from the discussions we had during these meetings.

I would like to specially thank Dr.David Flay who helped with the analysis and gave me many suggestions. I want to thank the other students, Dr.Yoomin Oh, Dr.Huan Yao, Kai Jin and Yan Huang who were working on this project with me. I also want to thank Dr.Whitney R. Armstrong, Dr.Sylvester Joosten and Dr.Nikolaos Sparveris for their great advice.

I also want to thank to all people who contributed to the E05-110 experiment. I would like to thank to the Department of Energy (DOE) for supporting me through the grant DE-FG02-94ER40844. I would like to thank to the Turkish Ministry of Education (MEB) for giving me the oppurtinity to study in USA.

I owe special thanks to Dr.Ugur Cevik, Dr.Nedim Alev and Dr.Nevzat Yigit for their support. I would not be able to study in USA without their help. I wish to take a chance to thank my friend Dr.Ismail Bilgin for his support.

I would like to specially thank to Myers family for supporting me. I am grateful to my family, especially to my parents, my brothers and sister. Finally, I am grateful to my fiance Maggie who supported me at every steps of my PhD.

CONTENTS

LIST OF FIGURES

LIST OF TABLES

CHAPTER 1

INTRODUCTION

1.1 Brief History of Nuclear Physics

Physicists have been investigating the most fundamental constituents of matter for a long time in order to understand the universe better. In the 1800's it was believed that atoms were the most fundamental blocks of matter. Later in 1897, the discovery of the negatively charged particle, the electron, by J.J Thompson changed physicists' views of the atom. In 1911, Ernest Rutherford along with Hans Geiger and Ernest Marsden carried out the Geiger-Marsden experiment, which led Rutherford to discover the atomic *nucleus*. By deflecting alpha particles passing through a thin gold foil, they were able to find that the atom was made of mostly empty space with a dense core in the center, called *the nucleus*. This made a big impact on the scientific community and led to more investigations on whether the nucleus is made up of any smaller particles. Rutherford continued his experiments, and he discovered the proton in 1917. In 1932, James Chadwick who worked with Rutherford, discovered the neutron. Today, protons and neutrons are called *nucleons*.

In late 1930s, the neutron was found to have a magnetic moment [1]. The discovery of the neutron's magnetic moment indicated that the neutron was not an elementary particle. As the experiments got more sophisticated and with the higher energy probe particles be-

came available, physicists were able to study the inner structure of nucleons. In 1964, the quark model was proposed by Murray Gell-Mann and George Zweig. According to this model, nucleons are made up of point like particles called *quarks* [2, 3]. The matter and its constituents are summarized in the Figure 1.1. In the 1980s, all that was known about fundamental particles combined in the Standart Model. The standart Model is not complete today, but it is the best explanation of the most fundamental particles and interactions between them.

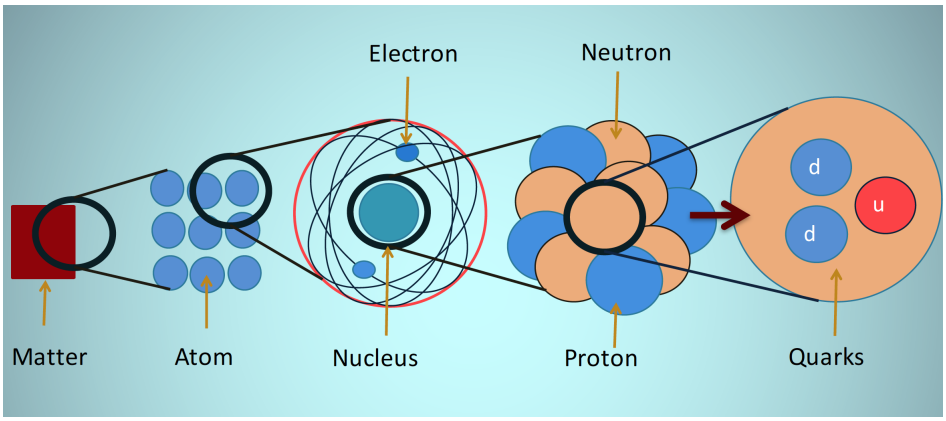

Figure 1.1: Constituents of Matter. Figure adapted from TEDxCERN.

1.2 Studying Nuclear Structure With Electrons

In nuclear physics, nucleons are the main subject of interest. To understand the nuclei better, we first need to study nucleons and their interactions in the nuclei.

Electrons can be used as a probe to study the nuclear structure and has advantages over hadrons [4]. The electron is a point like particle that interacts only through electromagnetic and weak interactions. Since, the interaction between electron and a target nucleus is weak ($\alpha = 1/137$), it doesn't disturb the system. The electromagnetic interaction is also well understood through Quantum Electrodynamics (QED). Therefore this makes the electron an ideal probe to study the nuclear structure. The most precise nuclear form factor measurements come from the electron scattering experiments [5–8].

In electron scattering experiments, the variation of ω energy transfer, q three momentum transfer and the polarization of the virtual photon can be achieved independently by changing the kinematics of the electron. In addition to their Coulomb interaction, they can also have magnetic interaction with target. Moreover, electrons are also easy to produce and accelerate in the laboratory.

Electron scattering experiments have been used widely as a tool to study the nuclear structure since the 1950s. The first electron scattering experiment was performed at the University of Illionis in 1951 at an incident energy of 15.7 MeV. In 1953, experiments with higher energy electrons (up to 190 MeV) were carried out at Stanford University and the University of Michigan [9]. In 1961, Robert Hofstadter won the Nobel Prize for his pioneering studies of electron scattering in atomic nuclei [10].

Figure 1.2 shows first high energy electron scattering equipment used at Stanford University.

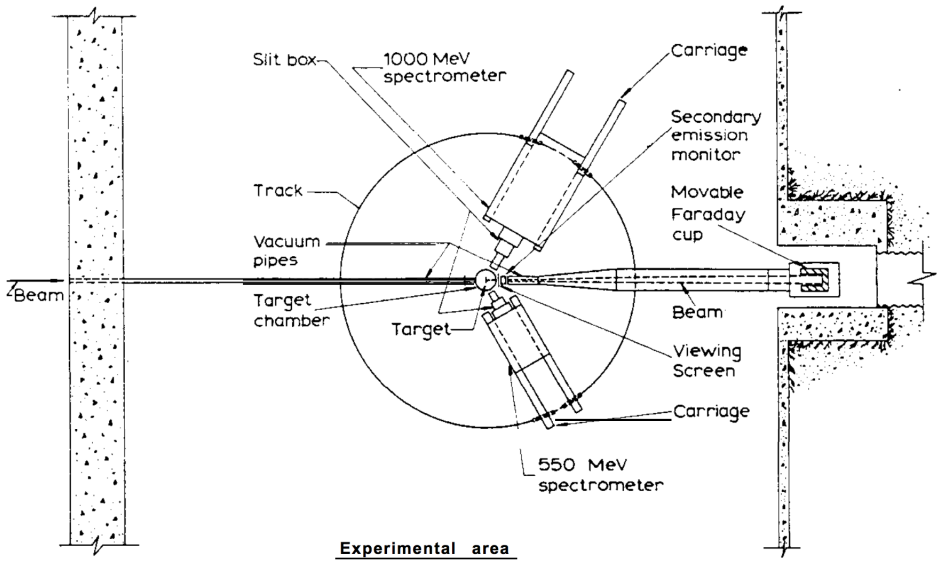

Figure 1.2: First high-energy electron scattering equipment. [9].

When considering a scattering experiment in which an electron with inital momentum $\overrightarrow{P_i}$ scatters off target and the scattered electron measured at θ scattering angle with a final

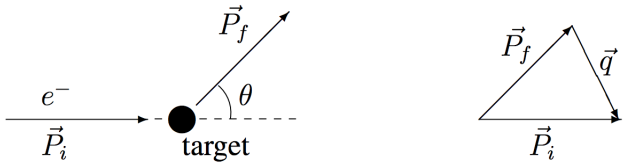

Figure 1.3: Scattering process of an electron off a target nucleus. [10].

momentum $\overrightarrow{P_f}$, the momentum transfer of the electron can be defined as $\overrightarrow{q} = \overrightarrow{P_i} - \overrightarrow{P_f}$.

In this process the differential cross section $\frac{d\sigma}{d\Omega}$ is usually the most important quantity . The Born approximation and Fermi's Golden Rule can be used to formulate this differential cross section.

This differential cross section $\frac{d\sigma}{d\Omega}$, was first formulated by Rutherford for non-relativistic point like spin-less charged particles. Rutherford's formula is shown in Equation 1.1.

$$\frac{d\sigma}{d\Omega}_{Rutherford} = \frac{\alpha^2}{16E^2 Sin^4(\frac{\theta}{2})}, \tag{1.1}$$

Later, Mott rederived this formula by considering that electrons are relativistic and have spin $1/2$ but the nucleus is spin-less. The Mott differential cross section is shown below in Equation 1.2:

$$\frac{d\sigma}{d\Omega}_{Mott} = \frac{\alpha^2 Cos^2(\frac{\theta}{2})}{4E^2 Sin^4(\frac{\theta}{2})}, \tag{1.2}$$

The Mott differential cross section is formulated for point like particles. When an extended charge distribution (nucleus) is considered as the scattering target, the differential cross section becomes:

$$\frac{d\sigma}{d\Omega} = \frac{\alpha^2 Cos^2(\frac{\theta}{2})}{4E^2 Sin^4(\frac{\theta}{2})} \left|F(q^2)\right|^2 \tag{1.3}$$

$F(q^2)$ is known as the nuclear form factor, and it is a Fourier pair of electric charge.

The form factor is shown below in Equation 1.4:

$$F(q^2) = \int d^3r\rho(r).e^{iqr} \tag{1.4}$$

A more realistic description of the elastic scattering of an electron on a spin of $\frac{1}{2}$ hadron has to take into account the internal structure and the anomalous magnetic moment of the hadron. Equation 1.3 has to be modified by introducing electric and magnetic form factors representing the internal structure of the proton. This will yield the Rosenbluth formula [11]. The Rosenbluth formula [12] is shown in Equation 1.5.

$$\frac{d\sigma}{d\Omega} = \frac{d\sigma}{d\Omega}_{Rutherford}\frac{E'}{4E}(\frac{G_E^2+\tau G_M^2}{1+\tau}cos^2(\frac{\theta}{2})+2\tau G_M^2 sin^2(\frac{\theta}{2})) \tag{1.5}$$

$$\tau = \frac{Q^2}{2m_{p/n}^2} \tag{1.6}$$

G_E is the electric form factor and G_M is the magnetic form factor in this equation. The relation between G_E and G_M was extracted and formulated from experimental results (see Figure 1.4). G_E and G_M can be described approximately by dipole form in Equation 1.7.

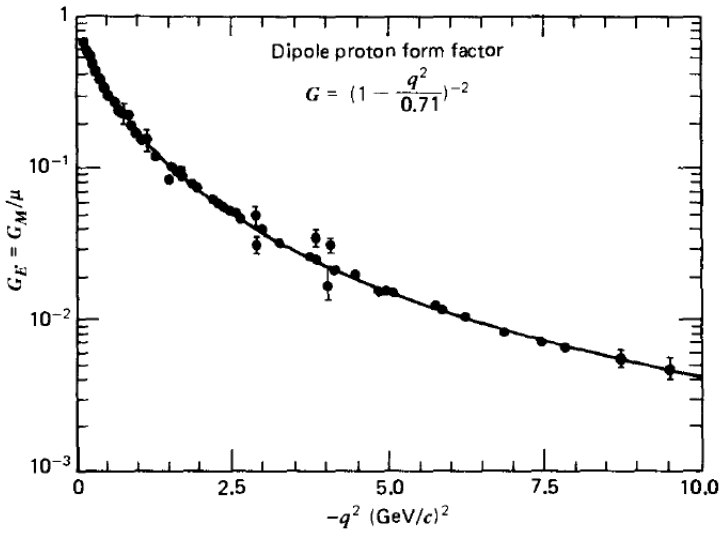

Figure 1.4: The proton form factors as a function of q^2. Figure from [13].

$$G_E = G_M/2.793 = \left[1 - (q^2/0.71GeV^2)\right]^{-2} \tag{1.7}$$

1.2.1 Quasi-elastic Electron Scattering

Different nuclear response structures can be observed in an inclusive electron scattering (see Figure 1.5). These structures depend on the energy transfer ω (the energy of the virtual photon). Therefore, the de Broglie wavelength of the virtual photon defines the structure type. Each structure represents a different region of the nucleus. At low energies, a virtual photon has a large wavelength and can not penetrate into the nucleus. Thus, it can be used to study the properties of the nucleus. As the energy transfer increases, the wavelength of the virtual photon becomes smaller and it can be used to study the inner structure of the nucleus (nucleons, quarks).

The energy wavelength relation can be seen in Equation 1.8 (Planck's Equation):

$$E = \frac{hc}{\lambda} \tag{1.8}$$

The first structure can be seen at the position of $\omega = Q^2/2M$ (Q is the four momentum transfer and M is the nucleus mass). This is a sharp peak due to the elastic scattering from the target nucleus. The energy loss of the electron is equal to the recoil energy of the nucleus [4]. When the energy loss gets larger than the recoil energy, the nucleus reaches an excited state, and peaks due to inelastic excitations can be observed.

When the energy loss is large enough to knock out a nucleon from the target nucleus, a broad peak due to quasi-elastic scattering can be seen. If the energy loss increases even more, the knocked out nucleon can be in a Δ resonance state. The Δ resonance peak is broader than the quasi-elastic peak. After the resonance region the deep inelastic region (DIS), a structureless continuum, comes. In the DIS region, the electron scatters off the constituent quarks of the nucleons. The DIS can be used to study quarks and gluons.

The quasi-elastic scattering on a nucleon is very similiar to the elastic scattering on a

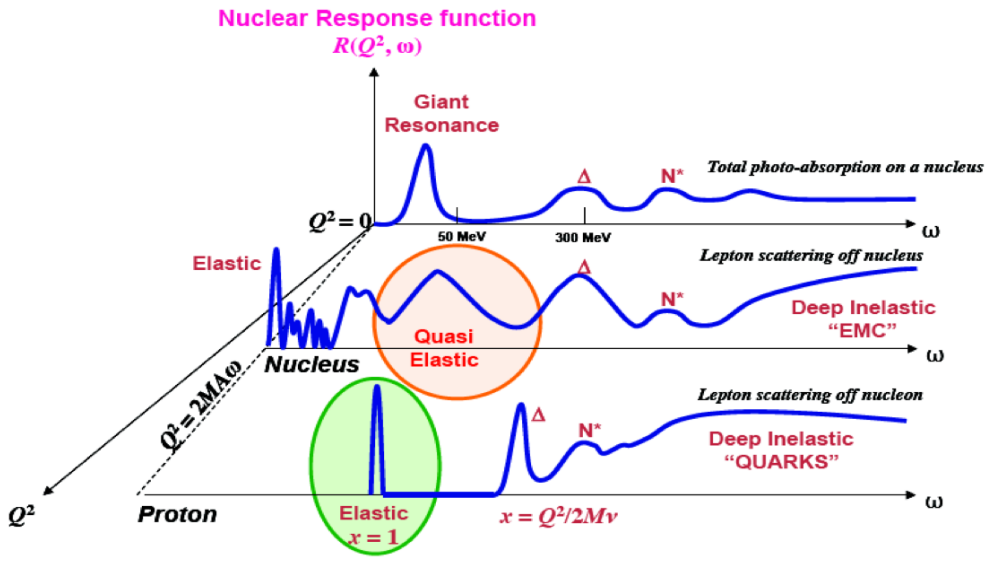

Figure 1.5: Nuclear Response Functions (illustration only) that can be seen in the scattering experiments.

nucleon. The elastic scattering on a nucleon can be observed at $\omega = Q^2/2M_N$ (M_N is the nucleon mass), and corresponds to an electron scattering from a free nucleon at rest. The quasi-elastic scattering is the elastic scattering of an electron from a nucleon in motion. The elastic scattering has a sharp peak while the quasi-elastic scattering has a shifted broad peak. The broadening in the quasi-elastic peak is due to the Fermi motion of the nucleon and the shift is due to the nuclear binding [14]. The width of the quasi-elastic peak can be used to measure the Fermi momentum of the nucleons k_F.

The inclusive quasi-elastic scattering is a great tool to study nucleons and the interaction between them. In the inclusive scattering, only the scattered electron is detected and the final hadronic state is un-measured. The inclusive scattering provides less specific information compared to the exclusive scattering which measures the knocked-out nucleon as well. The exclusive scattering gives an integral over all final states of the nucleon [14] [8].

1.2.1.1 Quasi-elastic Electron Scattering Kinematics and Rosenbluth Formula

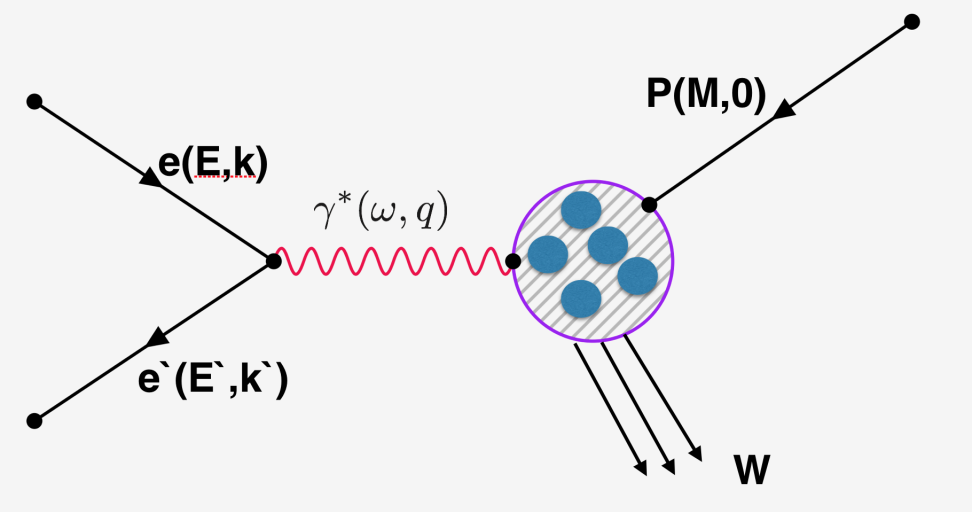

Figure 1.6: The inclusive quasi-elastic scattering diagram

In an inclusive unpolarized electron scattering process, an electron with the initial energy E scatters off a target nucleus at rest and the scattered electron is measured at θ scattering angle with E' energy (see Figure 1.6). The only quantity that is known about the target is the invarient mass W. The Rosenbluth formula for this process under the plane wave and the Born approximation can be written in terms of the structure functions W1 and W2 in Equation 1.9:

$$\frac{d\sigma}{d\Omega} = \frac{d\sigma}{d\Omega_{Mott}}\left[W_2(|q|,\omega) + 2W_1(|q|,\omega)tan^2(\frac{\theta}{2})\right] \tag{1.9}$$

The right side of this equation can also be re-written to separate contributions of longitudinally and transversely polarized virtual photons to the scattering processes [8]:

$$\frac{d\sigma}{d\Omega} = \left[\frac{Q^4}{\overrightarrow{q}^4}R_L(|\overrightarrow{q}|,\omega) + \frac{Q^2}{2\overrightarrow{q}^2\varepsilon}R_T(|\overrightarrow{q}|,\omega)\right] \tag{1.10}$$

The relation of R_L and R_T to W_1 and W_2 is given by:

$$R_T(|\overrightarrow{q}|) = 2W_1(|\overrightarrow{q}|) \tag{1.11}$$

and

$$\frac{Q^2}{|\overrightarrow{q}|^2}R_L(|\overrightarrow{q}|) = W_2(|\overrightarrow{q}|) - \frac{Q^2}{|\overrightarrow{q}|^2}W_1(|\overrightarrow{q}|) \tag{1.12}$$

$$W^2 = M_N^2 + 2M_N\omega - Q^2 \tag{1.13}$$

$$\begin{aligned} Q^2 &= \overrightarrow{q}^2 - \omega^2 \\ &= 4EE'Sin^2(\frac{\theta}{2}) \end{aligned} \tag{1.14}$$

where $\varepsilon = [1 + \frac{2\overrightarrow{q}^2}{Q^2}tan^2(\frac{\theta}{2})]^{-1}$ is the virtual photon polarization, R_L is the longitudinal response function and R_T is the transverse response function of the nucleus. In the plane wave aproximation, both incident and scattered electrons are considered plane waves. The Born aproximation assumes that a virtual photon is exchanged between the incident electron and the target particle.

R_L measures the nuclear charge density inside the nucleus and R_T measures the magnetic component of the nucleon electromagnetic current of the nucleus [15]. R_L and R_T can be extracted experimentally by measuring cross sections at two or more angels. This method is known as the Rosenbluth Separation and will be explained in the data analysis section in detail.

CHAPTER 2

CSR: COULOMB SUM RULE

2.1 Coulomb Sum Rule

The properties of free nucleons have been studied well through the electron scattering experiments. However, nucleons are bound in the nucleus and their properties are different than the free nucleons. This phenomena was first observed by the European Muon Collaboration (EMC) and it is known as the EMC effect [16]. Therefore, the question of how the nucleon properties are affected by the nuclear medium is important in nuclear physics. The quasi-elastic scattering off nuclei can be used to investigate the properties of bound nucleons [17].

More specifically, the quasi-elastic electron scattering can be used to study a phenomena known as the Coulomb sum rule (CSR). The CSR states that the integration of the quasi-elastic charge response function (longitudinal response function) $R_L(q,\omega)$ over the full range of energy loss ω at a constant three-momentum transfer q, should give the total number of protons (Z) in a nucleus. If we divide the integration by the number of protons, we get another form of the Coulomb sum rule which is known as S_L. $S_L(q)$ can be more explicitly defined as:

$$S_L(\vec{q}) = \frac{1}{Z}\int_{0+}^{\infty} \frac{R_L(\vec{q},\omega)}{\tilde{G}_E^2} d\omega \tag{2.1}$$

Here $\tilde{G}_E$ includes the nucleon charge form factors and a relativistic correction.

$$\tilde{G}_E = (G_E^p + (N/Z)G_E^n)\zeta \tag{2.2}$$

where $\zeta = \frac{1+Q^2/4M^2}{1+Q^2/2M^2}$ is the relativistic correction suggested by de Forest [18], G_E^p is the proton electric form factor and G_E^n is the neutron electric form factor. The lower limit of the integration doesn't include the elastic peak and excited states of the nucleus. The upper limit of the integration goes to infinity, however, experimentally one can only measure the energy range $\omega < |q|$ [19].

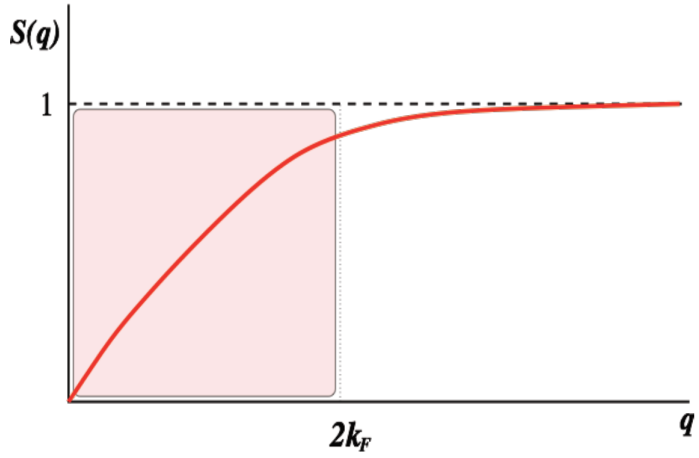

Figure 2.1: CSR shouldn't quench more than a few percent at $q = 2k_f$ and reach 1 at higher q values [17, 19].

As it can be seen in Figure 2.1, S_L is predicted to be one, when q is large ($q >> K_f$, K_f is the fermi momentum of the nucleus). However, modifications in the electromagnetic properties of the free nucleons by the nuclear medium (EMC effect) and the presence of short range correlations can change this result [17]. It is generally accepted that S_L shouldn't quench more than a few percent at $q = 2k_f$ and reach 1 at higher q values [17, 19]. The

validity of reaching unity at high q is model independent. The effects that might cause CSR not to reach unity are:

- Finite size effects: The finite size effects are due to the center of mass effects [20, 21]. This effect is seen in the actual calculation of the CSR where the center of mass effect needs to be subtracted from the nuclear charge form factor [19]. This subtraction is feasible for ligh nuclei, however, it becomes very difficult for heavy nuclei. This correction is important at low q. The effect of center of mass corrections can be seen in Figure 2.2.

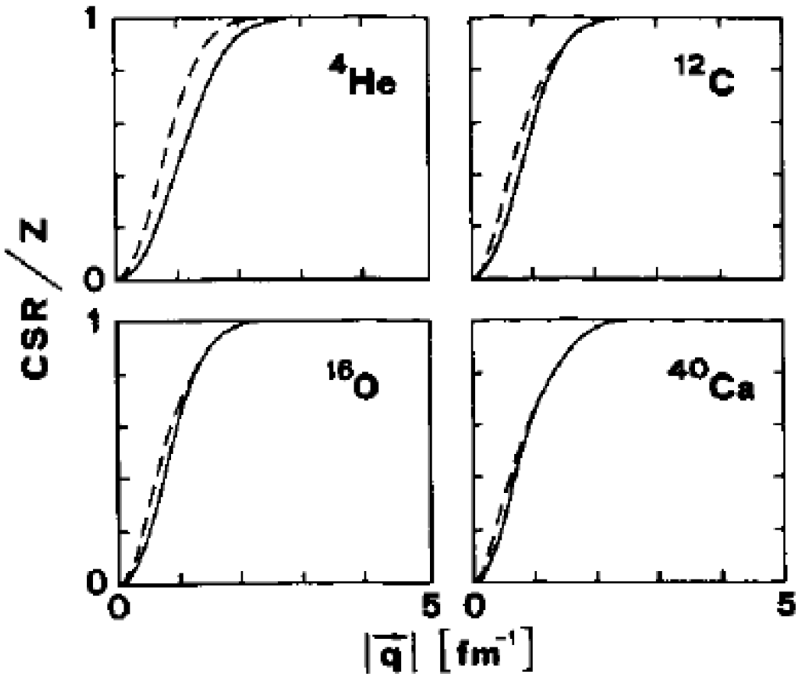

Figure 2.2: The CSR divided by the proton number, as a function of the three-momentum transfer, in the harmonic oscillator model, with (full curve) and without (dashed curve) center of mass corrections. Figure from [19]. $1fm^{-}1 = 197.24MeV$

- Pauli blocking: The nucleons are fermions and they are constrained by the Pauli exclusion principle. Therefore, two or more nucleons can not occupy the same quantum state within the same quantum system. The pauli blocking effect is more important at low q and becomes negligible at high q. This effect was calculated for ^{12}C within

the harmonic oscillator model by Lightbody [22] and shown in Figure 2.3.

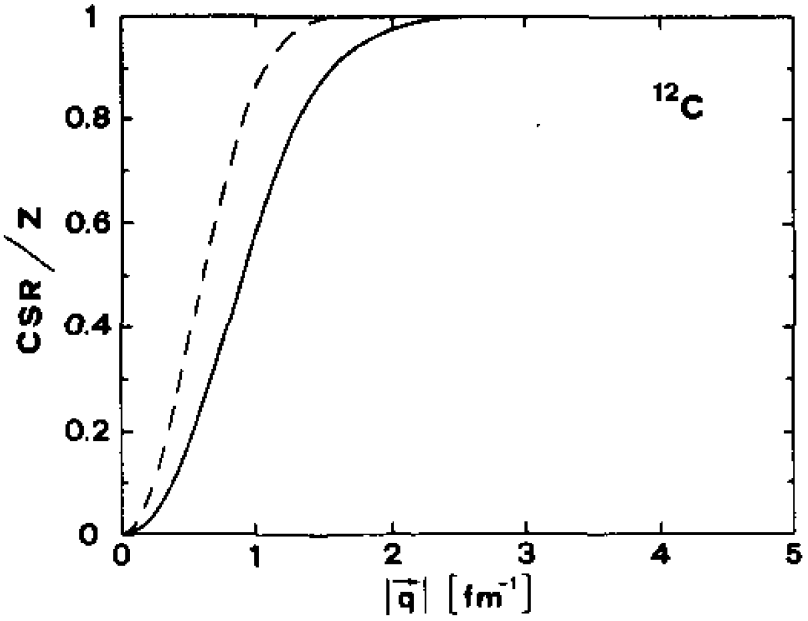

Figure 2.3: The CSR divided by the proton number, as a function of the three-momentum transfer, in the harmonic oscillator model, with (full curve) and without (dashed curve) Pauli blocking. Figure from [19]. $1fm^{-}1 = 197.24MeV$

- Long range correlations: At low q, the interactions between nucleons have a long range nature and are responsible for giant resonances [23]. The effects of long range correlations on the CSR were estimated within the random phase approximation (RPA) by Brink and Dellafiore [24] and Stringari [23]. The long range correlations are effective at low q and vanish at high q. The quenching effect on the CSR produced by the RPA is shown in Figure 2.4.

- Short range correlations: At large three-momentum transfers the virtual photon explores the medium and short inter-nucleon distances [19]. Therefore, the longitudinal response function is sensitive to the short range proton-proton correlations, and these can cause the CSR to be quenched. The short range correlations were calculated by Dellagiacoma, Orlandini and Traini [25] and the results are shown in Figure 2.5. The effect of short range correlations on CSR is very small compared to

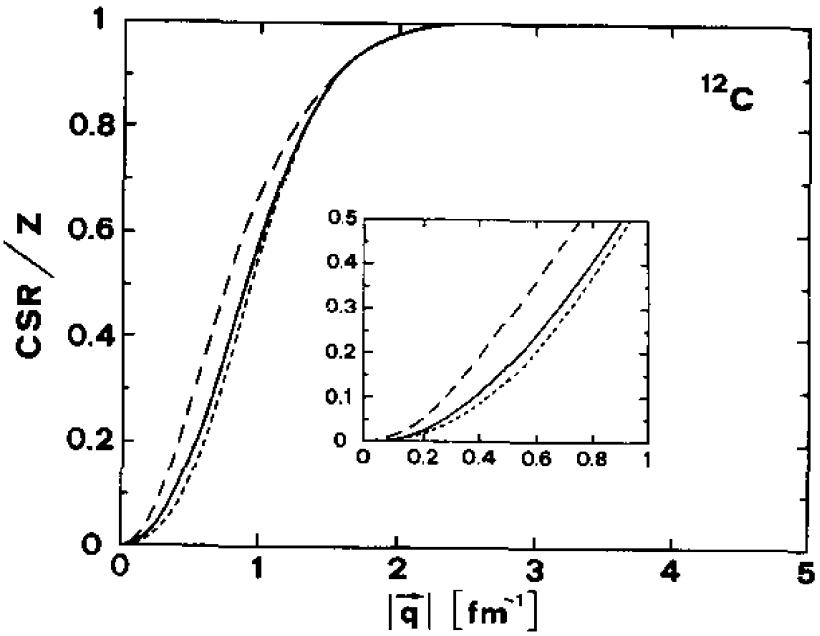

Figure 2.4: The CSR divided by the proton number, as a function of the three-momentum transfer, in the harmonic oscillator model, with (full curve) and without (long broken) center of mass correction. The short broken curve represents the result including RPA correlations. Figure from [19]. $1fm^{-}1 = 197.24MeV$

the long range effects at low q [22].

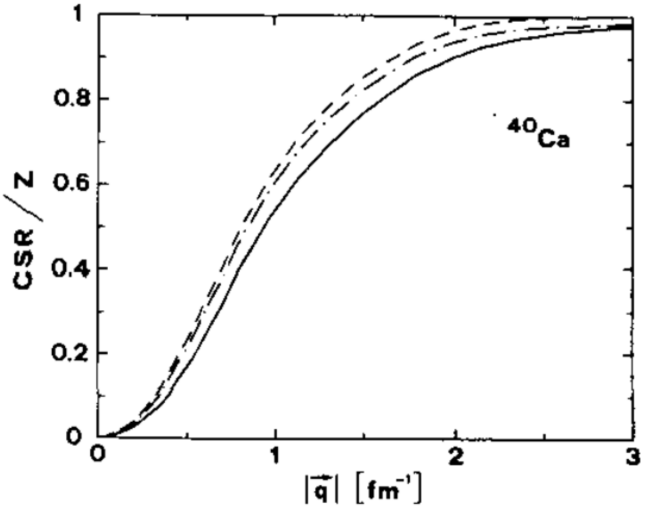

Figure 2.5: The CSR divided by the proton number, as a function of the three-momentum transfer, in the harmonic oscillator model, with (broken curve) short-range correlations included. Figure from [19]. $1fm^{-}1 = 197.24MeV$

2.1.1 World Data

According to Orlandini and Traini, [19] the Coulomb sum rule dates back to 1931 when Heisenberg studied the total cross section for the absorption of x-rays of momentum q by an atom of atomic number Z. However, Drell and Schwartz [26] and McVoy and Van Hove [27] formulated the Coulomb sum rule for electron scattering for the first time.

The first measurement of the CSR at the Massachusetts Institute of Technology Bates linear accelerator [28] found that S_L was 10% less than unity for the Fe target. In the last thirty five years a large experimental program has been carried out at the Bates [28–34] , Saclay nuclear research center in France [35–39] and SLAC national accelerator laboratory [40–42] to measure S_L for various nuclei at different three momentum transfer values. The early experiments performed at Bates [28] and Saclay [36] found S_L up to 40% different than the expected values for ^{56}Fe target in $|\mathbf{q}|$ range of 350-550 MeV/c.

The existing data for longitudinal and transverse functions is available on ^{2}H,^{3}H,^{3}He,^{4}He, ^{12}C,^{40}Ca,^{48}Ca,^{56}Fe and ^{238}U in the three momentum transfer range of 200 MeV/c to 600 MeV/c. Most of the experimental data are in the three monetum transfer region where different interactions can prevent the CSR to reach unity. There is only one point available at large three momentum transfer at $q = 1140$ MeV from SLAC NE9 [43]. However, the SLAC point has very large uncertainties.

The status of the measured Coulomb sum rule for various nuclei is summarized in Figure 2.9. As can be seen in Figure 2.9, while the CSR results for lighter nuclei (^{3}He) reach 1 at high q quickly (see Figure 2.6), there is up to 40% quenching for medium (^{56}Fe,^{40}Ca and ^{48}Ca) (see Figure 2.7) and heavy nuclei (^{208}Pb).

The experimental results have various explanations which are listed below:

- Validity of experiments: Due to the experimental limitations in the actual facilities to keep the experimental background under control, the results have been questioned. Inadequate lever arm strength is another concern that was raised for the same exper-

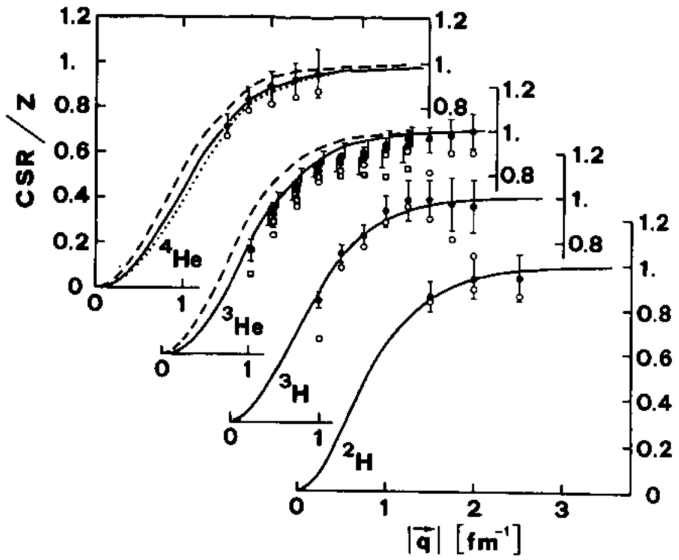

Figure 2.6: The CSR divided by the proton number as a function of three momentum transfer for medium weight nuclei Continuous curves: results from Schiavilla [44]; dotted curve: correlated model. The empty points represent the experimental values, while the filled points are the tail corrected results. Both Saclay (circles) and Bates (squares) data are shown for ^3He. Figure from [19].

iments.

- Inadequate Coulomb corrections (especially for heavy nuclei): The Rosenbluth separation is valid under the plane wave Born approximation (PWBA), however, for medium and heavy nuclei this aproximation is not valid due to the Coulomb field of nucleus, and the distorted wave Born approximation (DWBA) needs to be used. Effective momentum approximation, which will be explained later, needs to be used to correct for the Coulomb field and these corrections are known as the Coulomb corrections. Inadequacy of the Coulomb corrections for the analysis of existing experiments could be a possible reason of quenching for medium and heavy nuclei.

- Swollen nucleon: The question of whether the properties of the free nucleons are the same as the nucleons in the nuclei has been a longstanding question in nuclear physics [19]. Noble [45] is the first person who suggested that the mechanism which changes the mass should also change the nucleon charge radius. His calculations

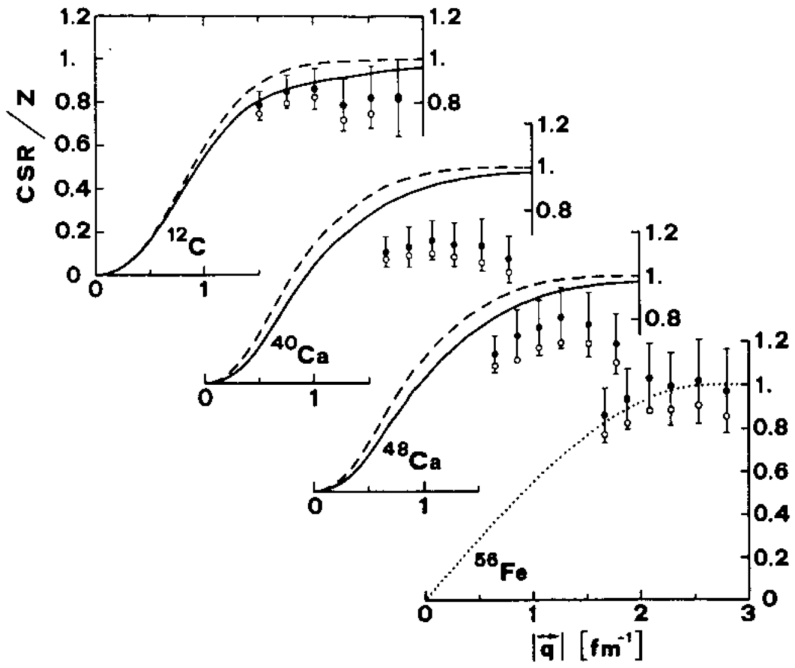

Figure 2.7: The CSR divided by the proton number as a function of three momentum transfer for medium weight nuclei. Broken curves: harmonic oscillator; Continuous curves: correlated model; Dotted curve: Fermi gas model, $k_f = 1.32 fm^{-}1$. The empty points represent the experimental values from Saclay, while the filled points are the tail corrected results. Figure from [19].

showed a 30% increase in the nucleon charge radius. He calculated the CSR by using the Fermi gas model (FGM) with an increased charge radius. The results are shown in Figure 2.8.

A later analysis on Saclay and Slac data by Jourdan [47] suggested that no quenching exists by using the distorted wave Born aproximation with the Coulomb corrections. However, reanalysis of Saclay Data by Morgenstern and Meziani [17] with the effective momentum approximation showed that quenching still exists. The comparison between M&M's analysis and Jourdan's work is presented in Table 2.1.

2.1.2 Theoretical Calculations

The quenching of R_L is also known as the missing charge problem and there have been great theoretical efforts to understand and solve this problem. The non-relativistic models

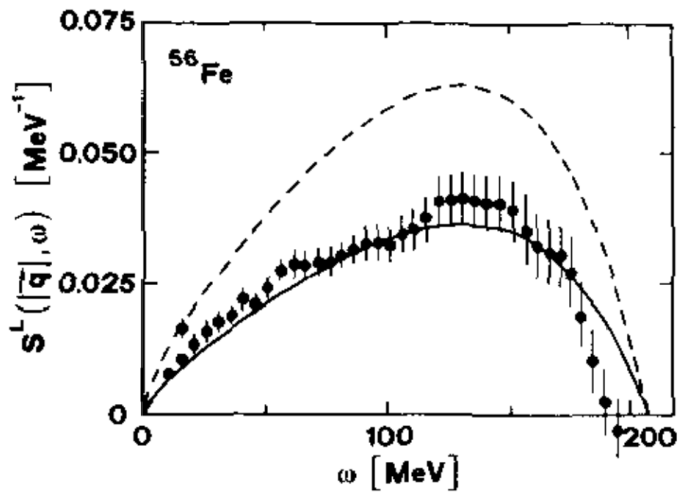

Figure 2.8: Longitudinal structure function in the relativistic FGM calculation of Noble [45] for $|q| = 410 MeV/c (k_f = 1.11 fm^{-}1)$. Experimental data from Altemus [28]. Broken curve: impulse aproximation; Full curve: results with scaled root mean square radius. Figure from [19].

Analysis	Saclay Uncertainty	SLAC Uncertainty	Coulomb Correction	S_L
Jourdan	total	statistical	No	0.86 ± 0.12
	total	statistical	Yes	0.91 ± 0.12
M&M	total	(*)	No	0.72 ± 0.23
	total	(*)	Yes	0.63 ± 0.20
	total	total	No	0.82 ± 0.12
	total	total	Yes	0.73 ± 0.12

Table 2.1: Comparison of the Coulomb Sum in ^{56}Fe between Jourdan and M&M analysis at $\vec{q}$ = 570 MeV/c.(*) NO SLAC data were used. Table from [17]

couldn't explain why quenching exists [4]. There have been other models which counted for relativistic corrections, final state interactions, and two body and many body interactions [48–51]. These effects were found to be important, but not large enough to explain all quenching.

As stated earlier, the swollen nucleon idea was first proposed by Noble [45] and then by others [52–54] to solve the quenching problem and to explain the EMC effect. However, the y-scaling analysis of Sick at high q found the limits for the change in nucleon size to be $< 3-6\%$ [55].

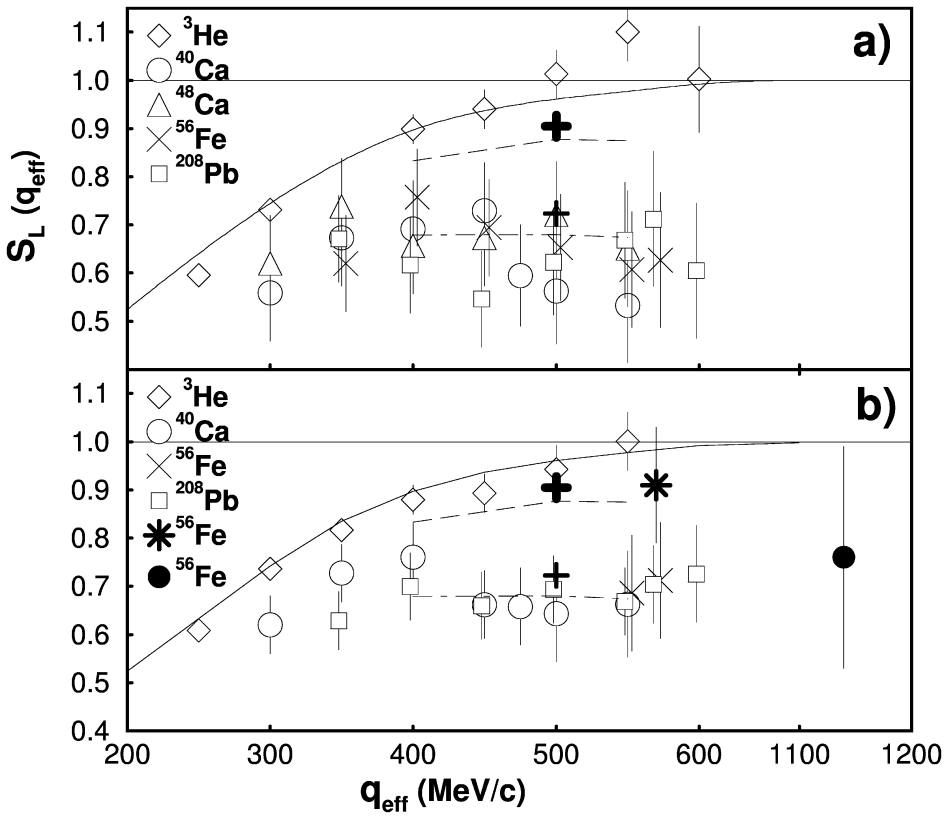

Figure 2.9: S_L obtained in the EMA as a function of q_{eff} using only Saclay data (a) and using Saclay data combined with SLAC NE3 and Bates data with the new experimental setup (b). NM calculations (solid line) [46], NM calculations integrated within the experimental limits: dashed line, same with modified form factors (dotted-dashed line), ^{208}Pb HF calculations integrated within the experimental limits (thick right cross), same with modified form factors (thin right cross). ^{56}Fe SLAC NE9 (filled circle) and Jourdan analysis of 56Fe Saclay data (thick star) are shown in (b). Figure from [17]

The relativistic models which were based on hadron and meson degrees of freedom were used to calculate R_L (see Figure 2.10) . Although, the agreement between the calculations and the experiments improved, the agreement is not good enough to explain the total quenching of R_L [15, 56, 57].

A very recent calculation of the CSR by Cloet *et.al* [58] using the relativistic and medium nuclear effects, indicated that medium modifications can cause up to 30% quenching at $|q| = 1GeV$ for ^{12}C.

Each of these models predict R_L differently for high momentum transfers. If the final state interactions and nucleon-nucleon correlations cause the quenching, then at high three

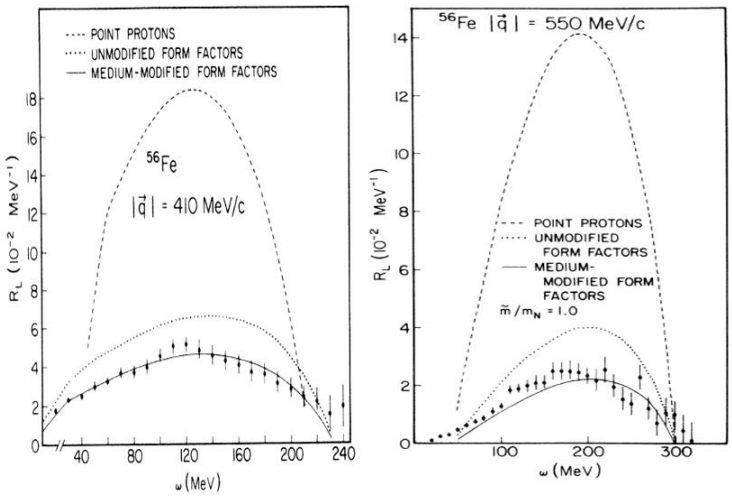

Figure 2.10: Longitudinal response functions for ^{56}Fe at $q = 410MeV/c$ (left) and $q = 550MeV/c$ (right) calculated using a relativistic Fermi gas model. The dashed curves are the result for pointlike protons. The dotted curves are the results obtained with free form factors. The solid curves are the results of calculations using the medium-modified form factors. Figure from [4]

momentum transfers quenching should decrease, since these interactions fall quickly when q increases [4]. However, if quark effects, swollen nucleon effects, or the vacuum polarization effects are repsonsible for the quenching, then the quenching will increase at high q, since these effects gets larger as q gets larger. Therefore, more data are needed at the high q region.

2.1.3 The E05-110 Experiment

Nearly 40 years after the CSR was first formulated, the question of why the experimental results are quenched for medium and heavy nuclei has still not been solved, and an overall agreement between the different study groups has not been reached. Therefore, Coulomb sum rule is still an unsolved puzzle. To solve this puzzle the E05-110 experiment at Thomas Jefferson Labaratory measured data for ^4He,^{12}C,^{56}Fe and ^{208}Pb targets from $|q| = 550MeV/c$ to $|q| = 1000MeV/c$ [59]. The E05-110 experimental data were measured at four different angles $15^\circ, 60^\circ, 90^\circ$ and 120° with the largest lever arm in a single experiment ($15^\circ - 120^\circ$). The E05-110 results from light nuclei to medium and heavy

nuclei will shed light on the medium dependancy of the CSR. Since the $|q|$ range for the E05-110 experiment is the region where the CSR is model independently expected to reach unity, the results will indicate whether the nucleon properties are affected by the nuclear medium or not.

In this thesis, the details of the experimental setup and data acquisiton are explained in Chapter 3. Chapter 4 contains the data analysis of the E05-110 experiment that was performed at Temple University. The results are given in Chapter 5 and Chapter 6 contains conlusions.

CHAPTER 3

THE E05-110 EXPERIMENT

E05-110 is an inclusive quasi-elastic electron scattering experiment which ran from October 23rd 2007 to January 16th 2008 in experimental Hall A at the Thomas Jefferson National Accelerator Facility (Jefferson Lab) in NewPort News, VA. Jefferson Lab is a lineer accelerator (LINAC) that accelerates electrons. Hall A has two almost identical high resolution spectrometers with a series of magnets and detectors that help to identify particles, and measure their properties after the scattering process. In the experiment E05-110, the accelerated electrons scattered off the targets: H_2,^4He,^{12}C,^{56}Fe and ^{208}Pb. The targets were set up on a target ladder which was controlled remotely. In the experiment, data was taken at various beam energies and momentum settings. This chapter discusses the experiment E05-110 in detail.

3.1 The Continuous Electron Beam Accelerator Facility at Jefferson Lab

The Continuous Electron Beam Accelerator Facility (CEBAF) at Jefferson Lab (see Figure 3.1) is one of the most advanced facilities for investigating the structure of nuclei and hadrons, and the underlying fundamental interactions in the region below the high-energy

”asymptotically free” regime. CEBAF’s 6 GeV continuous wave electron beam has been recently upgraded to 12 GeV and it is an ideal probe for studying the nuclear structure because the electromagnetic interaction is well understood, and the wavelength of the electron at this energy is a small percent of the nucleon’s size [60]. This experiment was run before the 12 GeV upgrade, therefore the properties of CEBAF with 6 GeV will be discussed.

3.1.1 Accelerator

The CEBAF accelerator is a five-pass recirculating superconducting radio-frequency (SRF) linear accelerator (linac) and is capable of delivering a beam to all the experimental halls simultaneously. The accelerator has 5 main parts: injector, two superconducting linacs, RF separators and two arcs. The main parts of the accelerator are shown in the Figure 3.3.

The injector consists of an electron source and 18 SRF cavities. The electron source provides electrons with energy about 100 keV and each cavity accelerates electrons by 2.5 MeV. The electrons reach an energy of $45MeV$ before being inserted in linac.

There are 160 cavities in each linac based on a design developed in Cornell University [61]. These cavities were built at the Thomas Jefferson Lab from niobium (see Figure 3.2) . Niobium is a superconducting material at 2 K. Liquid He is used to cool cavities at superconducting temperatures. The cavities are utilized in a linac configuration by cryomodule configurations. There is a total of 20 cryomodules which contain 160 cavities. The central helium refrigerator, located in the center of the racetrack, supplies liquid He at 2 K and 2.8 atm.

The linacs are linked to each other by two recirculation arcs which consist of hundreds of magnets. The electron beam is bent and focused by these magnets.

CEBAF was originally designed to accelerate electrons up to $4GeV$ by recirculation of the beam through non-superconducting linacs. The electrons gain $400MeV$ for each circulation. After changing the design to use two superconducting radio-frequency linacs, the electrons can be accelerated up to $6GeV$. The electrons can be injected to the accelerator

Figure 3.1: Top view of the Thomas Jefferson National Accelerator Facility

in two different ways: either from a thermionic or a polarized gun. In the polarized gun a strained GaAs (Galyum arsenide) cathode is illuminated at a 780nm wavelength by a 1497MHz diode laser [60]. The laser light excites the valance electrons in the GaAs and moves them to the conduction band. The electrons are then extracted to the injector by

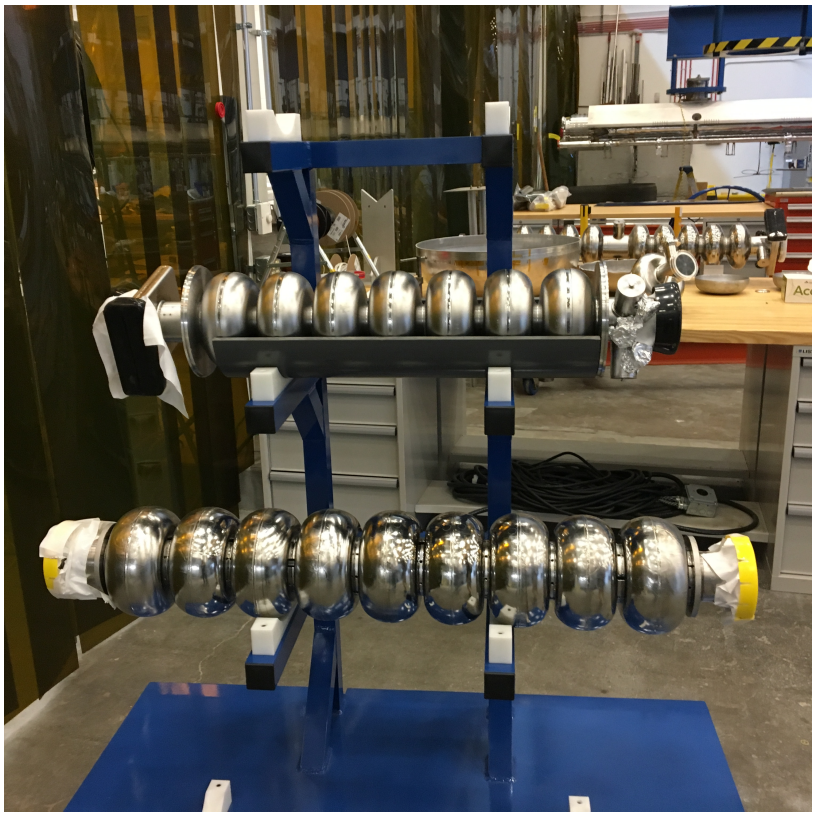

Figure 3.2: CEBAF superconducting radio-frequency cavities

applying $-100KV$ voltage [62].

The beam can be delivered to all the experimental halls at the same time and the current in each hall can be controlled independently. Radio frequency separators (RF deflecting cavities), which are operating at 499 MHz, are used to deliver three beams at different energies. These RF separators are located in the beam switch yard before the beamlines going to the experimental halls. The beam current can reach up to $200\mu A$ with 90% polarization [61]. The E05-110 experiment ran at initial electron energies from 400 MeV to 4000 MeV with current range from 1 μA to 60 μA.

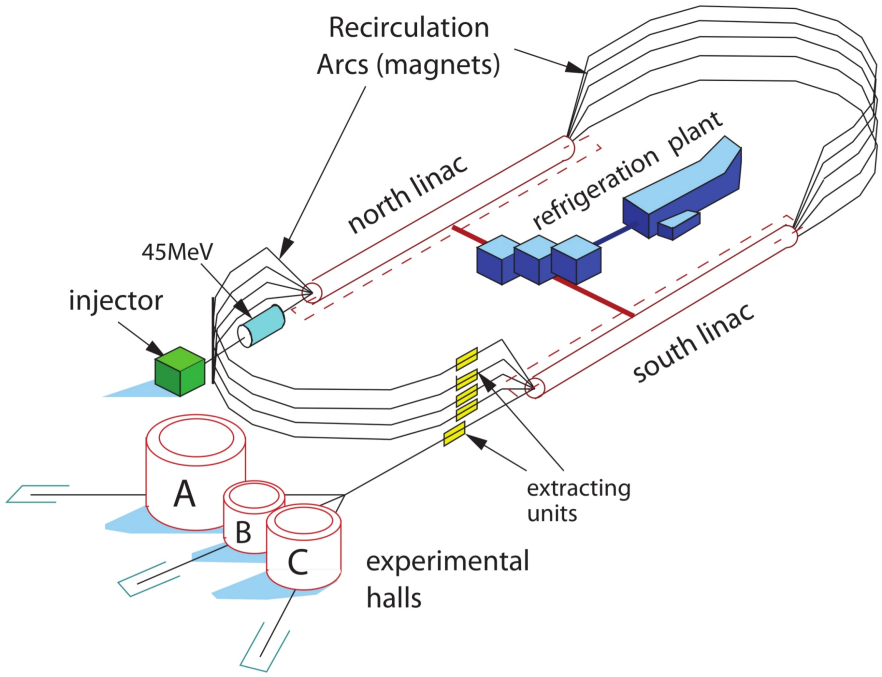

Figure 3.3: CEBAF recirculation arcs for ramping up the electron beam energy. [62].

3.2 Hall A Beamline

Figure 3.4 shows the layout of the beamline and the spectrometer components in Hall A. The instrumentations to determine the properties of the beam, such as beam energy, current, polarization, position and direction are also shown in the Figure 3.4.

The Hall A beamline is separated into several sections and maintained at vacuum pressure $\leqq 10^{-6}$ Torr. The beam measurement elements consist of the transmission-line position monitors, current monitors, superharps, beam loss monitors and optical transition radiation viewers (OTR). The beam optics elements consist of the focusing and corrector magnets. A fast rastering system, which operates between 17 and 24 KHz, is located 23 m upstream of the target position and rasters the beam over several mm's in both directions at the target [60].

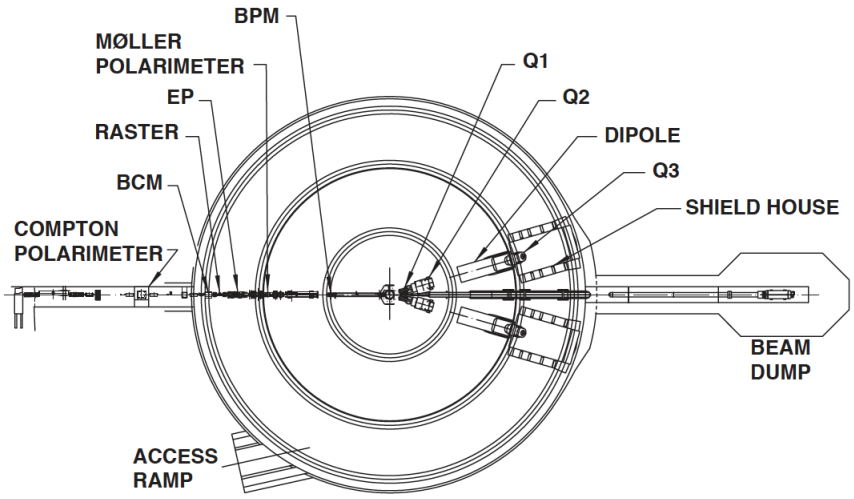

Figure 3.4: Schemetic layout of Hall A [60].

3.2.1 Beam Energy Measurements

The beam energy is measured by two different methods: The Arc Method and the eP Method.

- The Arc Method: The energy is determined by the measurement of the beam deflection in the arc section of the beamline. The beam is bent by $\theta = 34.3^\circ$ in the arc section of the beamline. The momentum of the beam can be determined from the field integral of dipol magnets and the bend angle by

$$p = k\frac{\int \vec{B} \times d\vec{l}}{\theta} \tag{3.1}$$

where $k = 0.299792$ GeV$\cdot$ rad $T^{-1}m^{-1}/c$. The p is in units of GeV/c. The magnetic field integral and the actual bend angle of the arc need to be measured simultaneously in order to determine the beam energy from the arc method. The scanners, an absolute angle measurement device, and an absolute field integral measurement device are used for the angle and field integral measurements. The systematic uncertanities are given in the table 3.1.

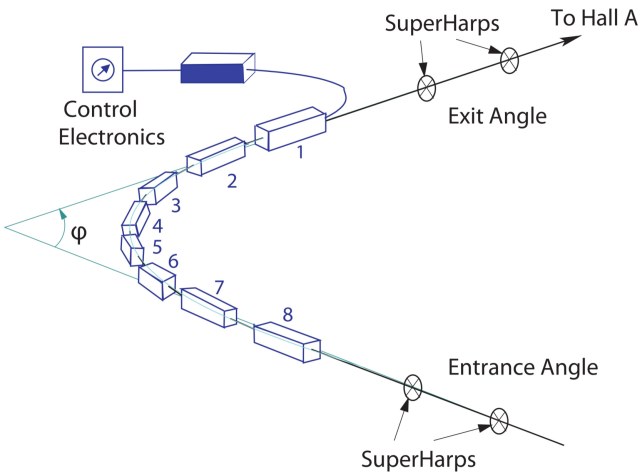

Figure 3.5: The measurement of beam energy by Arc method. Figure [62]

Table 3.1: The systematic uncertanities on the bend angle, the field integral, and the energy measurement from the arc method [60].

	E= 0.5 GeV	E = 4.0 GeV
Bend angle	$2.2x10^{-5}$	$2.2x10^{-5}$
Field integral	$1.2x10^{-4}$	$6.4x10^{-5}$
Energy	$1.2x10^{-4}$	$6.8x10^{-5}$

- The eP Method : A stand-alone device located 17 m upstream of the target along the beamline is used for the beam energy measurement in this method. The measurement of the scattered electron angle θ_e and the recoil proton angle θ_p in the H(e,e'p) elastic reaction are used to calculate the beam energy, E. This is done according to the given formula:

$$E = M_p \frac{cos(\theta_e) + sin(\theta_e)/tan(\theta_p) - 1}{1 - cos(\theta_p)} + 0(m_e^2/E^2 \tag{3.2}$$

where M_p is the mass of the proton and m_e is the mass of the electron. An electron and proton detector system, which is made up of a set of 2x8 silicon micro-strip detectors, is used in both spectrometer arms to measure beam energy simultaneously [60].

3.2.2 Measurement of Beam Current and Charge

Beam current monitors (BCM) are used to measure the beam current. The beam current measurement and the run time are used to calculate the total charge accumulated on the target. The total accumulated charge for each run is directly used in the cross section calculation to find the incident number of the electrons. Hall A BCM consists of an Unser monitor, two RF cavities, associated electronics and a data-acquisition system. There are two BCMs in Hall A and they provide stable low-noise, non-interfering beam current measurements. A cavity monitor and a Faraday Cup at the injector section of the accelerator are used in addition to the Unser monitor to provide a reference during the calibration runs. The Unser monitor is also used as a reference and calibrated by a known current through the wire inside the beam pipe. Magnetic shielding is required for noise reduction. Two stainless steal RF cavity monitors are tuned to beam frequency (1497MHz). One of the cavities is located downstream and the other one is upstream and their output voltage is proportional to the beam current. Each RF output signal is split into two parts: integrated and sampled. The Hall A beam current measurement system is shown in Figure 3.6.

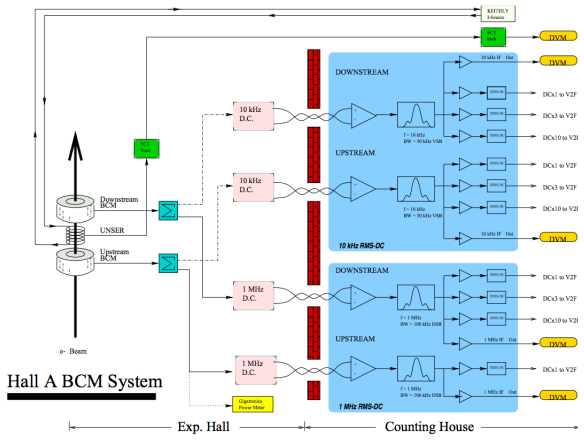

Figure 3.6: Schematic of the Hall A beam current measurement system. Figure [63]

For the sampled data, the output from one of the amplifiers is sent to an AC voltmeter that generates a signal proportional to the RMS of the input signal every second. The

output is also proportional to the beam charge accumulated during the corresponding second. Signals from both cavities' multimeters and the multimeter connected to the unser are transported to a computer and recorded every 1-2 s [60].

The other amplifier output is sent to the RMS-to-DC converter which produces an analog DC voltage level for the integrated data. A Voltage-To-Frequency converter then uses these levels to output a frequency that is proportional to the input DC voltage level. The output signals are fed to 200 MHz VME scalers and then injected to the data stream with other scaler information. A set of amplifiers with different gain factors (x1,x3,x10) are used to extend the non-linear region to lower currents. Thus, each RF cavity has three signals: U1, U3, U10 and D1, D3, D10. U corresponds to upstream and D corrresponds to downstream. These signals are fed to the scaler input of each spectrometer and used to calculate charge for each run. The calibration of the scalers and the calculation of the charge is explained in section 4.1.1.2.

The average current during the E05-110 experiment changes between $1\mu A$ and $50\mu A$. Thus, the gain x3 is used for charge calculation.

3.2.3 Measurement of Beam Position and Direction

The beam position at the target is an important measurement for the reconstruction of the scatttering vertex. The optics calibration and acceptance calculation are also dependent on the location of the beam at the target. Two Beam Position Monitors (BPMs) are used to determine the position and the direction of the beam at the target. These BPMs are located 7.524 m and 1.286 m upstream of the target. The percent difference between two BPMs is used to determine the relative position of the beam to within $100\mu m$ for currents above $1\mu A$. The calibration of the BPMs with respect to the wire scanners (superharps) is used to determine absolute position of the beam. The wire scanners are located next to BPMs and surveyed at regular intervals. Position information from BPMs has to be calibrated independently and is saved in two ways [60]:

- The beam position is averaged over 0.3 s and written to the EPICS every second and then injected into the data stream every 3-4 s.

- The beam position from BPMs is recorded in the CODA data stream from each of the 8 BPM antennas.

The Hall A beam position monitor system is shown in Figure 3.7.

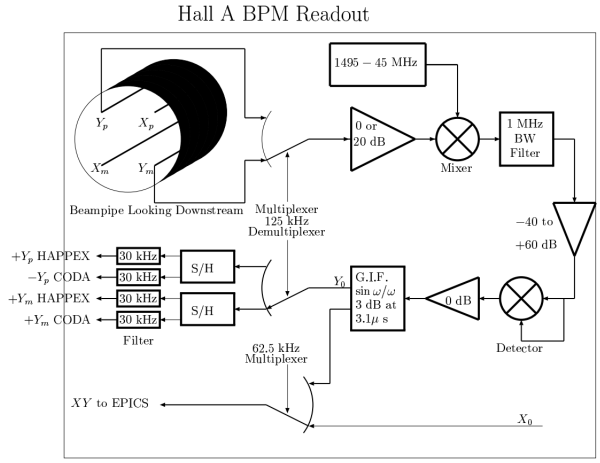

Figure 3.7: Schematic of the Hall A beam position monitor system. Figure [63]

3.2.4 Beam Raster

The beam spot is small and can damage the target cell at high currents. In order to avoid damage due to heat transfer, the beam is scanned to a size of a few mms and this is called beam rastering. Rastering the beam decreases the density fluctuations. The dependence of the density fluctuations on the beam current and raster can be found in the paper [64].

The beam raster system in Hall A is a fast rastering system (17–24 kHz) and located 23 m upstream of the target position. This raster system allows the beam to be rastered over several mms in both directions at the target [60].

3.3 Coordinate Systems

There are five coordinate systems in experimental Hall A and all the coordinate systems presented are Cartesian.

These coordinate systems are:

- Hall Coordinate System (HCS)
- Target Coordinate System (TCS)
- Detector Coordinate System (DCS)
- Transport Coordinate System (TRCS)
- The Focal Plane Coordinate System (FPCS)

The center of the hall is the origin of the HCS and it is defined by the intersection of the direction of the electron beam and the vertical symmetry axis of the target system. The z-axis is along the beam line and points to the beam dump. The y-axis points up vertically. See Figure 3.8.

There are two spectrometers in Hall A and each has its own TCS. A line perpendicular to the sieve slit surface of the spectrometer and going through the midpoint of the central sieve slit hole defines the z-axis of the TCS for a given spectrometer [65]. The y-axis goes through the origin of the HCS and points to the left side of the z axis. The x-axis points downward. The z_{tg} points away from the target. Ideally, the spectrometer would point directly at the hall center, however, during the experiment the spectrometer does not perfectly point at the hall center. It usually has a mispointing D_x and D_y which is measured by the survey group. The survey group also measures the distance from the midpoint of sieve slit surface to the hall center. The x_{tg} axis is parallel to the sieve slit surface with x_{tg} pointing down vertically. The out-of-plane angle (θ_{tg}) and the in-plane angle (ϕ_{tg}) are given by $\frac{dx_{tg}}{Z_0}$ and $\frac{dy_{tg}}{Z_0}$ respectively. See Figure 3.9

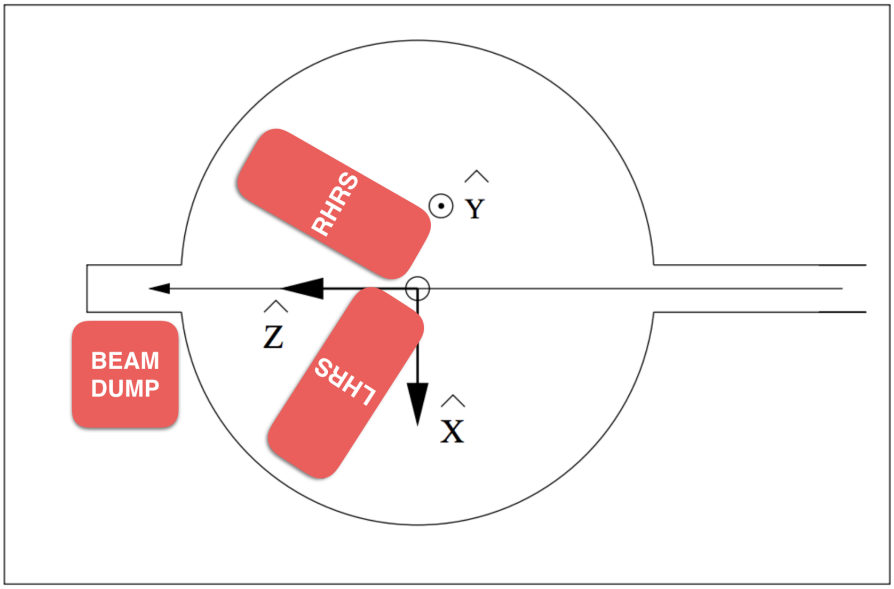

Figure 3.8: Top View of the Hall Coordinate System. Figure reproduced from [65].

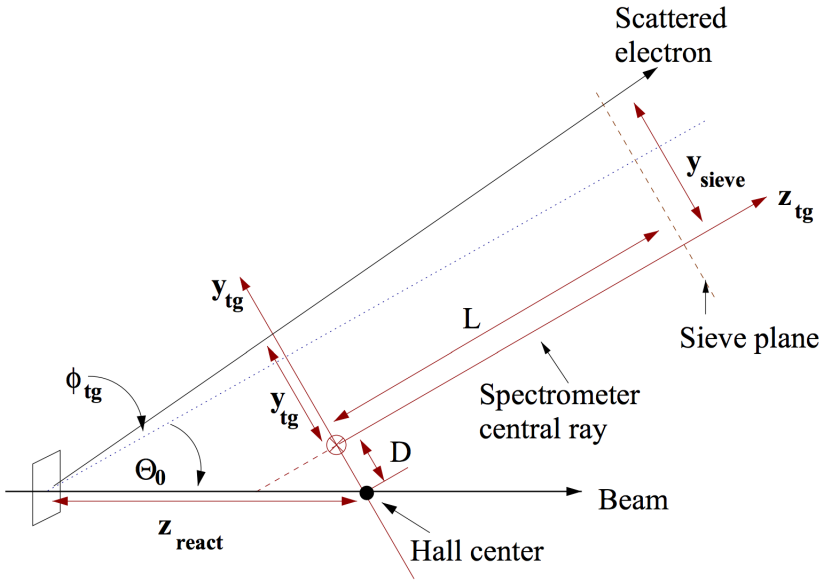

Figure 3.9: Top view of the TCS for electron scattering from a thin foil target. L is the distance from the hall center to the sieve plane, while D is mispointing. The spectrometer central angle is denoted by θ_0. Note that x_{tg} and x_{sieve} point vertically down (into the page) [65].

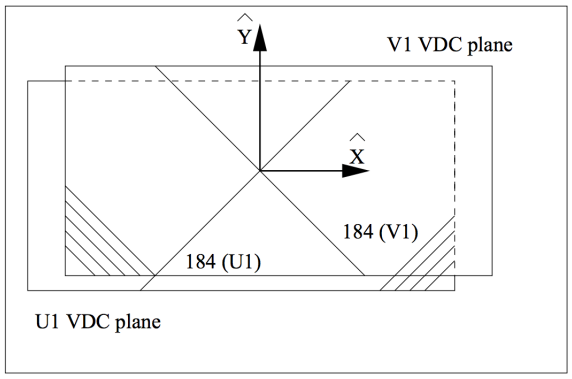

Figure 3.10: Top View of Detector Coordinate system [65].

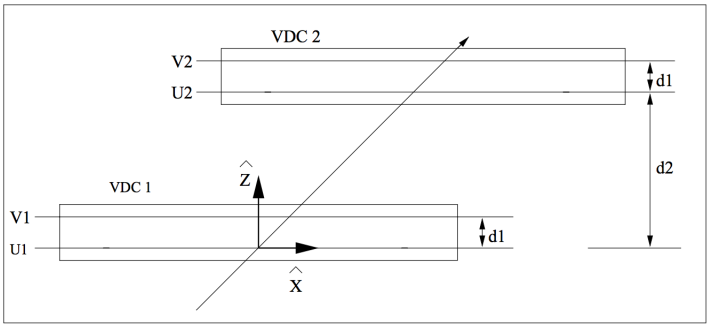

Figure 3.11: Side View of Hall Coordinate system [65].

The Vertical Drift Chamber (VDC) is used to define DCS. The origin of DCS is at the intersection of wire 184 of the VDC U1 plane and the perpendicular projection of wire 184 in the VDC V1 plane onto the VDC U1 plane (Each plane has 368 wires). y-axis is parallel to the short axis of the lower VDC. z-axis is perpendicular to the VDC U1 plane and points vertically up, while x-axis is along the long axis of the lower VDC and points away from the center of curvature of the dipole. See Figure 3.10 and Figure 3.11. The analysis variables that are defined in DCS are labeled with $_{det}$ subscript. These variables are calculated with some assumptions. Any deviation from these assumptions will require offsets in DCS. These offsets are used to correct the focal plane vertex calculation [65].

The TRCS at the focal plane is generated by rotating the DCS clockwise around its y-axis by 45° (see Figure 3.12). Ideally, the z-axis of the TRCS coincides with the central ray of the spectrometer. However, due to the mispointings mentioned above, the TRCS can

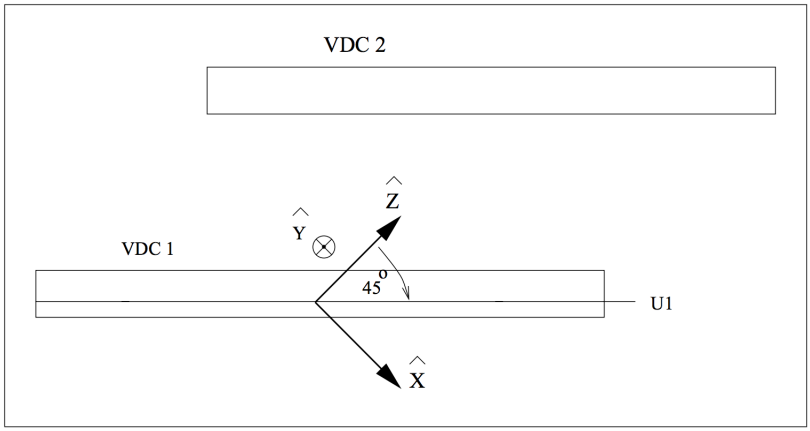

Figure 3.12: Side View of Transport Coordinate system [65].

differ from the ideal spectrometer Transport Coordinate System. The transport coordinates can be defined in terms of the detector coordinates by

$$\begin{aligned} \rho_0 &= -45^\circ \\ \theta_{tra} &= \frac{\theta_{det} + \tan\rho_0}{1 - \theta_{det}\tan\rho_0} \\ \phi_{tra} &= \frac{\phi_{det}}{\cos\rho_0 - \theta_{det}\sin\rho_0} \\ x_{tra} &= x_{det}\cos\rho_0(1 + \theta_{tra}\tan\rho_0) \\ y_{tra} &= y_{det} + \sin\rho_0\phi_{tra}x_{det} \end{aligned} \tag{3.3}$$

The focal plane coordinate system (FPCS) is a rotated coordinate system and it is obtained by rotating the DCS around its y-axis by an angle, where ρ is the angle between the local central ray and the z-axis of the DCS. The local central ray is the ray with $\theta = \phi = 0$ for the corresponding relative momentum $\frac{\Delta P}{P}$. Thus, the z axis of the FPCS rotates as a function of the relative momentum $\frac{\Delta P}{P}$. In FPCS the dispersive angle is small for all points across the focal plane. The transformation to the FCS also includes corrections for the offsets incurred due to misalignments in the VDC package. The coordinates of FCS can be shown as follows:

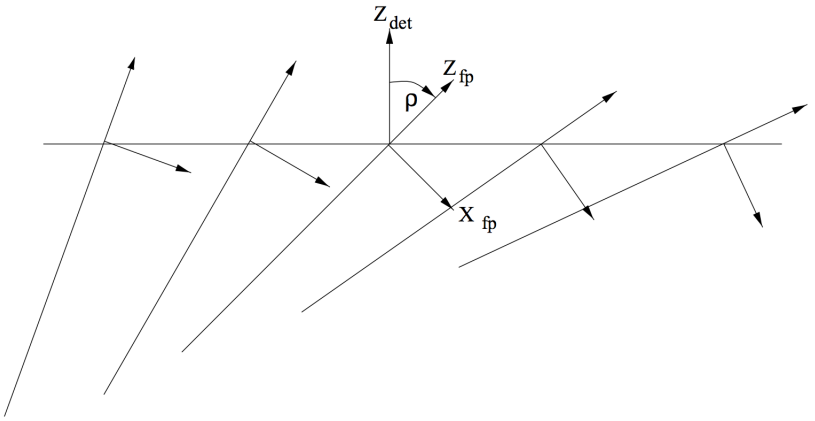

Figure 3.13: The focal plane (rotated) coordinate system as a function of the focal plane position [65].

$$
\begin{aligned}
x_{fp} &= x_{tra} \\
\tan\rho &= \sum_{i=0}^{6} t_{i000} x_{fp}^{i} \\
y_{fp} &= y_{tra} - \sum y_{i000} x_{fp}^{i} \\
\theta_{fp} &= \frac{x_{det} + \tan\rho}{1 - \theta_{det}\tan\rho} \\
\phi_{fp} &= \frac{\phi_{det} - \sum p_{i000} x_{fp}^{i}}{\cos\rho - \theta_{det}\sin\rho},
\end{aligned}
\tag{3.4}
$$

3.3.1 Experimental Target Variables

Target variables can be calculated with the help of the coordinate systems defined above. For each event, there are two angular coordinates (θ_{det} and ϕ_{det}) and two spatial coordinates (x_{det} and y_{det}) measured at the focal plane. x_{det} is the position of the particle and θ_{det} is the tangent of the angle made by its trajectory along the dispersive direction, while y_{det} is the position and ϕ_{det} is the tangent of the angle perpendicular to the dispersive direction. These focal plane variables are corrected for any detector offsets from the ideal central ray of the spectrometer to obtain the focal plane coordinates $x_{fp}, \theta_{fp}, y_{fp}$ and ϕ_{fp}. A detailed

description of the Hall A optics coordinate systems is given in [65]. The focal plane variables are used to calculate the target variables $\theta_{tg}, y_{tg}, \phi_{tg}$ and δ for the particle at the target. The calculation is done by matrix inversion which links the focal-plane coordinates to the target coordinates (in a first order approximation) [60].

$Y_{jkl}, T_{jkl}, P_{jkl}$ and D_{jkl} tensors connect the focal-plane coordinates to the target coordinates according to

$$D_{jkl} = \sum_{i=0}^{m} C^{D}_{ijkl} x^{i}_{fp}$$

$$\begin{aligned}
\delta_p &= \sum_{j,k,l} D_{jkl} \theta^{j}_{fp} y^{k}_{fp} \phi^{l}_{fp} \\
\theta_{tg} &= \sum_{j,k,l} T_{jkl} \theta^{j}_{fp} y^{k}_{fp} \phi^{l}_{fp} \\
y_{tg} &= \sum_{j,k,l} Y_{jkl} \theta^{j}_{fp} y^{k}_{fp} \phi^{l}_{fp} \\
\phi_{tg} &= \sum_{j,k,l} P_{jkl} \theta^{j}_{fp} y^{k}_{fp} \phi^{l}_{fp},
\end{aligned} \tag{3.5}$$

where $Y_{jkl}, T_{jkl}, P_{jkl}$ and D_{jkl} are polynomials in x_{fp}.

3.3.2 Calculation of the Scattering Angle

The electron scattering angle, θ_{scat}, is calculated from target variables θ_{tg} and ϕ_{tg} and the spectrometer central angle θ_0. The spectrometer central angle θ_0 is the angle between the beamline and the spectrometer nominal central ray. Thus, θ_{scat} can be shown as:

$$\theta_{scat} = arccos\left(\frac{cos(\theta_0) - \phi_{tg} sin(\theta_0)}{\sqrt{(1 + \theta^2_{tg} + \phi^2_{tg})}}\right) \tag{3.6}$$

Since θ_{scat} depends on θ_{tg} and ϕ_{tg}, their accuracy will determine the accuracy of the scattering angle. This makes the determination of θ_{tg} and ϕ_{tg} variables crucial. θ_{tg} and ϕ_{tg} variables are calibrated by using electron scattering from a thin ^{12}C target.

3.3.3 Calculation of the Absolute Momentum

For each event a relative momentum δ is measured by the spectrometer. The relative momentum is then used to calculate the absolute momentum P for the same event:

$$P = P_0(1+\delta) \tag{3.7}$$

P_0 is the spectrometer central momentum and calculated from the dipole magnetic field B_0 by:

$$P_0 = \sum_{i=1}^{3} \Gamma_i B_0^i \tag{3.8}$$

where Γ_i are the spectrometer constants. The spectrometer constants are given in the table below.

Table 3.2: The spectrometer constant coefficients for the L-RHRS [60]

	$\Gamma_1(MeV/T)$	$\Gamma_2(MeV/T)$	$\Gamma_3(MeV/T)$
HRS-L	2702 ± 1	0	-1.6 ± 0.4
HRS-R	2698 ± 1	0	-1.6 ± 0.4

3.4 Target System

3.4.1 Overview

Several types of different target systems have been used in Hall A, including:

- a system of cryo-targets and solid targets
- a waterfall target
- a target of polarized gaseous ^3He

The set of cryogenic targets currently operates with liquid hydrogen, liquid deuterium and gaseous helium 3 or helium 4 as target materials. A variety of solid targets are also provided; BeO, Carbon and Aluminum are typical, but other materials are available if the need arises. The combination of cryogenic targets and a few solid targets is the standard configuration [63].

The targets that were used in experiment E05-110 are discussed in this chapter.

3.4.2 Target Chamber

In Hall A, targets are contained in a special target chamber, which is a large evacuated multistaged cylinder. The target chamber is used to isolate the cryogenic target and beam line vacuum from the environment. This way each HRS can rotate around the target without vacuum coupling and without limiting kinematic and acceptance specifications for each HRS. It was also designed to contain more than one target at the same time and control them remotely. Thin aluminum foils are used to isolate the target chamber from the environment while minimize the material for the scattered electron passing through to the HRS. These aluminum windows are made of 5052 H34 aluminum foil and it is 6 *in* high and 0.016 *in* thick [63].

The target chamber has continous angle coverage from $\theta_{min} = 12.54^{\circ}$ to $\theta_{max} = 165^{\circ}$ [63]. The chamber is built from several rings with a 1.037 m diameter and supported by central pivot post that has a 0.607 m diameter. The beam enters through an oval hole in the middle ring which has a 5.23 cm width and exits through a 4.6 cm hole connected to the exit pipe. The cryogenic targets sit in the upper ring [66].

3.4.3 Target System For E05-110 Experiment

The experiment E05-110 used targets ranging from light nuclei to heavy nuclei in order to study medium dependency of the Coulomb Sum rule .H_2,^4He,^{12}C,$^{23}Al, Empty, BeO$,^{56}Fe and ^{208}Pb are the targets used in this experiment. These targets were installed on a target

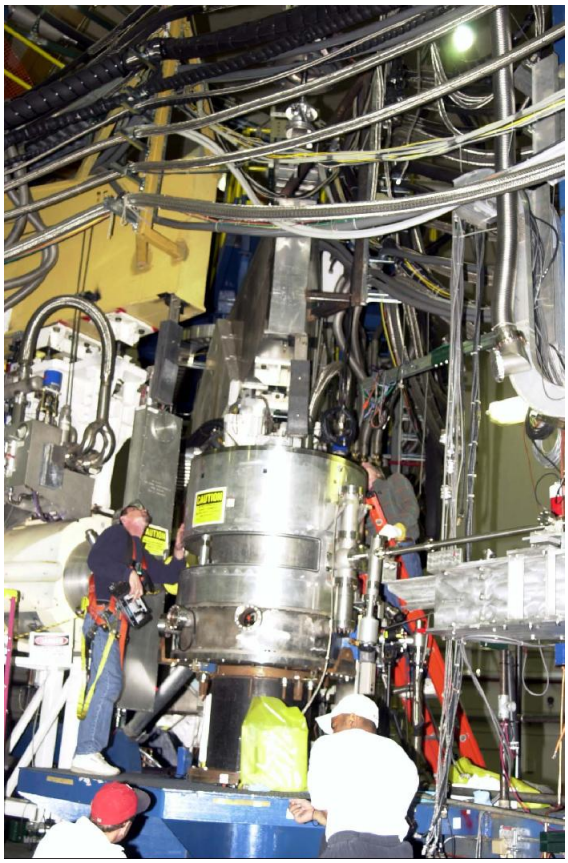

Figure 3.14: Hall A target chamber.

ladder in the target chamber to control them remotely.

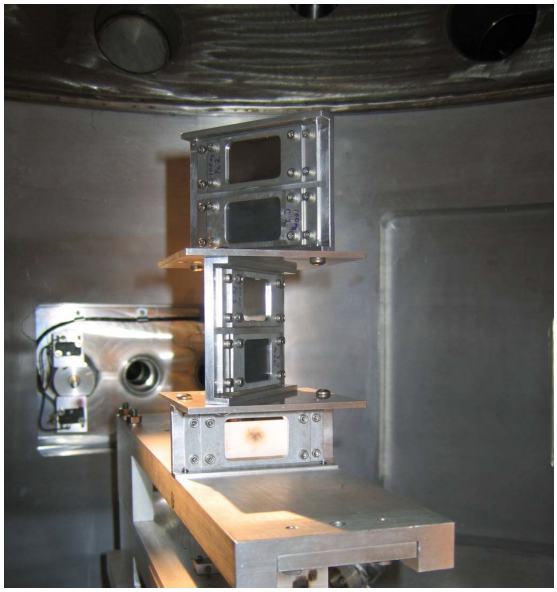

Figure 3.15: E05-110 experiment solid target latter.

The position of the target ladder is vertical in the path of the electron beam. The target system is controlled by three servo motors, each connected to its own motion controller called a BDS. Two of the BDS units are configured as ”Slaves” and are controlled by the third, the ”Master.” The target operator moves the target with the Master BDS through the IOC (input-output controller) during the experiment. The various target positions (Loop1 top cell, Loop1 bottom cell, Carbon target, etc) are stored as 15 encoder values on the control computer (IOC). An encoder attached to the Master's servo motor determines the target position [67]. The target positions for the E05-110 experiment are listed in table 3.3.

Table 3.3: Target Materials and BDS Position.

Target	Material	BDS Position
Loop 1 10 cm	High Pressure He	32932800
Loop 2 15 cm + Pb	He + Pb	26954176
Loop 2 10 cm	He	23377856
Loop 3 15 cm + Pb	H2 + Pb	19802560
Loop 3 15 cm	H2	16241600
Optics	7 carbon foils	12760000
10 cm dummy	2 Al foils	10092480
15 cm dummy	2 Al foils	9370560
Empty	n/a	8653760
BeO	BeO	6406480
Beam right carbon	Carbon	4321550
Beam right iron	Iron	2692366
Beam left carbon	Carbon	585998
Beam left iron	Iron	-1040625

Loop1 target is a 10 cm long and 2 cm diameter cylindrical high pressure He target. The target is made 10 cm long along beam Z. The cell material is aluminum alloy Al 7075-T6 and the length of the cell is 10.00 ± 0.05 cm at room temperature. The upper Loop2 contains He and is a 15 cm long cell at the top with a lead foil in the center slanted $50.0^\circ \pm 2.0^\circ$ beam right. The lower loop2 cell is 10 cm long and just contains He. Both cells are conflat style. The Loop3 target has two 15 cm long cells in the conflat style. The upper cell contains liquid H2 and a lead foil slanted $50.0 \pm 2.0^\circ$ beam right. All of the conflat style cells are made of aluminum alloy Al 7075-T6. The following table shows the cell window and target thicknesses for Loop1, Loop2 and Loop3 [68].

A sub-system for cooling, gas handling, temperature and pressure monitoring is installed along side the targets Loop1, Loop2 and Loop3. The operating temperature is 19 K for the LH_2 target at 0.17 MPa and 6.3 K for the ^4He target at 1.4 MPa. The End Station Refrigrator (ESR) supplies the helium for cooling the targets. The uncertainty in the target density is minimized by monitoring the pressure and temperature with pressure transducers and temperature sensors.

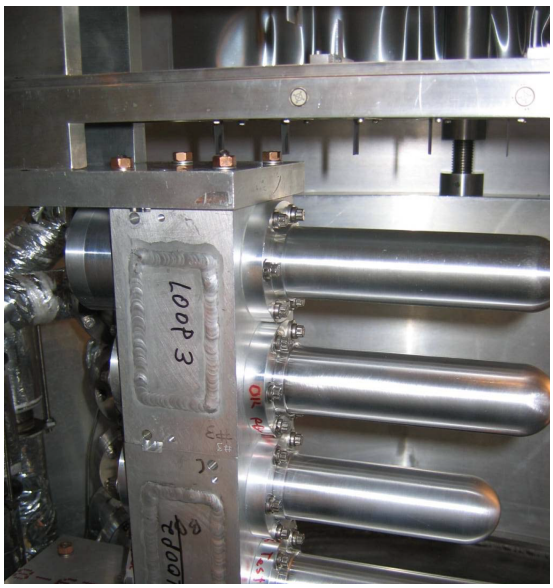

Figure 3.16: The E05-110 experiment cryo targets.

Table 3.4: Cryotargets window and lead target thicknesses

Cryogenic Target	Entrance Window (mm)±0.005	Exit Window (mm) ± 0.005	Lead thickness (g/cm^2)	Beam left wall (mm)	Beam right wall (mm)
Loop1 10cm	0.263±0.008	0.280±0.005	n/a	0.245±0.002	0.239±0.007
Loop2 15cm	0.128±0.002	0.194±0.009	0.1057±0.0001	0.194±0.009	0.194±0.009
Loop2 10cm	0.257±0.005	0.120±0.070	n/a	0.120± 0.070	0.120±0.070
Loop3 15cm	0.129±0.001	0.207±0.005	0.3187±0.0004	0.207±0.005	0.207± 0.005
Loop3 15cm	0.217±0.003	0.115±0.001	n/a	0.115± 0.001	0.115±0.001

The optics target consists of 7 carbon foils cut from the same sheet which is 99.5% chemically pure carbon and has $0.042 \pm 0.001 g/cm^2$ thickness. Foils are separated by 4 cm.

The dummy targets are made of Al 6061-T6 and their thicknesses are $0.259 \pm 0.001 g/cm^2$ [68].

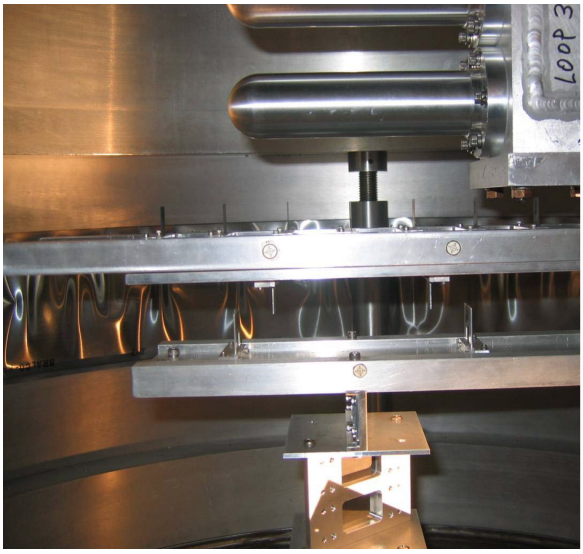

Figure 3.17: The carbon foils that are used for Optics Study.

There are five positions on the solid target ladder. The top position is for BeO and is perpendicular to the beam. The next two positions are for carbon and iron targets and they are slanted 51.78°, so that the downstream faces of the two foils are facing beam right. The bottom two positions are also for carbon and iron targets and they face 48.56° beam left. Table 3.5 gives the target foil positions, thicknesses and chemical purities [68].

Table 3.5: Solid targets purity and thicknesses

Purity	Target Position	Material	Thickness (g/cm^2)
99%	BeO	BeO	0.149 ± 0.001
99.95%	Beam right carbon	Carbon	0.0894 ± 0.0001
99.99%	Beam right iron	Iron	0.1027 ± 0.0001
99.95%	Beam left carbon	Carbon	0.0895 ± 0.0001
99.99%	Beam left iron	Iron	0.1023 ± 0.0001

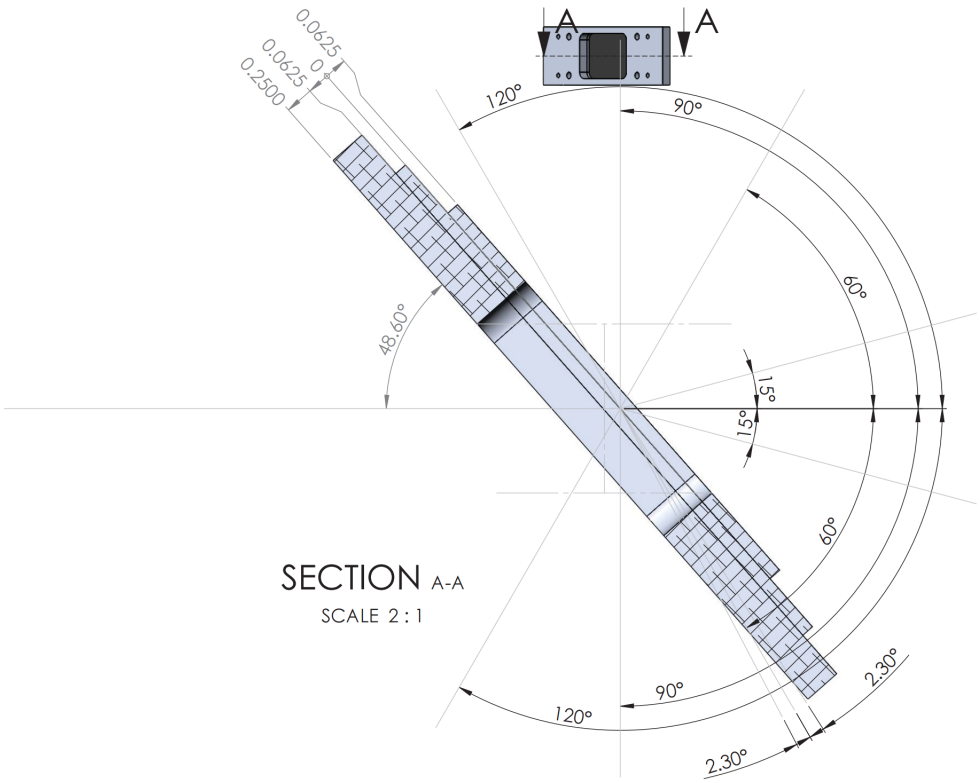

Figure 3.18: Technical drawing of beam left solid target.

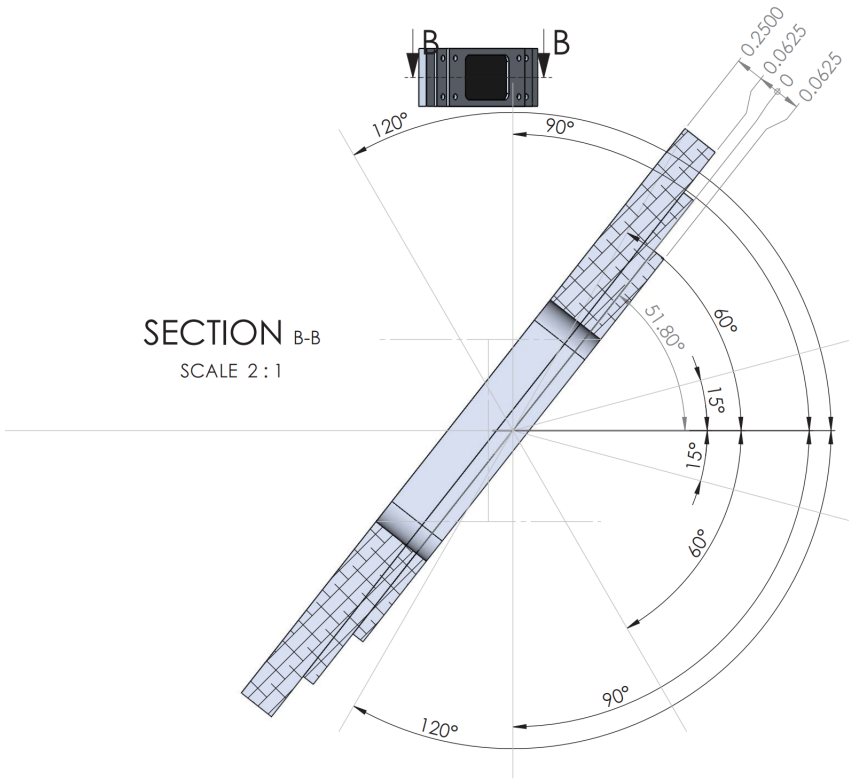

Figure 3.19: Technical drawing of beam right solid target.

3.5 Hall A High-Resolution Spectrometers

Thomas Jefferson lab experimental Hall A is equipped with two high resolution spectrometers that are almost identical : LHRS (Left High Resolution Spectrometer) and RHRS (Right High Resolution Spectrometer). These spectrometers were designed to study electromagnetic interactions and hadronic structure with high precision. Momentum resolution of these devices is better than $2 * 10^{-4}$ and they provide an angular resolution of better than 2 mrad [60]. Basic layout of both spectrometer is shown in Figure 3.20. Important design characteristics of spectrometer are also shown in the Table 3.6 .

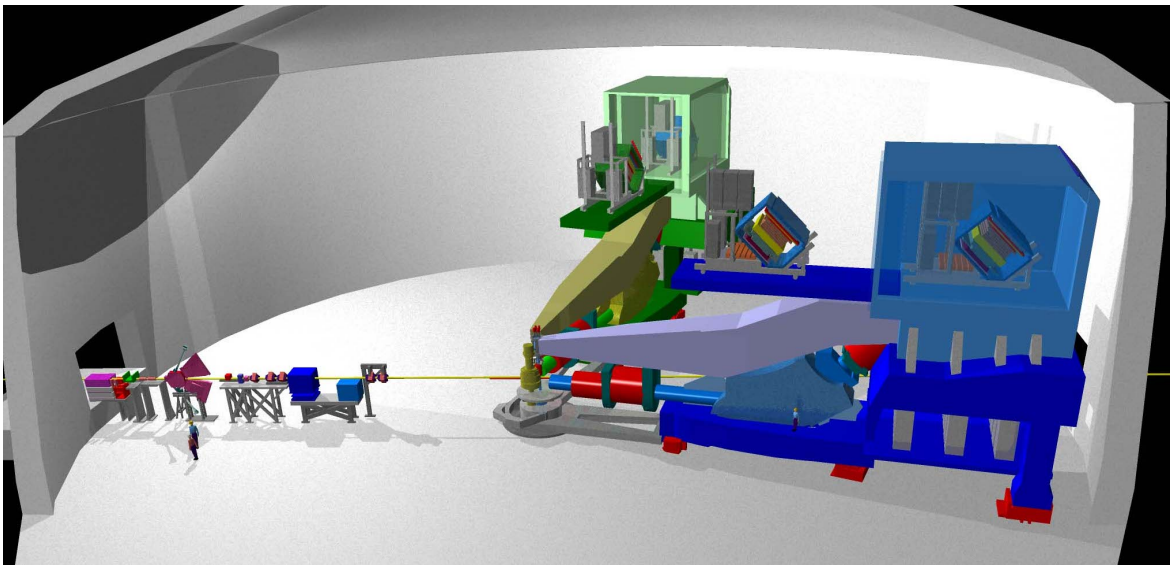

Figure 3.20: The Hall A high resolution spectrometers. Figure from [69].

3.5.1 Design and Characteristics of the Magnets

QQD_nQ magnet configuration is used for both LHRS and RHRS for a number of requirements: a high momentum resolution at the 10^{-4} level over the 0.8 to 4.0 GeV/c momentum range, a large angular and momentum acceptance, good position and angular resolution in the scattering plane, an extended target acceptance and a large angular range [60]. Here, Q stands for quadrupole magnet and D for dipole magnet. The functionality of the dipole

Table 3.6: LHRS characteristics. For more details, see [60].

Configuration	QQDQ
Optical Length	23.4 m
Bending Angle	45°
Momentum Range	0.3–4 GeV/c
Momentum Acceptance	$\pm$ 4.5%
Momentum Resolution ($\delta p/p$)	1×10^{-4}
Angular Range	12.5°–150°
Horizontal Angular Acceptance	$\pm$ 30 mrad
Vertical Angular Acceptance	$\pm$ 60 mrad
Horizontal Angular Resolution	0.5 mrad
Vertical Angular Resolution	1.0 mrad
(Solid Angle)$_{\frac{\delta p}{p}=0,y_0=0}$	6 msr

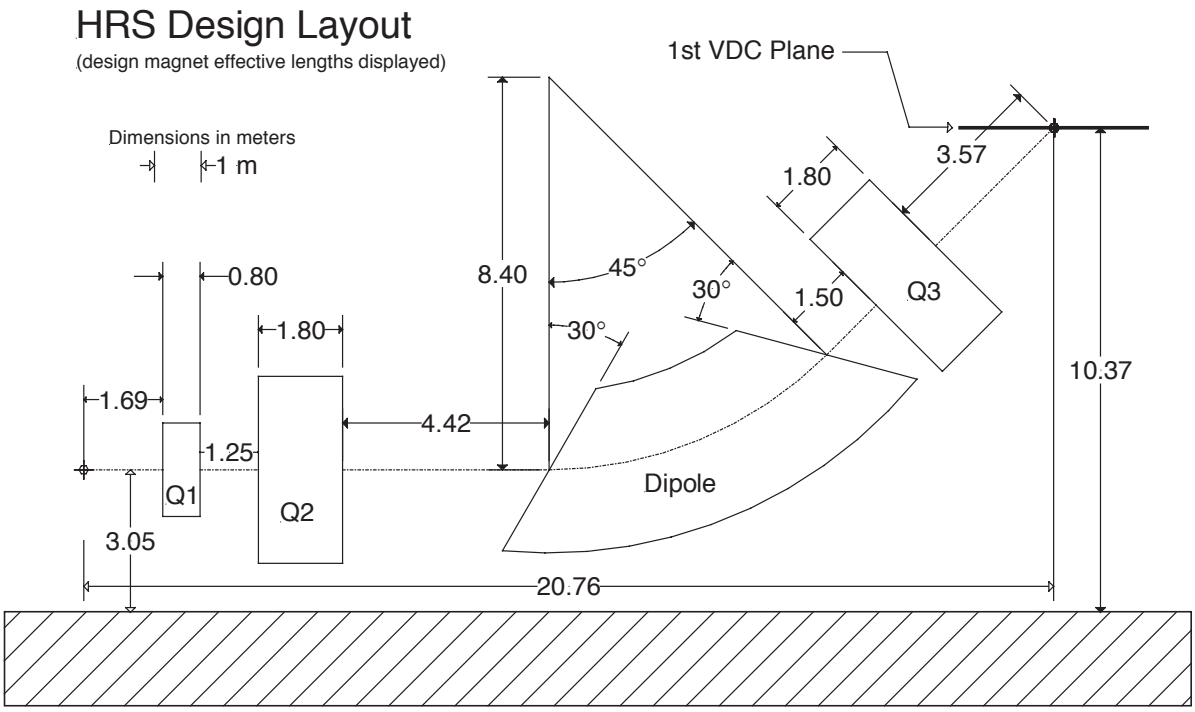

Figure 3.21: The design layout of the LHRS. Figure reproduced from [60].

magnet is bending the scattered particles 45°, while quadrupole magnets are used to focus the scattered particles just like an optical lens. The main functionality of the two quadrupoles in front of the dipole is to achieve desired angular acceptance and produce a parallel beam in the radial plane. The third quadrupole accomodates extended targets.

Bending beam 45° is due to geometry of the spectrometers. The focal plane is at 45° with respect to central trajectory.

There are a total of eight superconducting magnets in the two spectrometers. Each of these magnets has independent cryogenic controls and reservoirs. The 1800 W helium refrigerator ESR feeds the cryogenic system.

3.5.2 Collimators

Each spectrometer has a set of collimators. They are located 1.109±0.005 m away from the target on the left spectrometer and 1.101 ±0.005 m from the target on the right spectrometer. The first two collimators are made of 80 mm thick tungsten. The dimensions for the first collimator is 121.8 x 62.9 mm at the entrance face and 129.7 x 66.8 mm at the exit face. The second collimator is smaller and has 50.0 x 21.3 mm dimensions at the entrance face and 53.2 x 22.6 mm at the exit face. The third collimator is called *sieve slit* which is used to study optics of each HRS. The sieve slit is made of 5 mm thick stainless steel and positioned 75 mm away from the target than the other collimators. There are 49 holes (7*7) that are spaced 25 mm apart vertically and 12.5 mm apart horizontally. 47 of the holes are 2 mm in diameter. The other two holes , one in the center and one displaced two rows vertically and one horizontally , are 4 mm in diameter [60].

3.5.3 Optics of the High Resolution Spectrometers(HRS)

The optics of the HRS is different from traditionally known optics of lenses. It is a mathematical expression that is related to the properties of the HRS magnets. The positions and angles of the scattered particles are determined at the focal plane by a pair of Vertical Drift Chambers (VDCs). The optics matrix of HRS allows the reconstruction of the scattering vertex from the focal plane coordinates.

Two different target variables are used for optics matrix optimization : Theoretical and Experimental target variables. The theoretical target variables are reconstructed from the

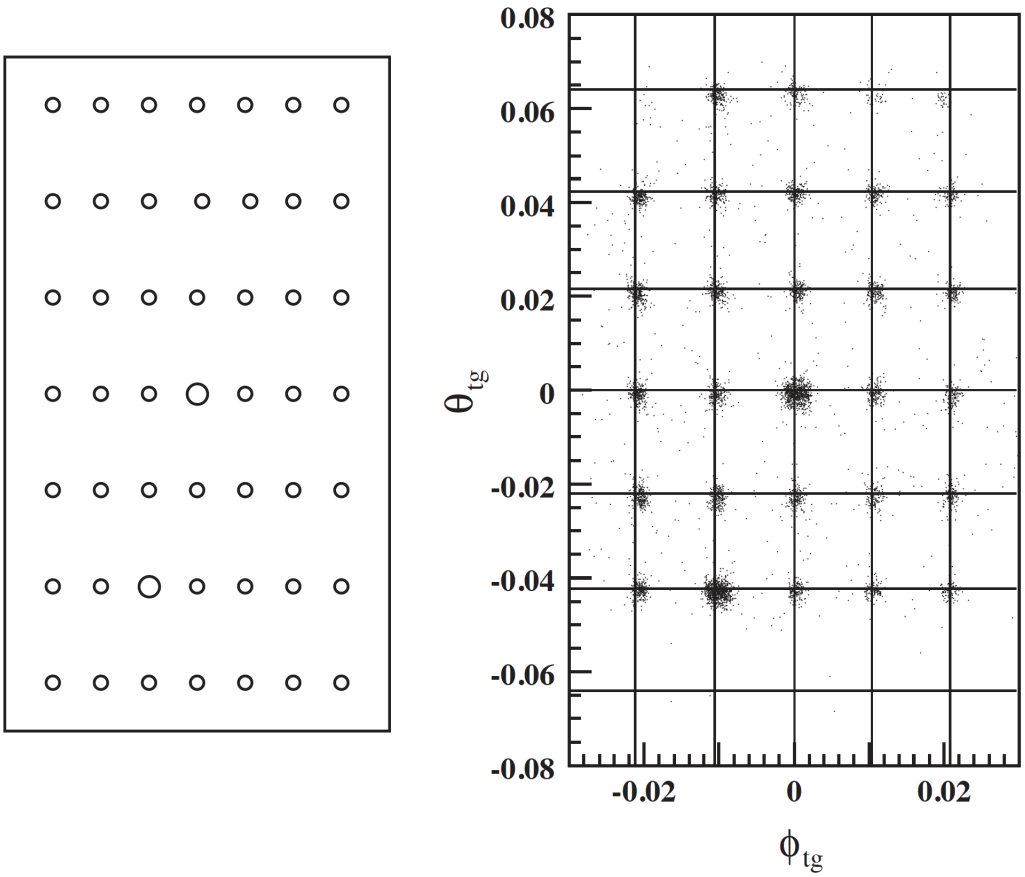

Figure 3.22: Geometric and reconstructed configurations of the sieve slit [60].

geometry and survey information and the experimental target variables are reconstructed from focal plane variables by using optics matrix (see (Sect. 3.3.1)). The optix matrix is optimized by setting the χ^2 of difference between experimental and theoretical values the smallest.

Optics run data was taken with carbon foil targets and sieve slit for the experiment E05-110 (see Figure 3.17). Optics matrix optimization study for E05-110 experiment is done by Huan Yao and checked by Kai Jin with an independent analysis. E05-110 experiment has a wide spectrometer momentum settings from 0.1 GeV/c to 4.0 GeV/c. This wide momentum settings required to use more than one optics matrix. Optics data was taken at four different incident electron energies: 400, 645, 740, 1102. However, beam raster was accidentally on for the 645 and 740 MeV beam energies which made a bad track reconstruction quality.

But , 1102 MeV optics came out to be not much different than 645 and 740 MeV optics. Thus only two sets of optics used in this analysis : 400 and 1102 MeV. The 400 MeV optics called low energy optics and used for momentum settings below 450 MeV, while 1102 MeV optics is called high energy optics and used for momentum settings above 450 MeV.

3.6 Detector Packages

The LHRS and RHRS contain a number of detectors which are located in the shield hut at the end of the magnet configuration. The LHRS is composed of the Vertical Drift Chambers, the S1 and S2 scintillating planes, the NaI calorimeter, the gas Cherenkov and the pion rejectors. The NaI is not included in the standart detector configuration of the LHRS. It was installed just for the E05-110 experiment. Unfortunately, some of the blocks were unresponsive during the experiment. Therefore, the NAI was only used for background study and cross check, but not used in the main electron events selection. The RHRS is composed of the the Vertical Drift Chambers, the S1 and S2 scintillating planes , the gas Cherenkov, the pre-shower calorimeter and the shower calorimeter. The layout of the LHRS and RHRS detector packages are shown in Figure 3.6. The detectors that were used in this analysis are explained in detail below.

3.6.1 Vertical Drift Chambers and Tracking

Each HRS uses a vertical drift chamber (VDC) to reconstruct particle trajectories precisely. Each VDC has a U-V plane configuration, where both planes are orthogonal to each other and lie in the horizontal plane of laboratory. The tracking information from VDC and the spectrometer optics information together is used to reconstruct the angle, position and momentum of the particles in the target system. There are 368 gold plated sense wires in each plane. They are inclined at an angle of 45°with respect to the scattered particle

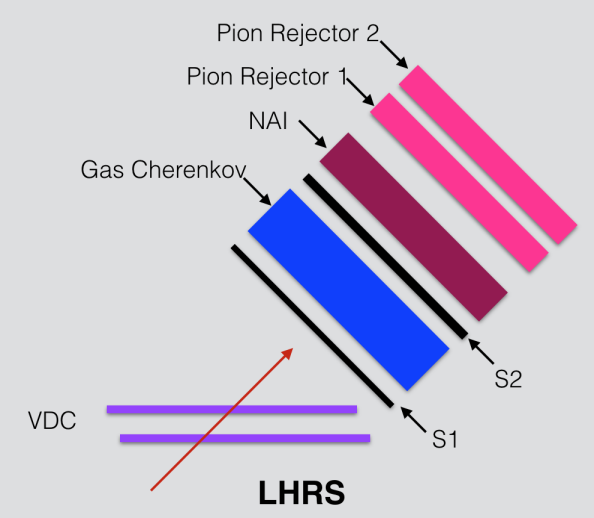

Figure 3.23: The LHRS detector package. Figure adapted from [66].

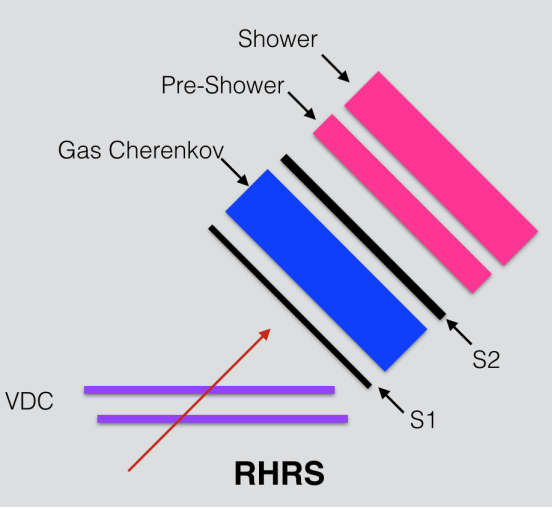

Figure 3.24: The RHRS detector package. Figure adapted from [66].

trajectory(see Figure 3.25) [70]. The spacing between two adjacent wire is 4.243 mm.

The distance between U and V planes is 26 mm. VDC chambers are seperated by 335 mm and filled with 62% argon and 38% ethane gases.The gas is bubbled through cooled alcohol to reduce aging effects on the sense wires [60]. For each spectrometer gas supplied to each VDC independently.

Each particle crosses an average thickness of $7.8x10^{-4}$ radiation lengths (X_0) in each

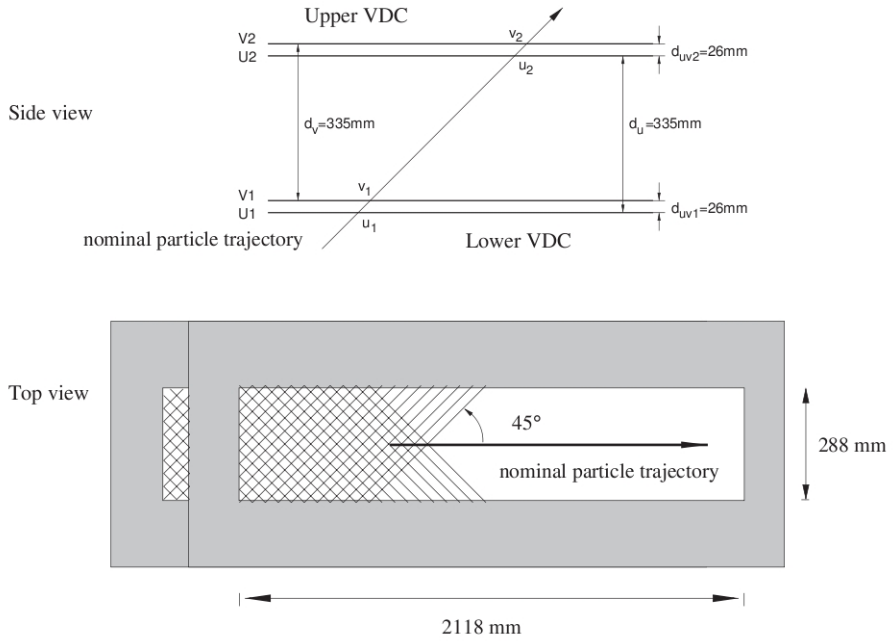

Figure 3.25: Schematic layout of the U and V planes of the VDCs. Figure from [71].

VDC. The biggest contribution to the multiple scattering comes from Ti window ($5x10^{-3}$ X_0) at the exit of the spectrometer vacuum. A typical on-line analysis of the wire efficency is shown in Figure 3.26.

The VDC chambers are hold at high voltage: the cathode plane is hold at -4 kV and the wires are hold at ground. High Voltage is provided to each VDC by a single channel of a Bertan 377N HV power supply [70].

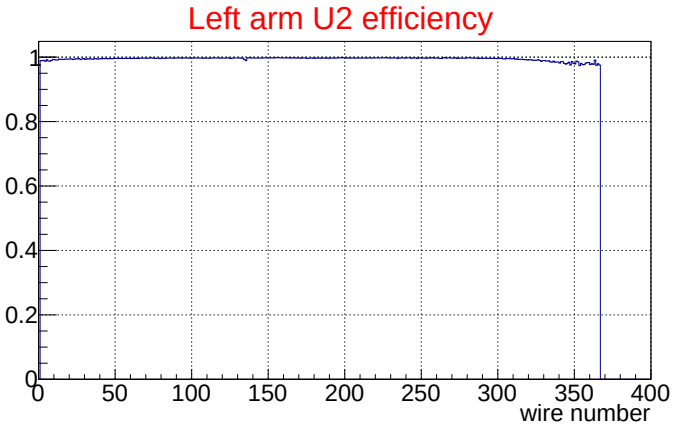

Figure 3.26: Wire efficency of VDC U2 plane as a function of wire numbers for run 4215

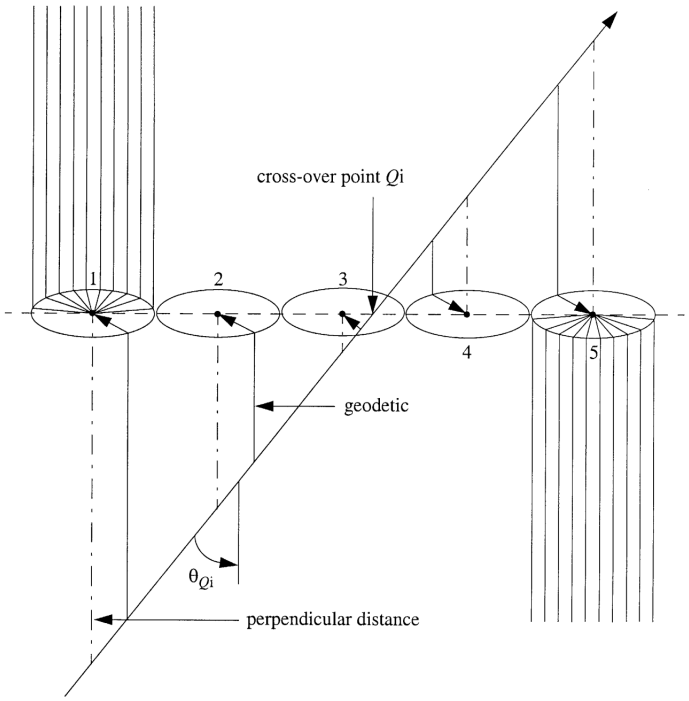

Figure 3.27: Electric field lines between the high-voltage cathode planes in the LHRS VDCs. Figure from [71].

The passage of a charged particle through a VDC plane is shown in Figure 3.27. When a charged particle goes through the gas medium, it causes ionization. Ions and generated electrons are then drifted with almost constant velocity along the electric field between sense wires. Intense electric field in the region close to wires accelerates g;drifting electrons and causes more ionization. This makes an electric signal on the sense wires (hit). The timing information of the signals are sent to Time to Digital Converters (TDCs) [71]. Good tracks cross the VDCs at an angle of 45° because of the HRS design [60]. A particle passing through VDCs will have signal on 5 wires usually, however, because of the inefficiencies in the wire signals , signals from 3 wires are considered to be a good track [66]. A single-track corresponds to the track reconstructed with a good signal from per plane. However, sometimes more than one track can be reconstructed for the same eventi (multi-track event) due to number of reasons which will be explained in multi-track correction analysis.

In this analysis, a cut for single tracks is used to select good electrons. Thus, an efficiency associated with the cut is calculated considering the multi-tracks as well (See 4.1.1.4).

3.6.2 Scintillators and Triggering

A trigger system is used in all scattering experiments to decide which events in a detector to keep. Experiments are usually searching for particular type events and trigger systems are used to identify and save those events for an offline analysis [72].

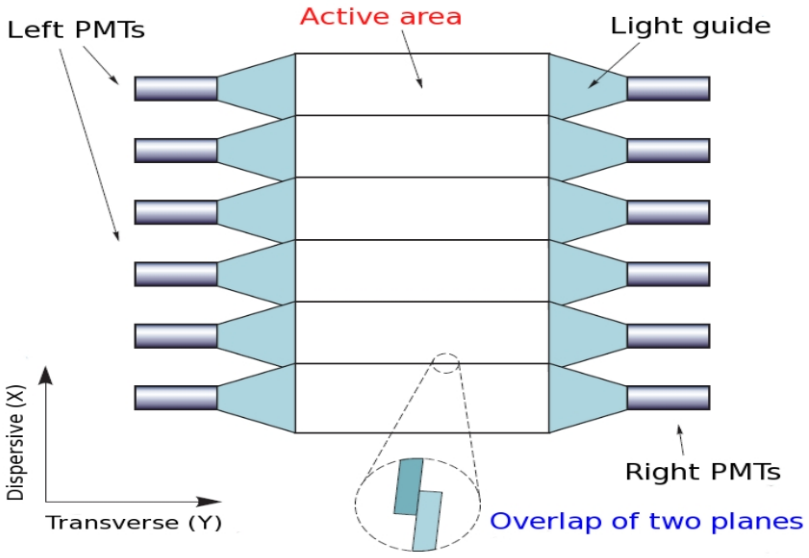

Figure 3.28: The S1 scintillator plane. Figure from [62].

In Hall A, there are two trigger scintillator planes for each HRS arm (S1 and S2) and each plane has a time resolution of 0.30 ns (σ). They are sepated by 2 m and each plane has six overlapping paddles made of thin plastic scintillator (5 mm BC408). Each paddle is attached to two Burle 8575 model photomultipliers (PMTs). The dimensions of the active volume of S1 is 36.0 cm (length) x 29.3 cm (width) x 0.5 cm (thickness) and of S2 is 60.0 cm x 37.0 cm x 0.5 cm. S1 scintillator plane is shown in Figure 3.28.

When charged particles goes through the scintillator planes, it generates light inside paddles. This light is collected by PMTs at both ends of paddles and the intensity and time

information of the light are recorded by ADC and TDC modules.

Traditionally, trigger system of HRS works as a start-stop watch. When particles hit on a paddle of S1 plane the counter starts and when they hit S2 plane counter stops and forms a trigger. More specifically, when a particle hits on a paddle of S1, PMTs on both sides of paddle will generare ADC and TDC signals which will form a logic signal for S1 plane. If one of the paddles of the S2 plane also fired it will create a logic signal too. Signals from both S1 and S2 will form the main trigger.

The main trigger for LHRS is T3 and for RHRS is T1. When one paddle of either S1 or S2 planes fires and at the same time the gas Cherenkov fires, T2 (T4) triggers will form. T2 (T4) triggers are formed for RHRS (LHRS) either by cosmic ray events or particles on the edge of acceptance. Figure 3.29 shows how the main triggers formed. T5 trigger is the main trigger for coincident experiments and not used for E05-110 experiment.

3.6.3 Gas Cherenkov

The gas Cherenkov detector is a particle identification detector (PID) and plays a crucial role to seperate scattered electrons from pion background in this analysis. If a charged particle enters a medium, which has the index of refraction $n > 1$, with a speed greater than the speed of light in the same medium , it emits a radiation called the Cherenkov radiation (after Pavel Cherenkov, who first observed the effect in 1934) [73]. The requirement for the Cherenkov radiation is :

$$\beta \geq \frac{1}{n},$$
$$\beta = \frac{v}{c}$$

v is the speed of the particle in the medium and c is the speed of light in the vacuum.

Huygen's wave construction can be used to determine the direction of the emitted light

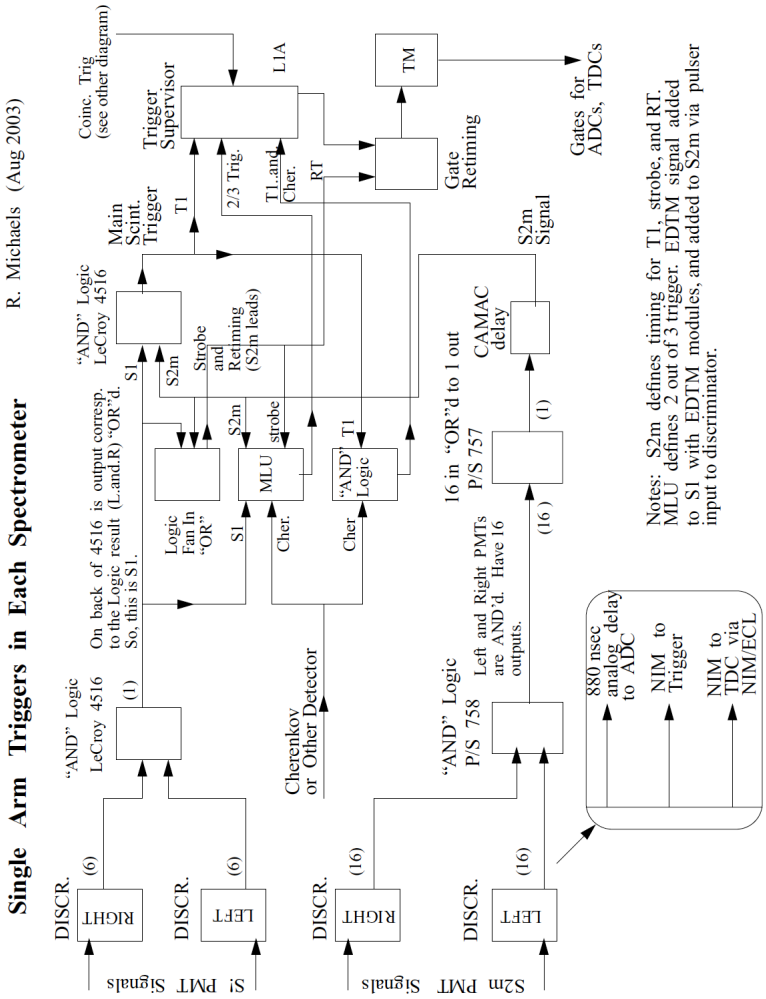

Figure 3.29: Diagram for how main triggers for L-RHRS formed. Figure from [66].

clasically. The emitted light has a spectrum of frequencies, with the most interesting component being in the blue and ultraviolet band of wavelengths. The blue light can be detected by using photomultiplier tubes and ultraviolet light can be converted to electrons using photosensitive molecules [73]. The Cherenkov angle θ_c is the angle of the emitted radiation relative to the particle direction and can be shown as :$cos\theta_c = 1/\beta n$.

The gas cherenkov is used to separate e^- from π^- background [60]. Thus, it is important to find the threshold momentum to trigger the Cherenkov detector for the pion and the electron. This can be calculated with the expression for the energy :

$$
\begin{aligned}
E = \gamma mc^2 &= \sqrt{m^2c^4 + p^2c^2} \\
\gamma &= \frac{1}{\sqrt{1-\beta^2c^2}}
\end{aligned}
$$

$$
p = \frac{mc}{\sqrt{n^2-1}}. \tag{3.9}
$$

From this equation, the threshold momentum for an electron and pion can be calculated for CO_2 medium with $n = 1.00043$ [62].

$$
\begin{aligned}
p^{\pi^-}_{\text{min}} &= 4.77 \text{ GeV} \\
p^{e^-}_{\text{min}} &= 17.4 \text{ MeV}.
\end{aligned}
$$

The kinematics of E05-110 experiment is $0.1GeV \leq p \leq 4GeV$. Therefore , it has a great ability to identify particles. The electron detection efficiencies are higher than 99% .

The gas cherenkov detector in Hall A is filled with CO_2 at atmospheric pressure and mounted between scintillator planes S1 and S2. It has ten spherical mirros with $80cm$ focal length, each seen by a PMT (Burle 8854). The length of the particle path in the gas medium is $130cm$ for the RHRS Cherenkov , leading to an average of twelve photoelectrons. For the LHRS path length is $80cm$, yielding seven photoelectrons on average. The total amount of material in the particle path is about 1.4% X_0 (radiation length) [60] .

Cherenkov radiation collected by Each PMT is sent to Analog to Digital Converter (ADC) unit. Total signal produced by the particle is summation of each individual PMT signal. Even though the pions can not fire the gas Cherenkov, they can still ionize the atoms of the gaseous medium and produce electrons with enough energy to trigger the detector. These electrons are called knock-on electrons and their distribution has a peak at the one

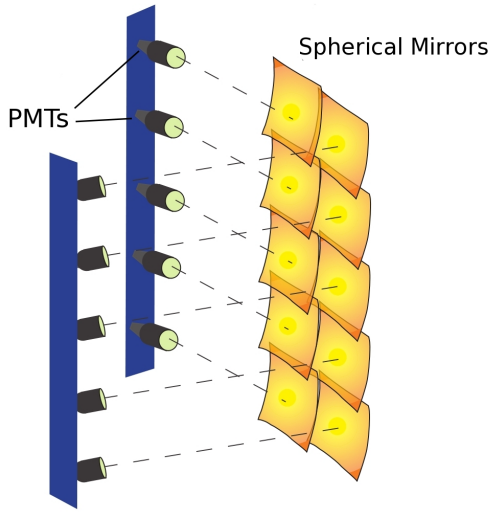

Figure 3.30: The gas Čerenkov in the LHRS. Figure from [62].

photo -electron peak [62]. These electrons are removed from analysis with an ADC cut which will be discussed further in the Cherenkov efficiency section. A schematic picture of the gas Cherenkov in the LHRS is given in Figure 3.30.

3.6.4 Shower Detectors

Shower detectors are used in Hall A for particle identification alongside with the other detectors (Cherenkov). Combination of shower detectors and Cherenkov allow to have an excellent PID and pion rejection. The pion rejection ratios for the Hall A shower calorimeters is better than 99%. Combination of Cherenkov and shower detectors have pion rejection ratios better than 99.9%.

Standard detector configuration of each HRS consists of two layers of shower detectors: Pre-shower calorimeter and shower calorimeter. However, a NaI calorimeter was used in LHRS instead of shower calorimeters which aimed to have a better control of background particles at low momentum settings. The blocks in the first layer in RHRS are perpendicular to the particle tracks and in the second layer are parallel to the tracks. The first layer in RHRS is composed of 48 lead glass blocks with 10 cm x 10 cm x 35 cm dimenions. The

second layer is composed of 80 lead glass blocks with 15 cm x 15 cm x 35 cm dimensions [60]. A schematic picture of the shower calorimeter in the RHRS is shown in Figure 3.31.

High Voltage (HV) is used across the photomultiplier tubes and bases, which are mounted on the back of shower and on the side of pre-shower calorimeters. When charged particle pass through the lead glass in shower calorimeters, e^+e^- particle pairs are created. These particles then create additional particles and Cherenkov light. PMTs collect created particles and Cherenkov light signal and send it to ADC modules [74].

Shower calorimeters measure the energy deposited by the incoming particle. The output signal of shower calorimeters is linearly proportional to the energy loss of incoming particle. Particles can be identified by looking at the energy deposited in the calorimeter [74].

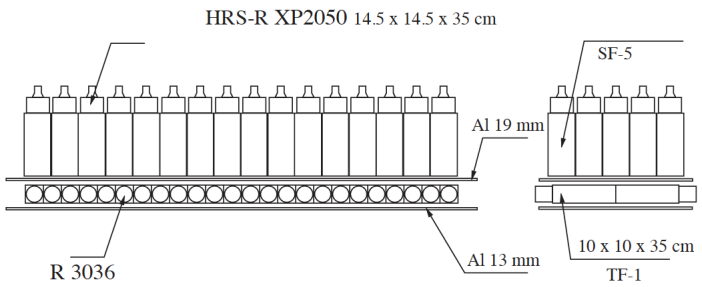

Figure 3.31: Shower detectors in the RHRS. Particles enter from the bottom of the figure. Figure from [60].

3.7 Data Acquisition

A data acquisition system (DAQ) consists of the software and hardware that digitizes signals collected from detectors and other monitors and saves it for an offline analysis. The data acquisition systems in Hall A use CODA (CEBAF On-line Data Acquisition System). CODA is a toolkit of distributed software components developed by the JLab data acquisition group which controls DAQ hardware elements such as VME digitization devices

(ADCs, TDCs, scalers). The read-out controller (ROC) is the most important component of CODA which runs on the front-end crates, the event builder (EB) and event recorder (ER), the event transfer (ET) system and the Run Control process, from which users can select different experimental configurations, start and stop runs, as well as reset and monitor CODA components (see Figure 3.32) [60].

A run is the data that is recorded for a specific kinematics. It is not possible to continuously take data as a single piece for different kinematic settings, instead it is divided into runs. ROC gathers data from the front-end boards for each event and sends to EB and after event is built , ER writes data to a local disk. The data are then written to tapes in the Mass storage system (MSS) and erased from local disk typically after one day [60].

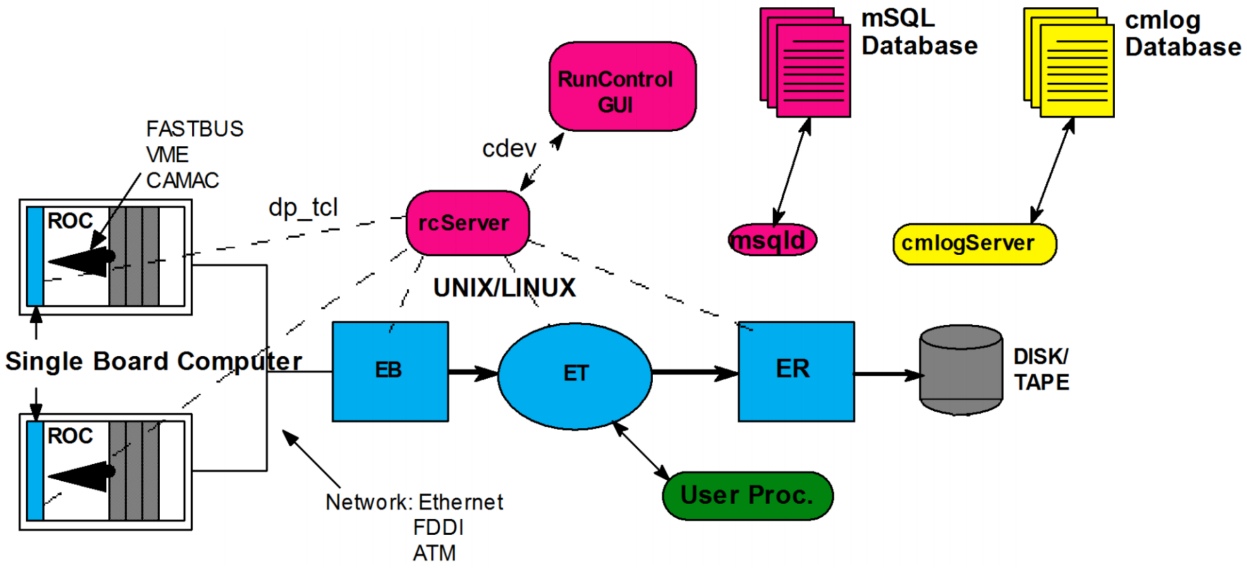

Figure 3.32: CODA components. Figure reproduced from [75]

Scalers events count raw signals from phototubes. Scalers also count important quantities like charge and triggers which are used for cross section normalization.

The Experimental Physics and Industrial Control System (EPICS) is a collection of code and documentation which is built by a collaboration of more than 70 labaratory, university and industrial facilities [76]. The main purpose of EPICS is to control detectors

and devices via a graphical user interface (GUI).

3.8 Analysis Software

ROOT [77] is the main software package that has been used during the analysis of E05-110 experiment. Root is an object-oriented program and library developed by CERN for particle physics data analysis. Root library is written with C++ programming language and consists of many useful physics functions. It is a very powerful tool for particle physics data analysis.

At Jefferson Lab Hall A, a software package called Analyzer [78] is used to process raw experimental data. The analyzer is built on the top of ROOT. The analyzer converts TDC and ADC signals that are collected from different detectors and converts into a meaningful data that explains physical properties of particles. The analyzer analyzes the recorded raw data during the experiment and writes to a root file that can be used by ROOT. In order to use analyzer, a script called Replay is used. Replay uses optics matrix, detector calibration coefficients and run database to create root files. There is one root file for every run number. These root files consist of histograms of detector responses and kinematics variables such as Cherenkov ADC signals, W^2 and Q^2. These root files are used to extract cross sections for each kinematics.

3.9 Kinematics of the E05-110 Experiment

E05-110 experiment aimed extract Coulomb Sum Rule (CSR) in the momentum transfer range $0.55 GeV/c \leq |\ \overrightarrow{q}\ | \leq 1.0 GeV/c$ with a significantly better precision than previous measurements. In order to calculate CSR, longitudinal response functions has to be extracted via a method known as Rosenbluth separation. The Rosenbluth separation requires measurement of cross sections at two or more angles at a constant $\overrightarrow{q}$. Four different angles were used for E05-110 experiment. Having more than two angles enables to check any

angle dependent systematic errors [59]. The most forward angle was chose to be 15° and backward angle 120°. This allowed for the largest Rosenbluth lever arm within a single experiment compared to all previous experiments. The other two angles are : 60° and 90°.

Both Rosenbluth separation and radiative corrections require an interpolation procedure since it is not possible to measure data at every kinematic setting. To have as much covarage as possible in (q, ω) to reduce systematic uncertainties in the interpolation procedure, data was taken at beam energies from 400 MeV to 4 GeV and at scattered energies from 100 MeV/c to 4 GeV/c. Figure 3.33 shows actual kinematic settings of E05-110 experiment.

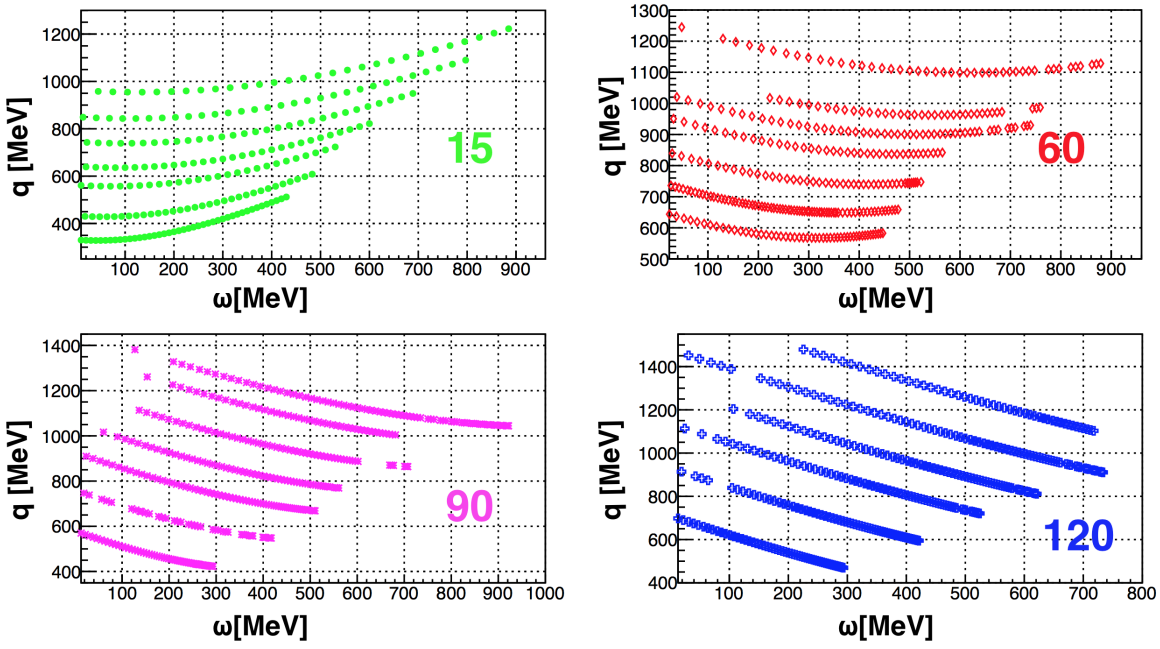

Figure 3.33: Kinematics setting of E05-110 experiment. Each color represents a different angle and each line represents a different beam energy. The y axis is three monetum transfer q (MeV) and the x axis is energy loss ω (MeV).

CHAPTER 4

DATA ANALYSIS

In this chapter, we will explain the data analysis of the E05-110 experiment. We will first discuss the extraction of the raw cross sections. We will then explain the background correction, the acceptance and the radiative corrections. Finally, we will talk about the procedure of the Rosenbluth separation and the extraction of the CSR. The analysis procedure of the E05-110 experiment is summarized in Figure 4.1.

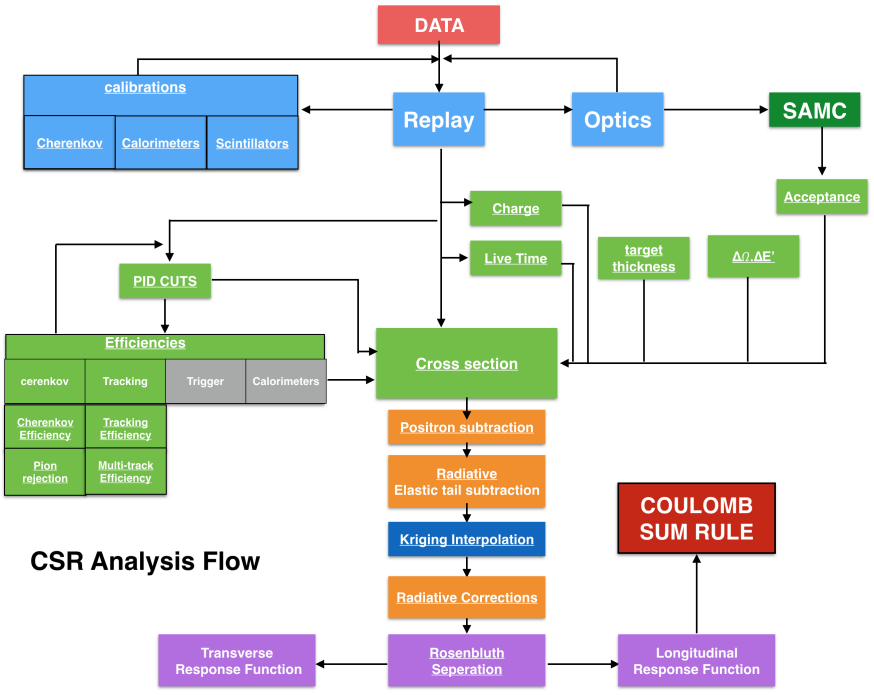

Figure 4.1: The analysis procedure of the E05-110 experiment.

4.1 Experimental Cross Sections

The E05-110 experiment aimed to measure the longitidunal and the transverse response functions to extract the Coulomb Sum Rule (CSR). In order to extract the CSR accurately, the cross sections have to be calculated with great care. In this section we will discuss the extraction of the cross sections.

4.1.1 Calculation of Raw Cross Section

The theoretical cross sections can be calculated by using Equation 1.10. However, the experimental cross sections were extracted by using the formula given below:

$$\frac{d^3\sigma_{\text{raw}}}{d\Omega dE'} = \frac{N_{\text{cut}}}{(Q/e).t_{LT}.A.\varepsilon.\chi}\frac{1}{\Delta E'.\Delta\Omega}, \tag{4.1}$$

Each of the quantities in this equation are:

- N_{cut} is the number of the electrons that pass all the analysis cuts. The analysis cuts are explained in detail in the subsection Section 4.1.1.1.

- Q/e is the number of beam electrons. Q is the total charge of each run which is extracted from the BCM scaler. If we divide the accumulated charge by the e (charge of the electron), we will get the total number of beam electrons. The calculation of Q is given in subsection Section 4.1.1.2.

- t_{LT} is the live time which is 1- dead time. When an event generates a trigger, it is sent to the DAQ and then saved. However, sometimes some of the triggers are not saved due to the high trigger rates. The live time correction counts for the triggers that were not saved. Equation 4.2 was used to calculate the live time. T1 and T3 are the main trigger event types for the right and left arm respectively. Live time is explained in detail in Section 4.1.1.3.

$$t_{LT} = \frac{PS \times N_{T1(3)}}{Ntrigger_{total}} \tag{4.2}$$

- ε is the product of all detector (cut) efficiencies. In this analysis we only have Cherenkov and multitrack efficiencies. In subsection Section 4.1.1.4 these efficiencies are explained in detail.

- A is the spectrometer acceptance which was determined from a Monte Carlo simulation code, called Single Arm Monte Carlo (SAMC). The acceptance of the HRS is defined as the ratio of the number of events detected at the focal plane in the VDC to the number of particles generated at the target. The acceptance calculation is explained in Section 4.1.1.5.

- χ is the number of the target particles which is defined in Equation 4.3. σ_A is the target thickness (g/cm^2 and N_a is the Avagadro's number ($6.02x10^{23}$), θ_r is the target rotation angle and gA is the atomic number of the target.

$$\chi = \frac{\sigma_A N_a}{Cos(\theta_r) gA} \tag{4.3}$$

- $\Delta E'^*$ is the energy width in MeV for the given momentum bin being studied.

- $\Delta\Omega$ is the solid angle that is defined by the width of the acceptance cuts $\Delta\theta$ and $\Delta\phi$. In this analysis $\Delta\theta = 0.08mrad$ and $\Delta\phi = 0.04mrad$.

$$\Delta\Omega = \Delta\theta\Delta\phi \tag{4.4}$$

We will now discuss each quantity in detail:

*$\Delta E' = 2\delta p/p \cdot p_0$ where $\delta p/p$ is the half-width of the $\delta p/p$ cut in percent and p_0 is the LHRS momentum setting.

4.1.1.1 N_{cut}

In an electron scattering experiment, cosmic background and secondary particles which are generated in scattering processes, are also detected in addition to the scattered electrons by the experimental apparatus. To extract clean cross sections of the scattered electrons, we need to eliminate these particles. This is done by a set of good electron cuts. The cuts, which are used in this analysis to select good electrons, are given for both LHRS and RHRS in Figure 4.2.

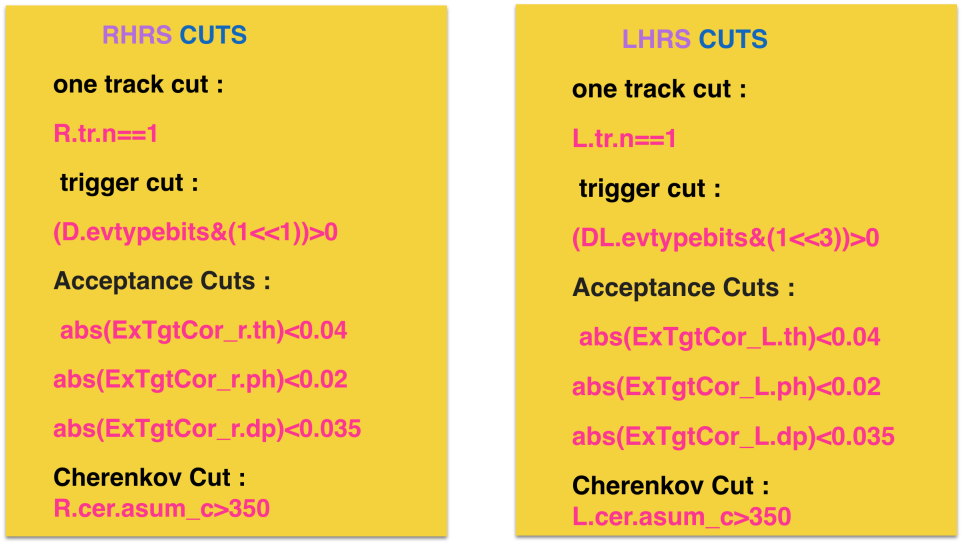

Figure 4.2: Good electron cuts used for LHRS and RHRS

- $R(L).tr.n == 1$: This cut excludes events with multi tracks and zero track and selects events with only one track. Using this cut requires an efficiency study for the good events excluded. The number of excluded good electrons needs to be found and accounted for. This study will be explained in the tracking efficiency section.

- $(D(L).evtypebits\&(1 << 1(3))) > 0$: This cut selects triggered events by the main trigger.

- $abs(ExTgtCor\_r(L).th) < 0.04 \& abs(ExTgtCor\_r(L).ph) < 0.02 \& abs(ExTgtCor_r(L).dp) < 0.035$: These cuts are used to select the particles that fall within the acceptance win-

dow. The θ and ϕ cuts are used to select events within the angular acceptance and the $\delta P/P$ cut is used to select events within the momentum acceptance. The distributions of θ, ϕ and $\delta P/P$ are given in Figure 4.3.

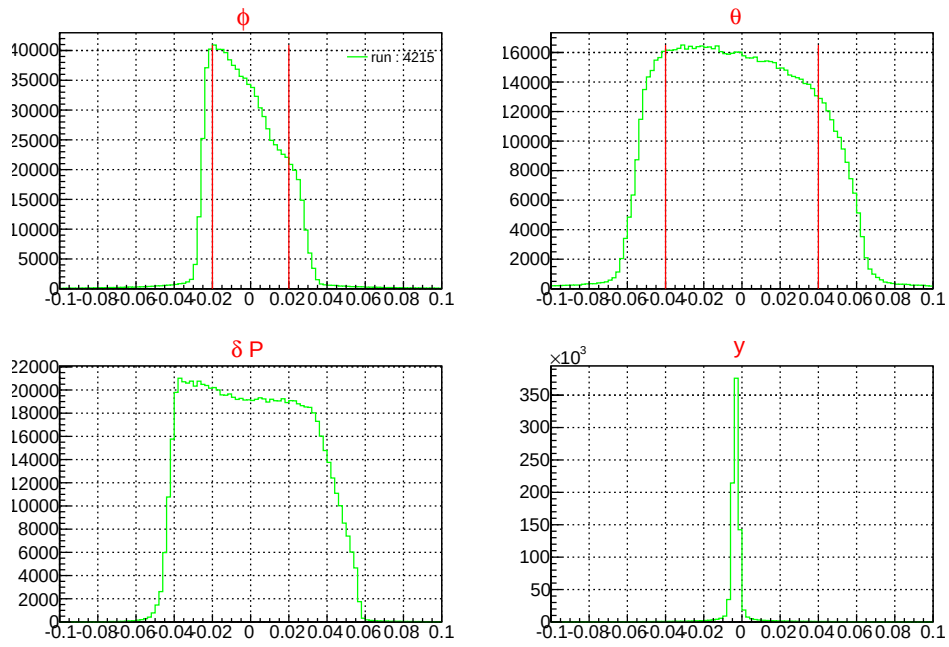

Figure 4.3: Target variables for run 4215.

- $R(L).cer.asum\_c > 350$: This cut selects events that have Cherenkov ADC values greater than 350. The main goal of this cut is to select good electrons and reject pion background. However, it is not possible to separate electrons from pions with just one cut. There will be still some pions leaking in the good electrons and some of the good electrons will be lost. In order to count for the electrons lost and the pions leaked in, an efficiency study was performed. We will discuss this in the Cherenkov efficiency section.

4.1.1.2 BCM Calibration and Calculation of the Charge

The beam Current Monitor (BCM) calibration is done in two parts:

- EPICS Calibration: The EPICS calibration provides a precise beam current measurement. A special calibration run is recorded for different current settings. Using this

calibration run, current values from the OLO2 cavity monitor and the Faraday cup are compared. During the calibration run, $I_{Faraday}$, I_{OLO2} and the average voltage values of the BCM cavities (upstream, downsteam) are measured simultaneously. The I_{OLO2} and $I_{Faraday}$ comparison is shown in Table 4.1. The difference between the two values are less than 1% for current values higher than 1μA (see Figure 4.4). Since the current values for the E05-110 experiment are from 5μA to 60μA, this proves that the OLO2 cavity is precise enough to be used for calibration.

Table 4.1: I_{OLO2} and $I_{Faraday}$ comparasion

$I_{OLO2}(\mu A)$	$I_{Faraday}(\mu A)$	%difference
59.491±0.245	59.318±0.177	0.29
39.160±0.049	39.048±0.068	0.29
19.594±0.033	19.472±0.012	0.62
10.810±0.039	10.723±0.051	0.81
5.038 ±0.007	5.034 ±0.01	0.06
2.171 ±0.008	2.164 ±0.005	0.33
1.017 ±0.002	1.019 ±0.017	0.27
0.542 ±0.002	0.549 ±6E-4	1.20
0.259 ±4E-4	0.263 ±5E-5	1.50

The EPICS calibration constants for upstream and downstream are calculated by the ratio of I_{OLO2} and $V_{u,d}$ as shown below (see Figure 4.5):

$$Constant_{EPICS} = \frac{I_{OLO2}}{V_{u,d} - offset}, \tag{4.5}$$

where "offset" refers to the offset of the BCM cavities and is determined from the beam off period. I_{OLO2} and $V_{u,d}$ values are extracted from the bcmlog_132 file.

After the EPICS calibration constants are calculated, the average beam current can be calculated from Equation 4.6.

$$I_{average} = Constant_{EPICS} * (V_{u,d} - offset), \tag{4.6}$$

- Scalers Calibration: in order to extract the beam charge, six RF cavities scaler signals

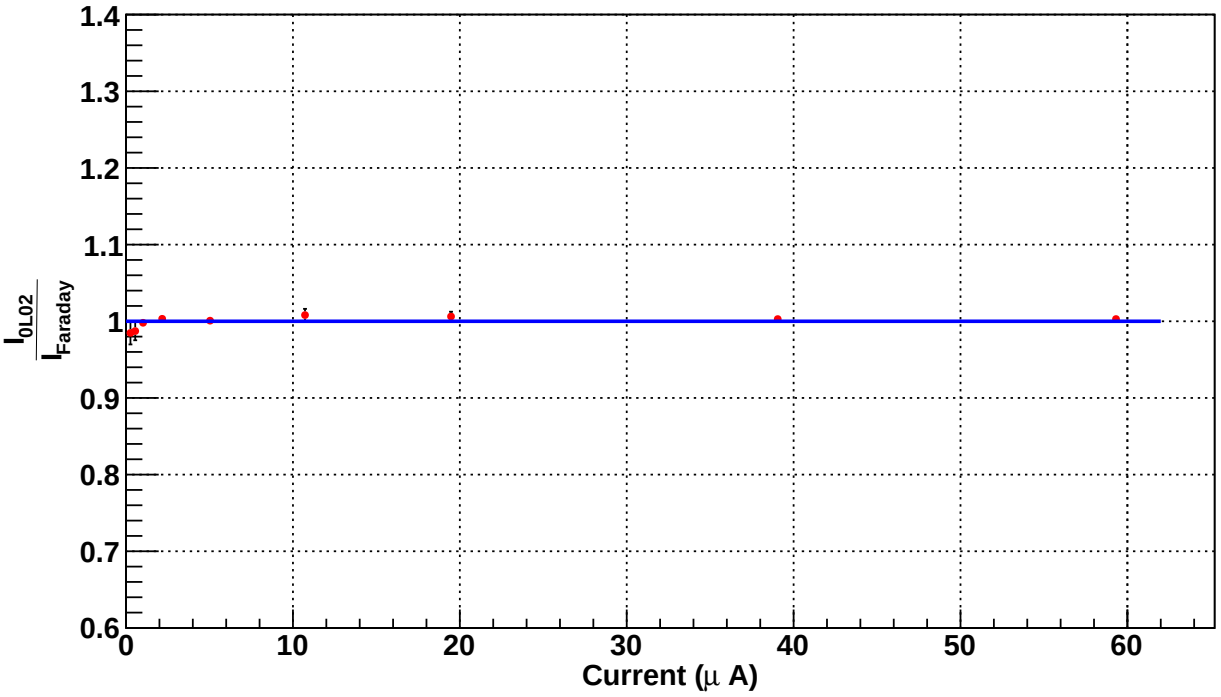

Figure 4.4: The ratio of I_{OLO2} to $I_{Faraday}$

were calibrated. There are three upstream amplifiers (U1, U3, U10) and three downstream amplifiers (D1, D3, D10) for different gain values. An amplifying constant and an offset were calculated for each amplifier. The offsets were extracted from the calibration runs. The calculation of the constants are shown in Equation 4.7:

$$C^n_{BCM} = \frac{\frac{Scaler^n_{BCM}}{T} - Offset^n_{BCM}}{I_{OLO2}}, \tag{4.7}$$

Table 4.2: Scaler Constants and offset values for the E05-110 experiment.

BCM Scaler	Scaler Constant	Offset
U1	2372.4 ± 2.4	362.5
U3	7294.5 ± 7.5	350.2
U10	22067 ± 225	442.6
D1	2427.9 ± 2.2	160.1
D3	7517.4 ± 8.7	126.7
D10	23485 ± 286	321.1

where n is the gain factor of the amplifiers (1, 3, 10) and T is the time of the run

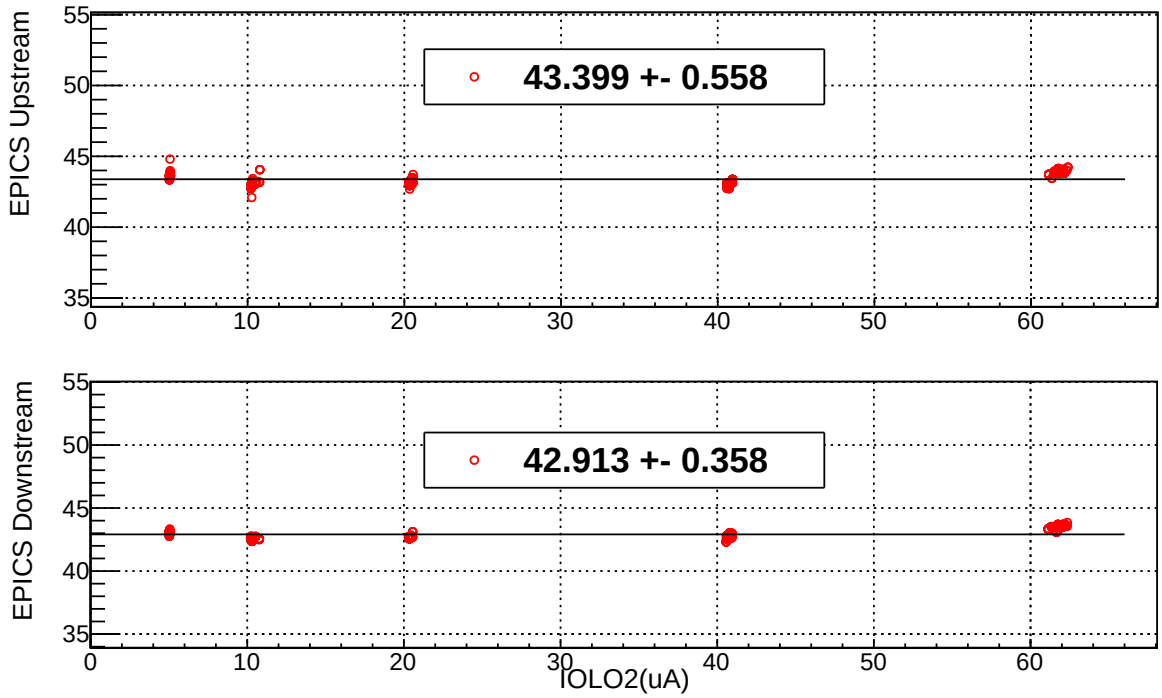

Figure 4.5: EPICS Calibration constants for different current settings.

which is counted by 1024 Hz clock. Figure 4.6 shows the BCM constants for different amplifiers *. While U1, U3, D1 and D3 are linear at 5-60 μA, U10 and D10 are linear only up to 30 μA. In this analysis, the U3 amplifier was used for the charge calculation, since the U3 amplifier signal was the most stable signal during the experiment.

The beam charge calculation is shown below in Equation 4.8:

$$Q(\mu C) = \frac{Scaler_{U3} - Offset_{U3} * T}{C_{U3}}, \tag{4.8}$$

where C_{U3} is the U3 scaler constant.

*This study was done by Xinhu Yan and the results were checked by the author.

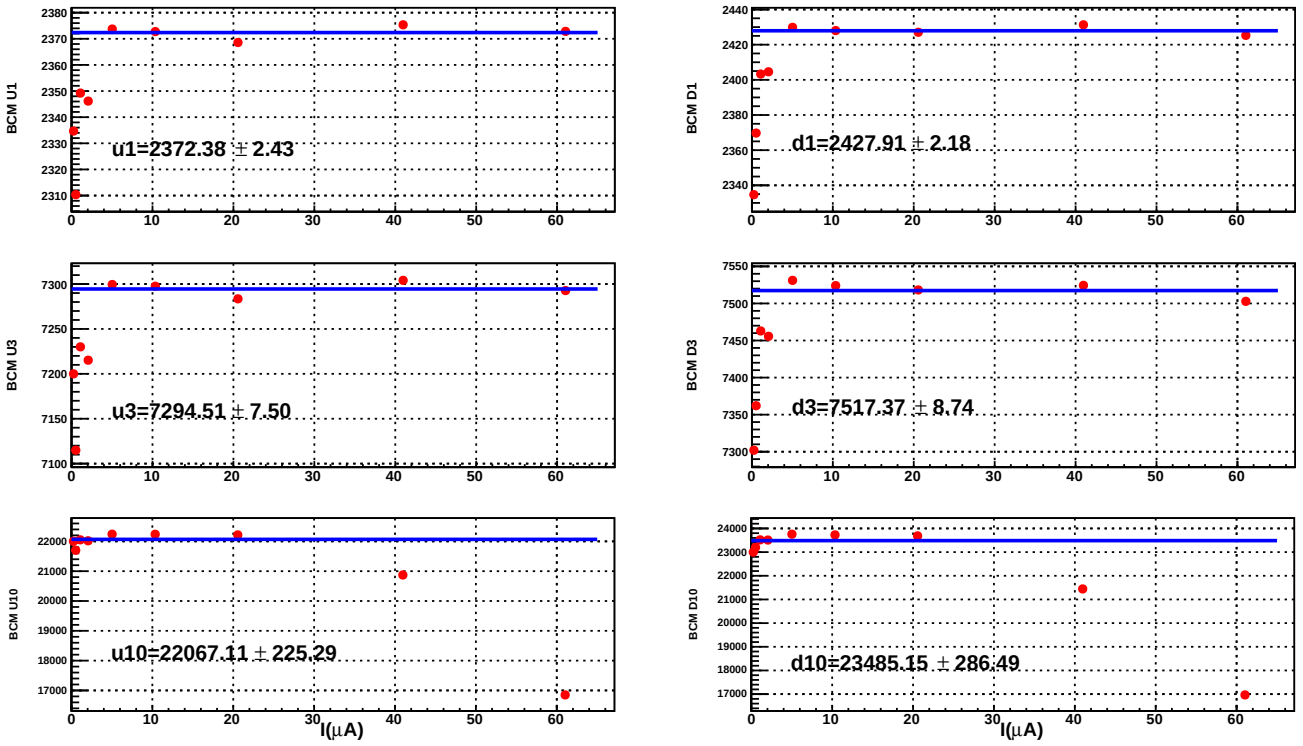

Figure 4.6: BCM scalers constants.

4.1.1.3 Live-time Calculation

- Computer Dead-Time: When an event generates a trigger, it is sent to the DAQ and then saved. However, sometimes some of the triggers are not saved due to high trigger rates. This is called *dead time*. 1-*dead time* is known as *live time*. The live time can be calculated by the ratio of the number of triggers stored to the number of triggers generated. When cross sections are extracted for a given run *live time* has to be calculated and corrected for. Scalers count for the number of triggers that were saved, and the total number of triggers generated can be found in the data stream. When triggers are generated, they are prescaled by the trigger supervisor. If a run has a prescale of N, the trigger supervisor will not count until they reach the Nth trigger. Therefore, when *live time* is calculated the prescale factor has to be counted for. Runs that have high trigger rates, have higher prescale factors. The E05-110 experiment has T1 as the main trigger for RHRS and T3 for LHRS. Thus T1(3)

triggers are used for *live time* calculation. The *live time* calculation is shown below:

$$t_{LT} = \frac{PS \times N_{T1(3)}}{Ntrigger_{total}} \tag{4.9}$$

where PS is the prescale factor, T1(3) is the number of triggers saved and $Ntrigger_{total}$ is the total number of triggers that were generated. Figure 4.7 and Figure 4.8 show the *live time* calculation for ^{56}Fe target at $\theta = 15^{\circ}$, $Ei = 1260MeV$ and $\theta = 120^{\circ}$, $Ei = 645MeV$. Overall, *live time* correction for the E05-110 experiment is less than 10%.

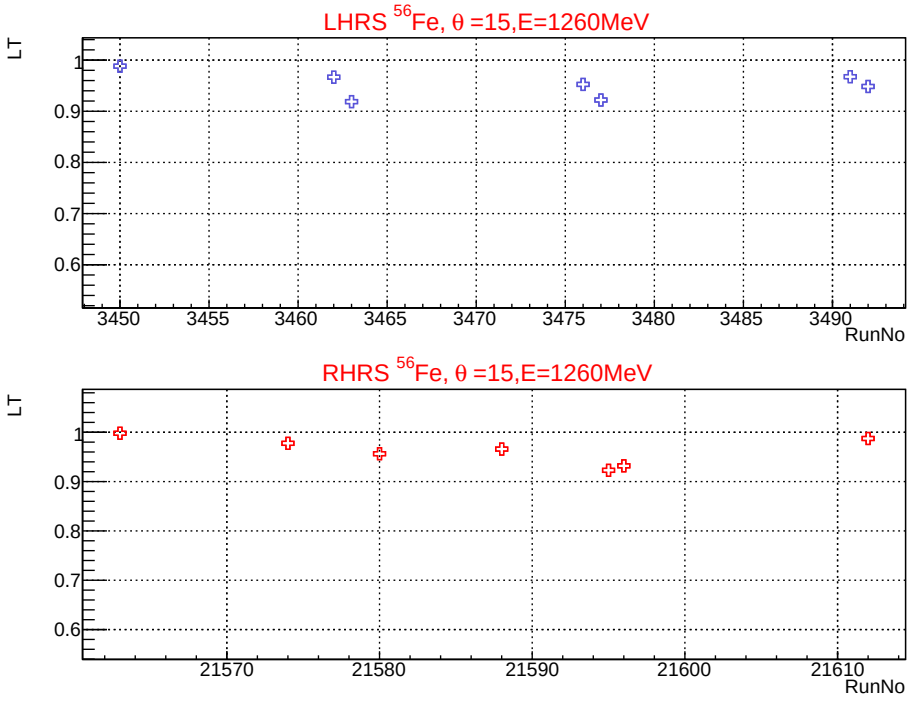

Figure 4.7: Live time calculation results for ^{56}Fe at $\theta = 15^{\circ}$ and Ei = 1260 MeV.

- Electronics Dead-Time: After particles generate signals at the detectors, these signals are sent to the TDC and ADC electronics. The TDC and ADC modules continuously receive signals. However, these modules can't process signals continuously. There is a very short time for these modules to process two consecutive signals. This is called

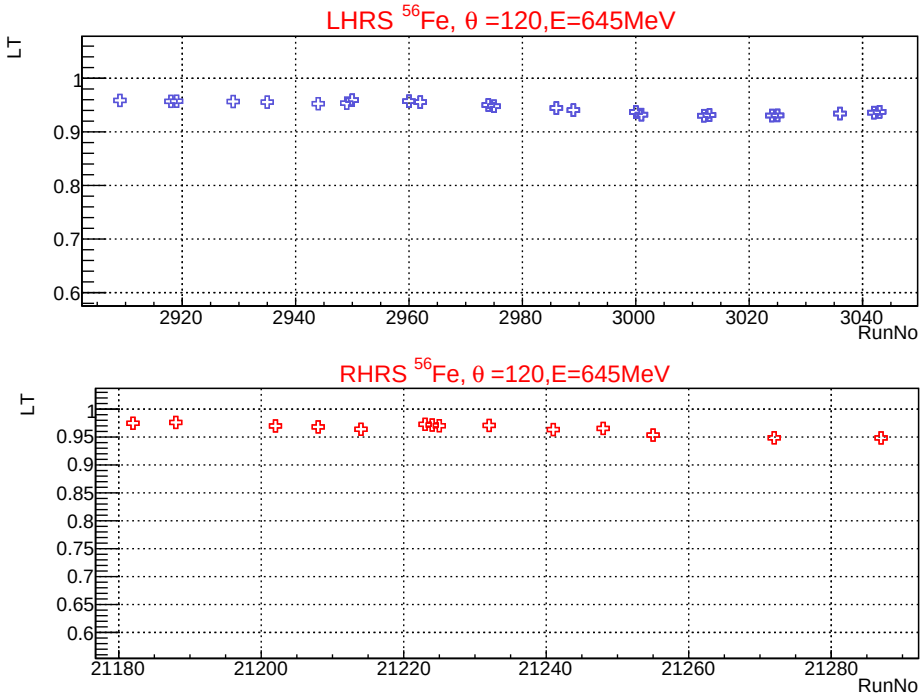

Figure 4.8: Live time calculation results for ^{56}Fe at $\theta = 120^{\circ}$ and Ei = 645 MeV.

electronics dead time. Electronics dead time can be calculated as shown below:

$$tDT_{electronics} = tgate \times Rtrigger \tag{4.10}$$

where tgate is the time for electronics to refresh and Rtrigger is the trigger rate. The tgate is about $\sim$ 100 ns for both RHRS and LHRS [79]. The electronics dead time is a very small correction, at most 2% for trigger rates $\sim$ 100 kHz. However, most of production runs have trigger rates around $\sim$ 10 kHz.

4.1.1.4 Detector Efficiencies

Detector efficiency ε is a product of all detector efficiencies. In this analysis we only use a Cherenkov cut, a trigger cut and a single track cut to select good electrons. Trigger efficiency was found to be higher than 99.99% which makes it negligible. Thus, the efficiencies in our cross section calculation only consist of the Cherenkov efficiency and the tracking efficiency.

- Cherenkov Efficiency: The Cherenkov detector is a particle identification (PID) detector and it is used to identify scattered electrons and background particles (pions). The ADC signal of the Cherenkov detector has two main peaks: the one-photoelectron peak and the main-photoelectron peak. the one-photoelectron peak is located around 250 ADC channels (see Figure 4.9). The main-photoelectron peak is located around 1400 ADC channels for LHRS and 1800 ADC channels for RHRS (see Figure 4.10).

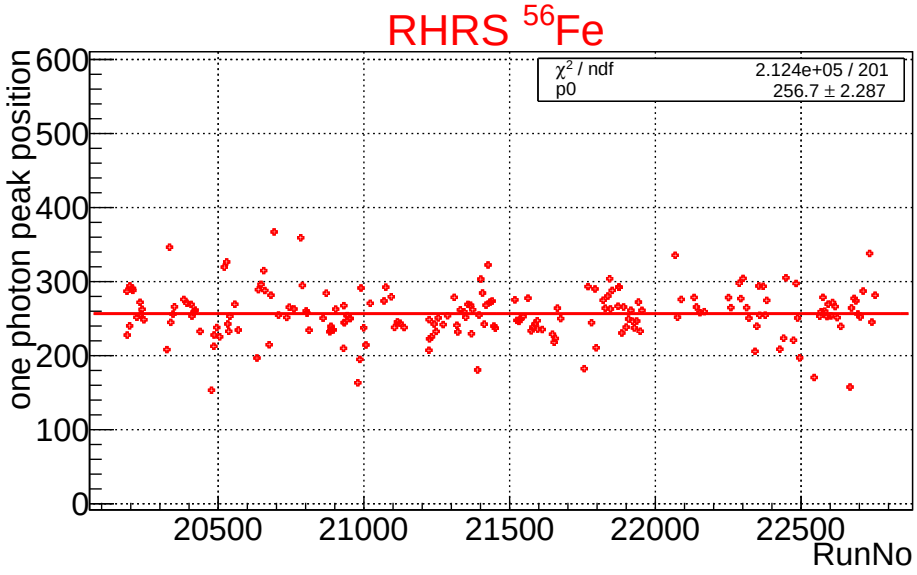

Figure 4.9: One-photoelectron peak position as a function of run rumbers.

A Cherenkov ADC cut at the 350 ADC channel ($R(L).cer.asum\_c > 350$) is used to select scattered electrons and reject background particles (pions and knock-on electrons). Pions have low energies and they usually don't fire the Cherenkov detector. However, knock-on electrons can fire the Cherenkov detector. Knock-on electrons are produced by pions that go through matter. Knock-on electrons are located at the one-photoelectron peak (200 ADC channel) on the Cherenkov ADC signal. Thus, cutting everything below the 350 ADC channel reduces the background mixed into the scattered electrons significantly. However, the 350 ADC channel cut can not clean the background 100%. The remaining background can be removed by fitting

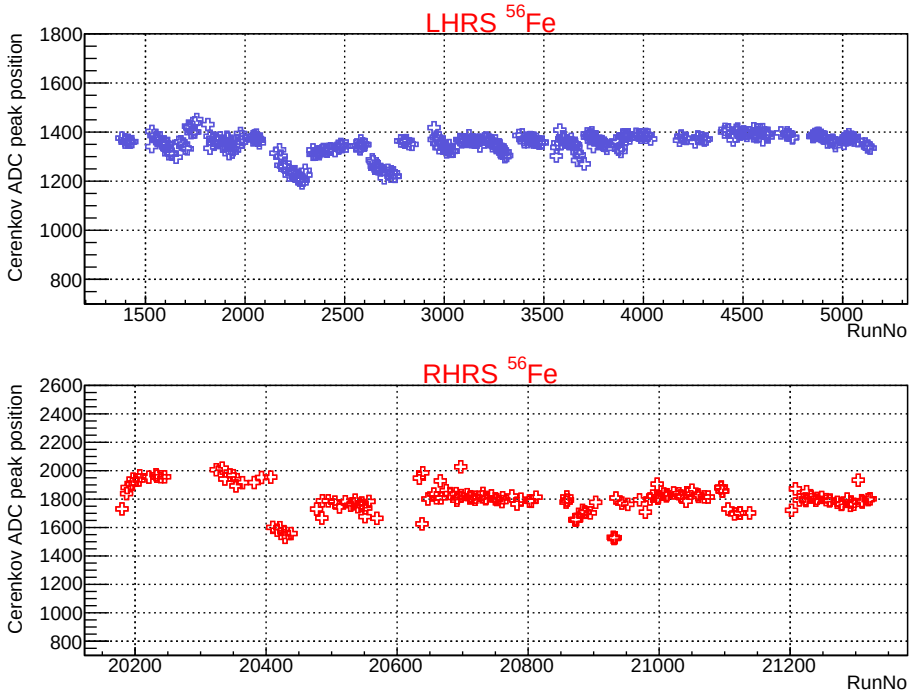

Figure 4.10: Main-photoelectron peak position as a function of run rumbers.

the one-photoelectron peak and the main-photoelectron peak separately to a Poisson distribution. The area under the tail of the Poisson distribution (one-photoelectron fit) that is above the 350 ADC channel was subtracted from the main-photoelectron fit to remove the remaining background.

When the one-photoelectron peak and the main peak were fitted, shower and preshower calorimeters were used to select clean samples of electrons and background. Once clean electrons and background samples were selected, they each fitted separately to a Poisson distribution. Then, parameters from fitting the clean sample were used to fit the main peak and the one-photoelectron peak.

The Cherenkov 350 ADC cut removes most of the background particles, but it also removes some of the good electrons (scattered electrons). The cut efficiency can be calculated by using the main-photoelectron Poisson fit to count for the removed electrons. The area under the tail of the fit that stays below the 350 ADC cut is the amount of the removed scattered electrons. Thus the cut efficiency can be defined as:

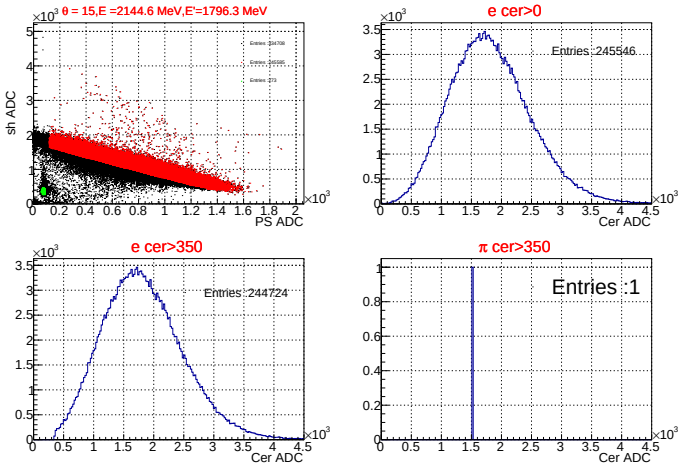

(a) Run no: 22089

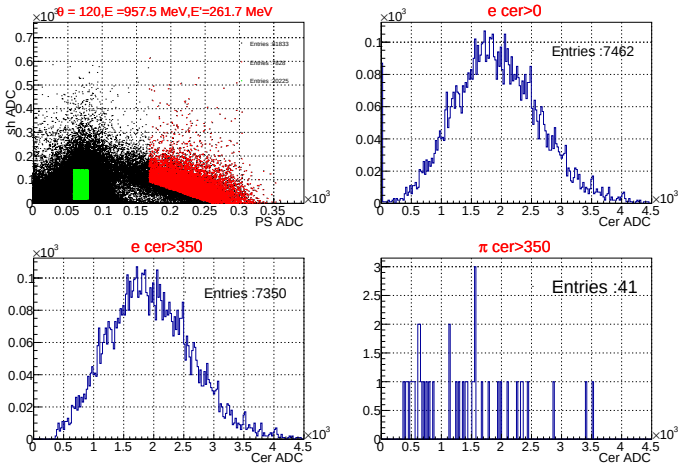

(b) Run no: 22495

Figure 4.11: Shower and preshower detectors were used to select electrons and background samples (Top run number: 22089 and bottom run number: 22495). The red area on the left top figure is the clean electron sample and the green area is the clean pion sample. The top right figure shows all the particles that fired the Cherenkov detector. The bottom left figure shows the events that survived after the Cherenkov 350 ADC cut. The bottom right figure shows the number of pions that passes the Cherenkov ADC 350 cut from the selected pion sample.

$$\varepsilon_{Cherenkov} = \frac{A1}{A1+A2} \tag{4.11}$$

where A1 is the area above the 350 cut and A3 is the area below the cut (see Figure 4.12). When this study was done, all of the other good electron cuts that are shown in Figure 4.2 were also used.

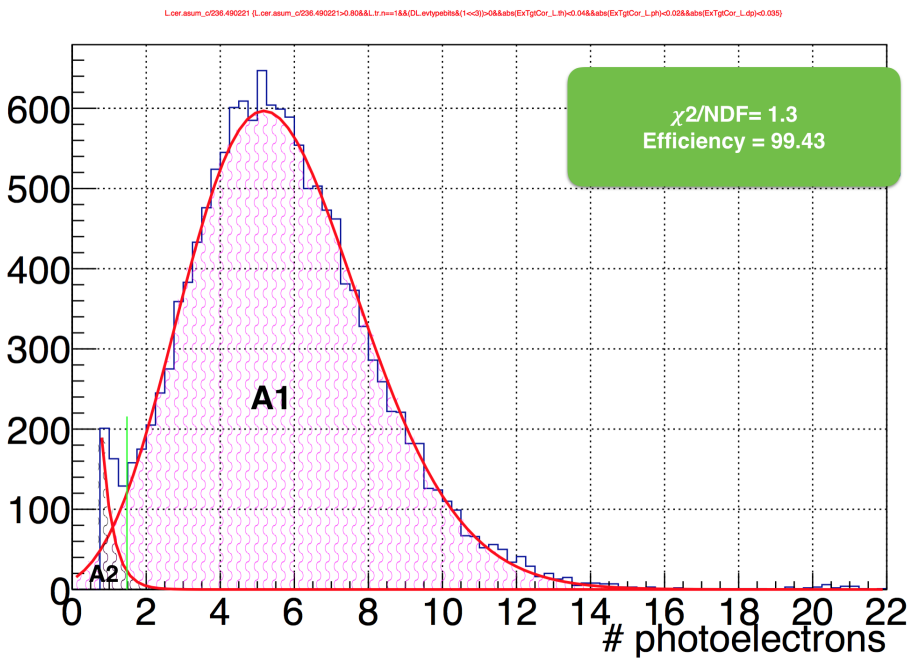

Figure 4.12: The Cherenkov ADC signal as a function of the number of photoelectrons for run 2305. The y axis is just the number of the counts. The green line is the position of the ADC 350 channel cut. A1 is the area above the cut and A2 is the area below the cut for the main-photoelectron fit

After the Cherenkov cut efficiency results were found for each run, they were fitted to a linear polynomial. The Cherenkov cut efficiency result for the LHRS was found to be 99.6 ± 0.0033 and for the RHRS was 99.9 ± 0.0029 (see Figure 4.13). Since the RHRS Cherenkov is longer than the LHRS Cherenkov, it is slightly more efficient than the LHRS one.

- Tracking Efficiency: The vertical drift chamber (VDC) provides the tracking information. Events can have zero track, one track or multi tracks. Events that have a single track are counted to be good events. The number of zero tracks and multi tracks are usually very small compared to one track events (see Figure 4.14 and Figure 4.15). A multi track event occurs when 2 or more tracks are found to be associated with the same event. When more than one particle goes through the detector within the gate opening interval of the TDC modules, a multi track event occurs. These particles can be good electrons or background particles. We select only one track events

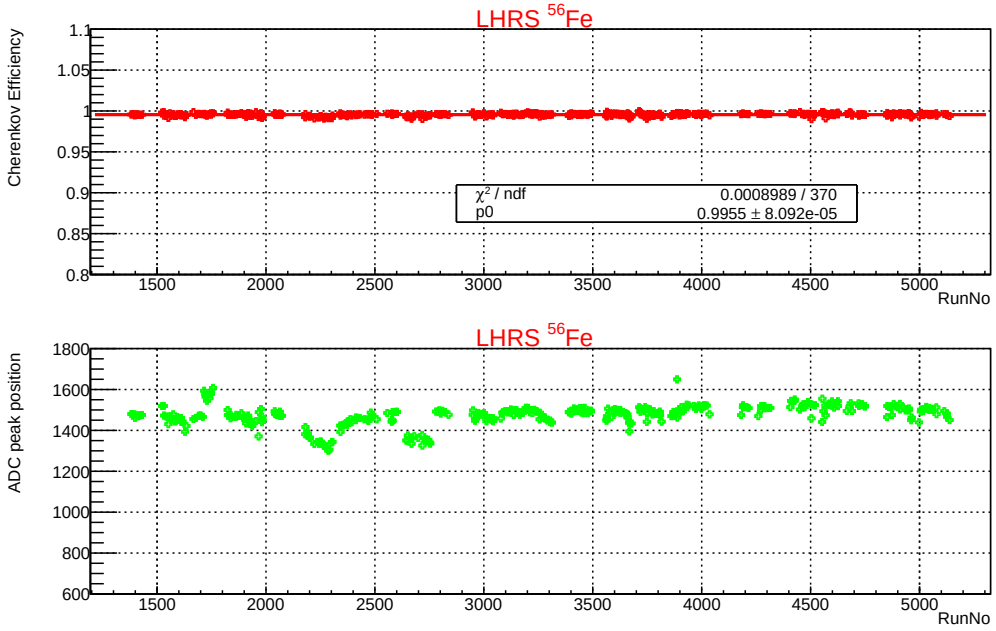

Figure 4.13: Cherenkov efficiency results for both RHRS and LHRS as function of run numbers.

via the $L.tr.n == 1$ cut when we extract cross sections. VDC single track efficiency is defined in Equation 4.12.

$$\varepsilon_{track} = \frac{N_{tr1}}{N_{tr1} + N_{trmgood}} \tag{4.12}$$

In Equation 4.12, N_{tr1} is the number of single tracks, $N_{trmgood}$ is the number of good multi tracks and . The PID and acceptance cuts were applied to each of these numbers to select good electrons. When $N_{trmgood}$ was calculated, the ADC signal of shower and preshower detectors for each track was used to identify any good tracks within multi tracks.

The result of the tracking efficiency was plotted as a function of the trigger rate and fitted to a first order polynomial. This fit was used to calculate the tracking efficiency for each run (see Figure 4.16).

The VDC wire efficiency is also a part of the tracking efficiency. However, the VDC at Hall A has wire efficiencies higher than 99.99%. Thus, it is insignificant for this

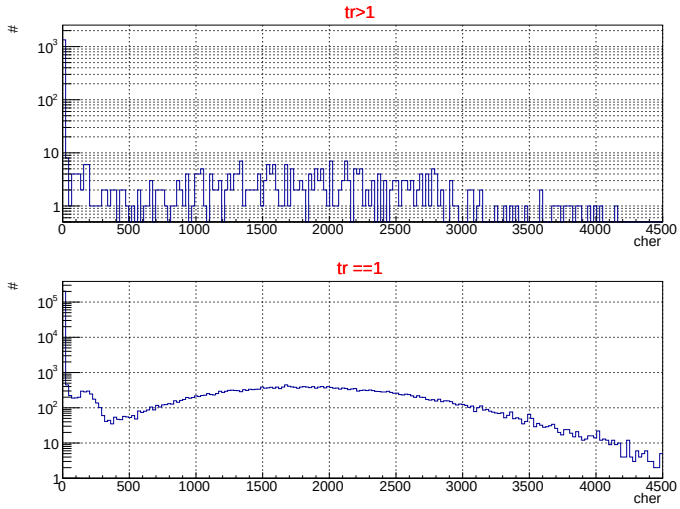

Figure 4.14: Cherenkov ADC signal of events with multi tracks and one track for run 22495.

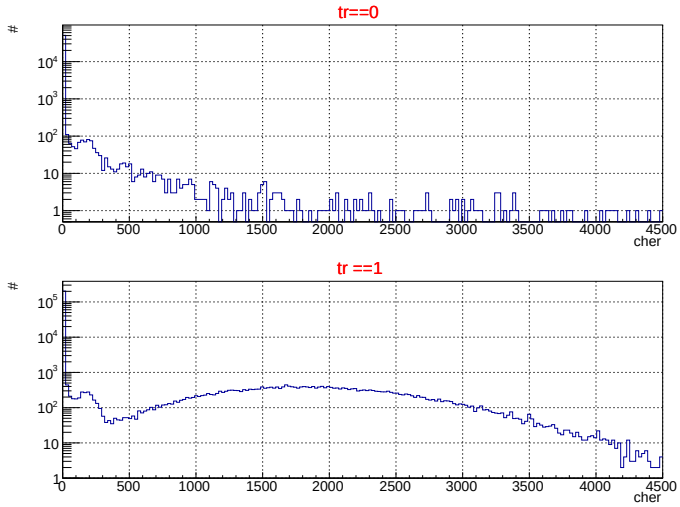

Figure 4.15: Cherenkov ADC signal of events with zero track and one track for run 22495.

analysis.

4.1.1.5 Acceptance Calculation

The acceptance of the HRS spectrometers is defined as a window in θ, ϕ and $\delta P/P$. The HRS spectrometers can only detect scattered particles within a certain range of θ, ϕ and $\Delta P/P$. The acceptance of the HRS for θ is ± 60 mrad, for ϕ is ± 30 mrad and for $\Delta P/P$ is $\pm 4.5\%$ (see Table 3.6).

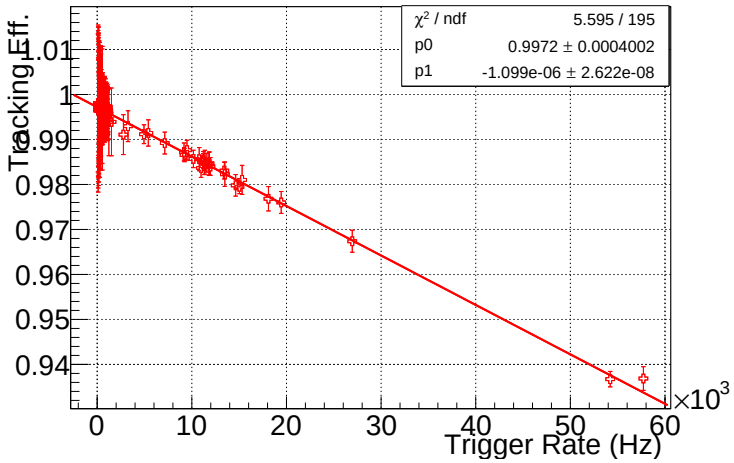

Figure 4.16: Tracking efficiency as a function of trigger rate.

The acceptance (A), which was used in the calculation of the cross sections, is not the size of the spectrometer window but rather the ratio of the number of particles detected within the window (cuts) to the total number of particles generated at the scattering vertex. The acceptance shows the number of the scattered particles that made it to the focal plane of detectors. In an ideal case, the acceptance would be 1 (all of the scattered particles would reach the focal plane), however, the complicated geometry of the magnets and the multiple scattering decreases the number of particles detected within the acceptance cuts. The acceptance cuts are given in Figure 4.2. The acceptance corrects for the particles that were excluded due to the acceptance cuts.

A monte carlo simulation code, called the Single Arm Monte Carlo (SAMC) [80], was used to study the acceptance (A). The SAMC was originally written in the Fortran programming language and translated into ROOT/C++ by Huan Yao [66]. A detailed description of the SAMC is given below:

- SAMC: θ, ϕ and $\delta P/P$ distributions are generated uniformly for each event (electron) at the target. Since each particle goes through the target, the target windows and other materials listed below in Table 4.3, the energy of each particle is corrected by the radiative effects due to the bremsstrahlung [81] and the ionization [82] and

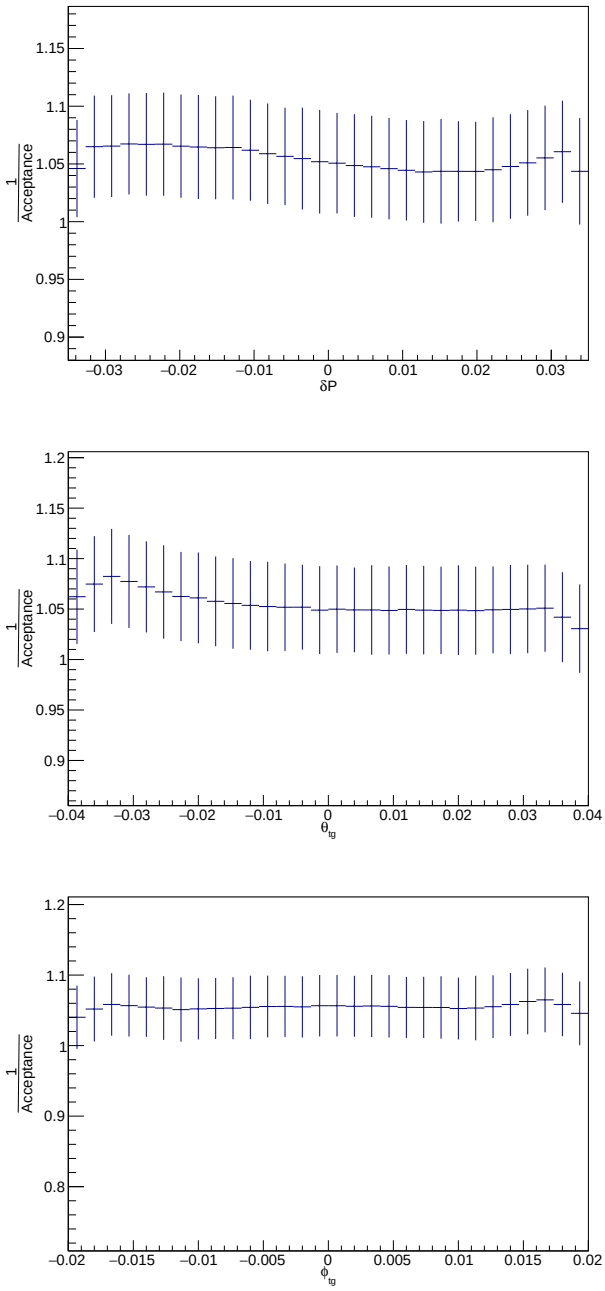

Figure 4.17: The acceptance is plotted as a function of $\delta P/P$, θ and ϕ at 90°.

the angle of each particle is corrected by the multiple scattering effect. The radiative effects change the energy of the incoming and the scattered electrons while the multiple scattering changes the scattering angle. The SAMC uses a forward optics matrix, which was generated by J.Lerose and is based on the SNAKE program, [83]

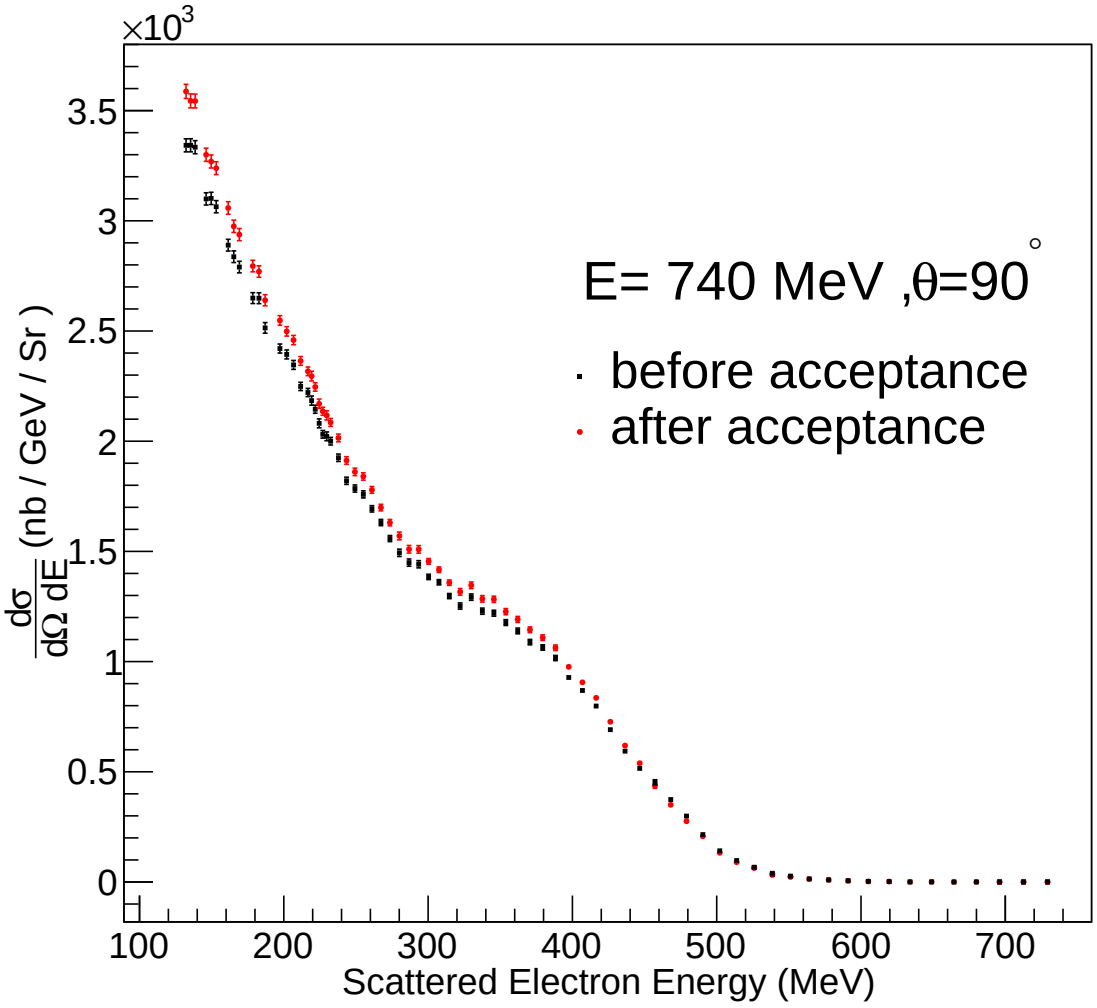

Figure 4.18: The figure shows the differential cross sections at $\theta = 90^{\circ}$ and $E = 740 MeV$ as a function of the scattered electron energy. The black points are before acceptance correction was applied and the red points are after.

to transport events through the magnets and get them to the focal plane. Events that reach the focal plane are called *Focal Plane Events*. After each event reaches the focal plane, they are reconstructed to the target with the CSR optics matrix which was also used for the CSR data reconstruction also.

The acceptance that was used in this analysis was a three dimensional acceptance. The projection of the acceptance on each dimenion is shown in Figure 4.17. The acceptance also includes bin migration due to the optics reconstruction.

Table 4.3: List of Materials that events go through in SAMC

Name	Z	A(g/mol)	Length(cm)	Density(g/cm^3)	Radiation Length X_0(g/cm^2)
Al	13	26.982	4.064e-02(Left Arm)	2.70	24.01
Al	13	26.982	3.048e-02(Right Arm)	2.70	24.01
Air	7	14.028	≈65	1.2e-03	36.66
Kapton	5	9.80	1.778e-02	1.42	40.61
Titanium	22	47.867	1.016e-02	4.54	16.16
Vacuum	0	0.00	357.0	0.00	0.00

4.1.1.6 Kriging Smoothing Function

After the acceptance correction was applied to the data, the cross sections still had some systematic fluctuations which could affect the Rosenbluth seperation. In order to smooth the spectra, the Kriging interpolation (the Gaussian regression) [84] method was used. The differential cross sections were first fitted by the Kriging interpolation method. Then the percent differences between data and fitting function were calculated and plotted as a function of $\Delta P/P$ for each run number. The percent differences were fitted by the Kriging interpolation method and the fit function was used to smooth cross sections. This procedure was repeated four times for each spectra. After repeating this correction four times, the systematic fluctuations in the percent difference were disappeared. The largest correction was found to be at 15°. Each step of corrections can be seen on Figure 4.19.

4.1.2 Extracting the Born Cross Sections

The Born cross sections are the final cross sections after all the corrections are applied to the raw cross sections. The Rosenbluth formula uses the Born cross sections. Since the goal of the E05-110 experiment is to extract R_L and R_T from the Rosenbluth formula, the Born cross sections have to be extracted first. This section will give the details of the corrections that were applied to extract the Born cross sections.

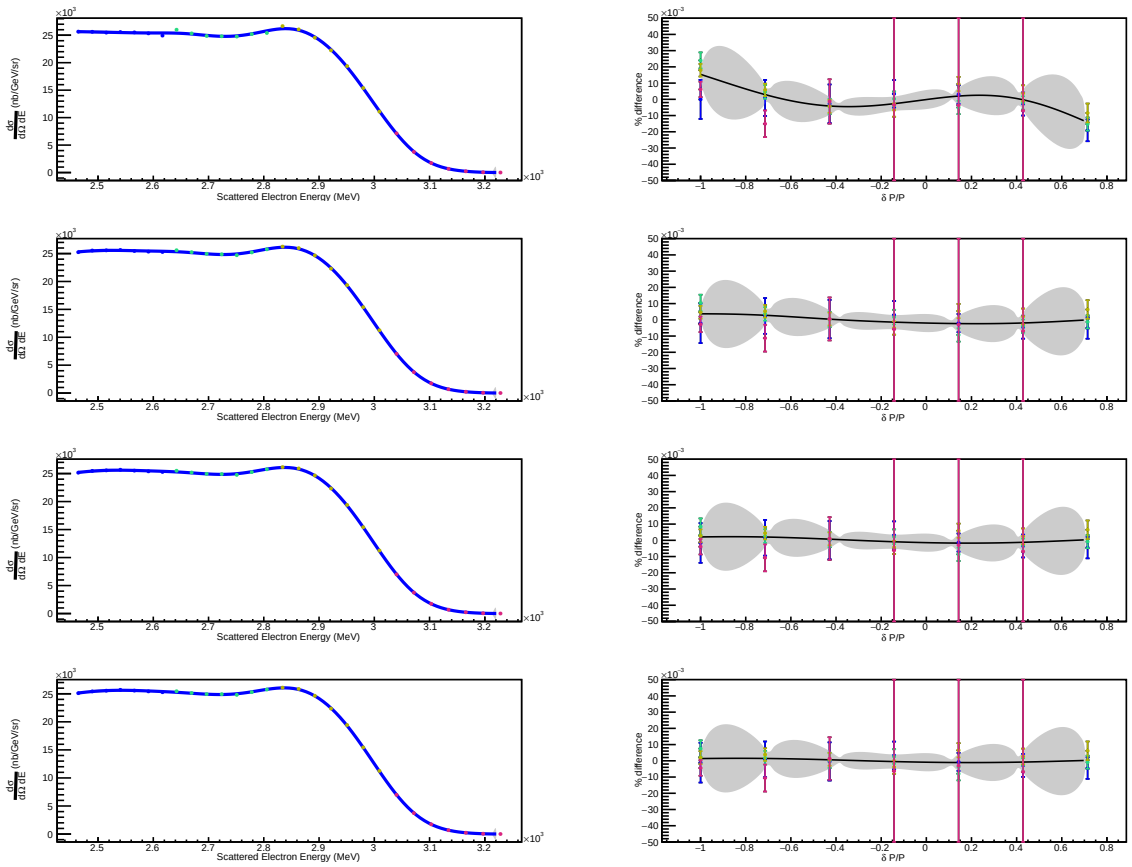

Figure 4.19: The left figures are the cross sections plotted as a function of the scattered electron energy at $\theta = 15^\circ$ and $E = 3250MeV$. On the right figures the percent differences between the data and the Kriging interpolation is plotted as a function of $\Delta P/P$.

4.1.2.1 Background Calculations

The main background for the E05-110 experiment comes from π^- which is generated during the scattering process and the electrons that were generated from the e^+e^- pair production. Since the cosmic background is less than 0.1%, it is negligible. The forward angle (15°) has the lowest background ratio contribution while the backward angle (120°) has the largest background ratio.

- Pion Background: The Cherenkov detector and the shower-preshower calorimeters were used to study π^- contamination in the electron sample (see Figure 4.11). The main reason the Cherenkov detector is used is to identify electrons and reject the pion background. A Cherenkov ADC cut which was applied to the 350 ADC channel,

cleaned most of the pion sample. However, this cut was not enough to clean all pions from the electron sample.

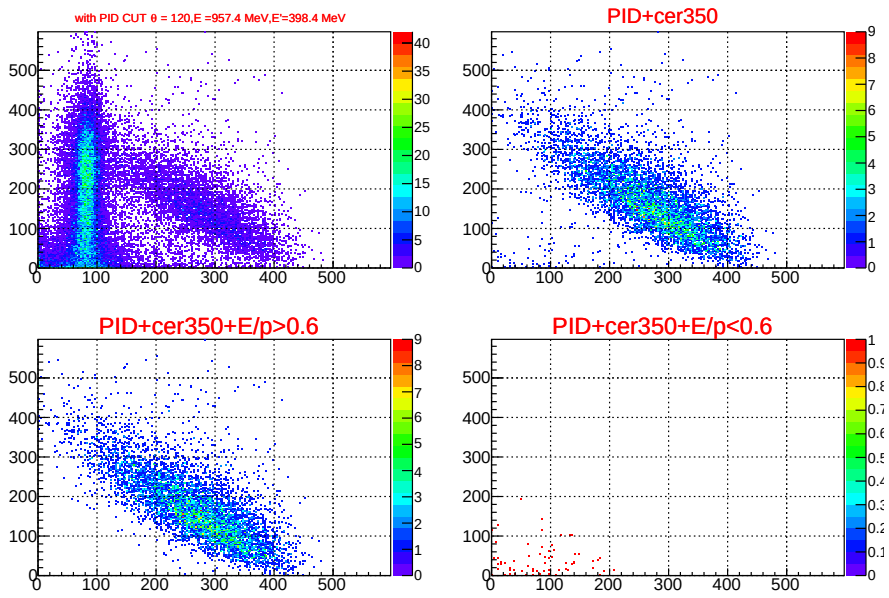

Figure 4.20: The top left figure shows the preshower ADC signal vs. the shower ADC signal for run 22440 with all the analysis cuts except the Cherenkov cut. The top right figure is the same as the top left figure but it has the Cherenkov 350 ADC cut on it. The bottom left figure has $\frac{E}{P} > 0.6$ cut and the bottom right figure has $\frac{E}{P} < 0.6$ cut in addition to the other cuts.

Pions have a shower and preshower ADC peak at low channels, and electrons have a peak at higher ADC channels. A sample of pions was selected from the main pion peak to study pion rejection. The number of pions that were leaked in the electron sample was checked by applying analysis cuts and an E/P calorimeter cut to the selected pions (see Figure 4.20). Pion rejection in this analysis is defined as:

$$\pi^{-}_{rej} = \frac{(N_{\pi^- sample} - N_{\pi^- leak})}{N_{\pi^- sample}} \tag{4.13}$$

where $N_{\pi^- sample}$ is the number of pions in the selected pion sample and $N_{\pi^- leak}$ is the number of π^- that passes through the analysis cuts. The backward angle and high beam energy runs have the most background. Thus, $\theta = 120^{circ}$ and $E = 957 MeV$ runs were used for the pion rejection calculation. The rejection factor was found to

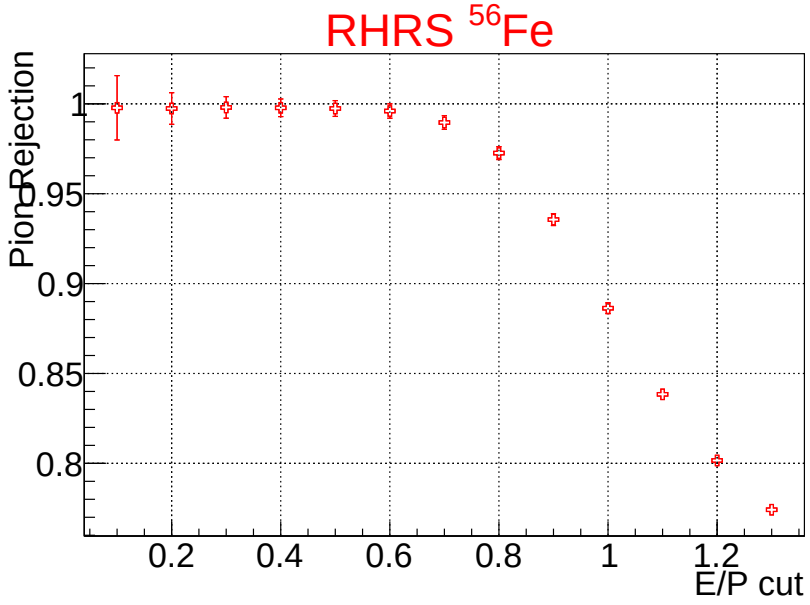

Figure 4.21: The pion rejection as a function of calorimeter $\frac{E}{P}$ cut.

be: $99.7 \pm 1.1\%$.

To find the pion background correction, the $\frac{N\pi^-}{N_{cut}}$ ratio was calculated for each angle and the beam energy. The Cherenkov 350 ADC cut is the main criteria for this calculation. All the analysis cuts were first applied to both of the samples and then everything above the Cherenkov 350 ADC cut was assumed to be electrons and everything below the cut was assumed to be pions. The pion background correction applied to the cross section as shown below:

$$N_{e^-} = N_{cut}[1 - (1 - \pi^-_{rej})\frac{N\pi^-}{N_{cut}}] \tag{4.14}$$

where N_{e^-} is the total number of electrons after the pion background is subtracted and N_{cut} is the number of events that passes the analysis cuts (see Equation 4.1).

The Pion background correction was found to be 2% for the biggest backward angle and highest beam energy ($\theta = 120^\circ$ and $E = 957MeV$). However, for $\theta = 15^\circ$, 60° and 90° this correction is less than 0.01% which is negligible.

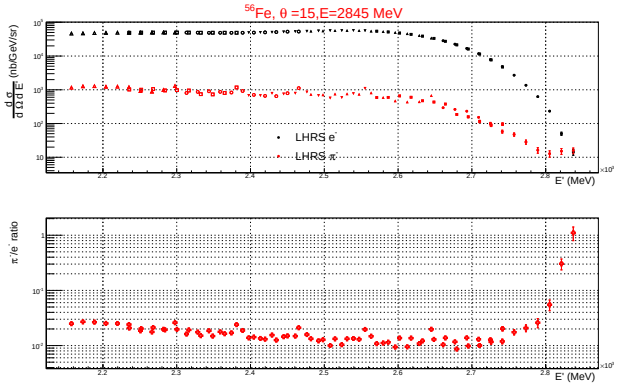

(a) $\theta = 15^{\circ}, E = 2845 MeV$

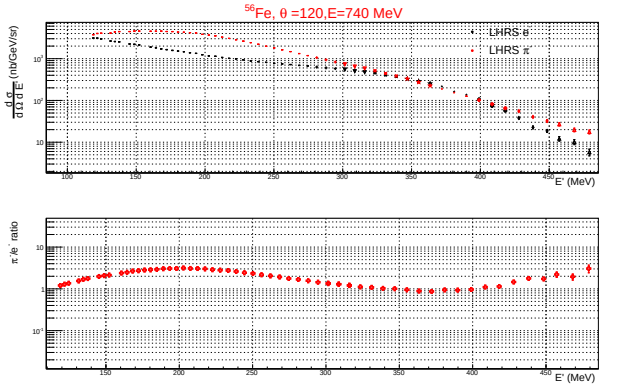

(b) $\theta = 120^{\circ}, E = 740 MeV$

Figure 4.22: In top figures electron cross sections are shown in black and pion cross sections are shown in red. The bottom figures show the ratio of cross sections.

- The e^- Background From the e^+e^- Pair Production: π^0 particles that are created at the target decay into 2 photons. This is the main decay mode of the π^0 with the branching ratio 98.823 [82]. These photons then decay into a e^+e^- pair and become a background for the experiment. This background needs to be evaluated and the cross sections need to be corrected for. During the experiment, the magnetic field of the magnets reversed for several beam energies at $\theta = 90^{\circ}$ and 120° to measure e^+ cross sections. Since the number of e^- particles produced from the pair production decay is equal to the number of e^+ particles, e^+ cross sections can be used as a correction factor. Unfortunately, due to time limitation the e^+ spectra couldn't be measured at all kinematics settings. Therefore, a Fortran code called EPC [85] and J.P Chen's calculation [4] have been used to evaluate e^+ spectra at unmeasured

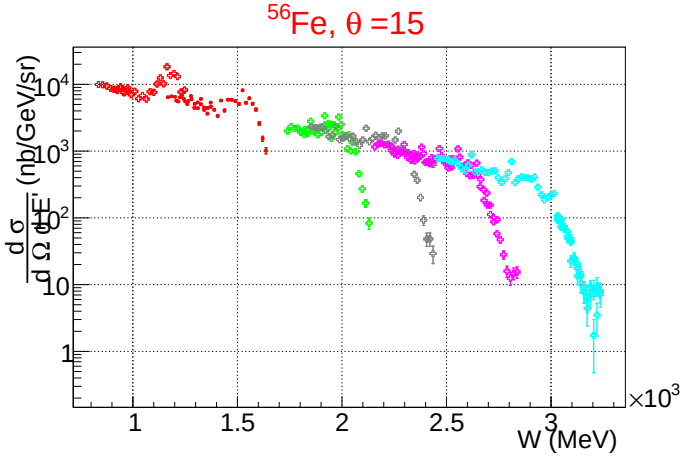

(a) $\theta = 15^\circ$

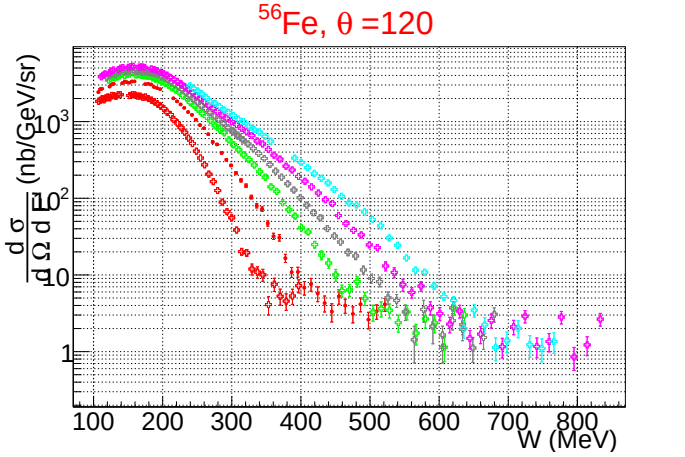

(b) $\theta = 120^\circ$

Figure 4.23: Pion cross sections as a function of energy loss of incoming electron ω for all 15 and 120 degree beam energies. Each color represents a different beam energy.

kinematics for $\theta = 90^\circ$ and 120°. Zein-Edinne Meziani's function was used for 60° [86].

EPC.f is the code that was used to produce the π^0 cross sections at the E05-110 experimental kinematics. These cross sections were used as an input for Chen's positron code to calculate positron cross sections. The measured positron data was analyzed to extract cross sections. The positron data was treated the same as the electron data. However, in addition to the regular analysis cuts, a β cut was used to clean the knocked out proton background. Positron cross sections for the measured spec-

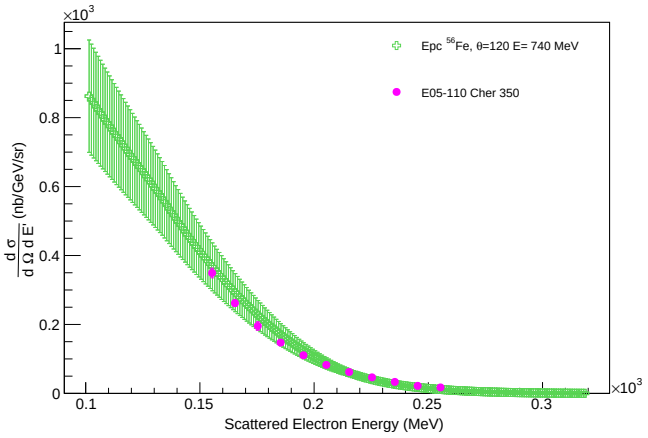

(a) $\theta = 120^{\circ}, E = 740 MeV$

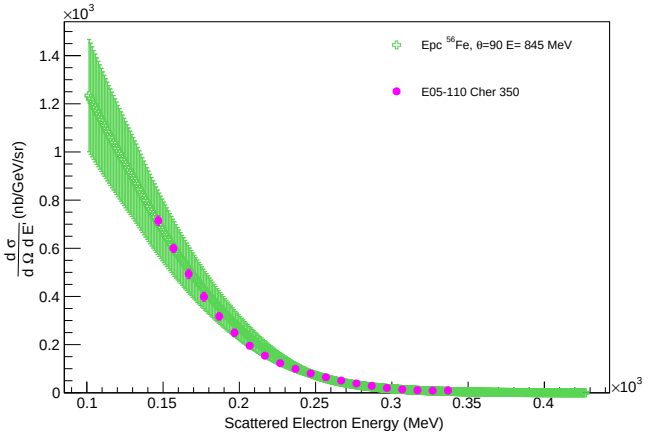

(b) $\theta = 90^{\circ}, E = 845 MeV$

Figure 4.24: The pink points are measured positron cross sections for E05-110 experiment. The green band is the positron cross sections that were extracted from EPC.f and Chen's [43] code.

tra compared to Chen's calculation. Chen's calculation was used for the SLAC NE9 experiment with different experimental conditions than our experiment (scattering angle, acceptance, target and target thickness, etc.). Therefore, a constant number that brings the experimental and Chen's cross sections to agreement was calculated from a fitting procedure. This constant number was then used to calculate cross sections at unmeasured e^+ spectra. One constant number was evaluated for each angle. These numbers are given in Table 4.4.

Table 4.4: Constants that were used to calculate positron cross sections.

Angle	Constant
120	673.3
90	521

Meziani's calculation was used only for $\theta = 60^\circ$ energies. His function is given below:

$$\sigma_{Meziani} = A1 + A2 * Ei + A3 * Ei^2 * (e^{-A4*Ep}) \tag{4.15}$$

where A1, A2, A3 and A4 are the parameters from Meziani's function, Ei is the beam energy, and Ep is the scattered electron energy.

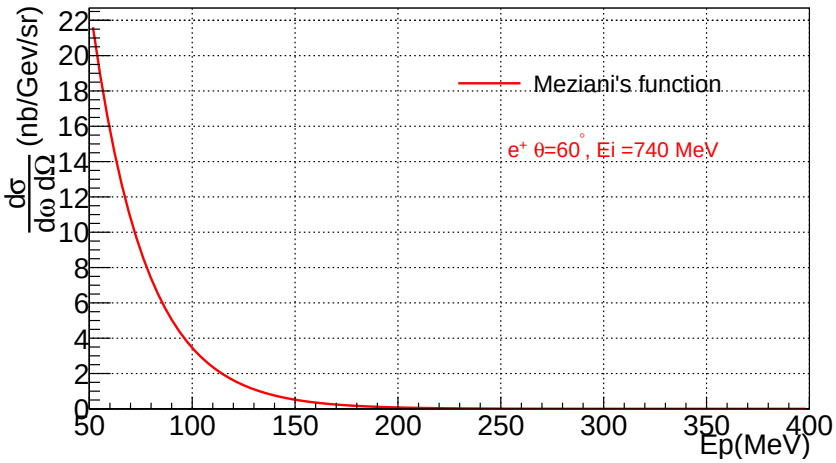

Figure 4.25: Positron cross sections that were calculated by using Meziani's function at $\theta = 60^\circ$ and Ei=740 MeV.

Table 4.5: Meziani's positron function parameters

A1	A2	A3	A4
241.8	-0.736	$0.835x10^{-3}$	0.038

The background from e^+e^- is almost zero at high scattered electron energies (Ep). It gets larger at low Ep. Another fortran code wiser.f was used to check the result of EPC.f. The difference between these two codes was used as an uncertainity. The systematic uncertainity is calculated to be 18%.

- Cosmic Background: Particles that shower on earth constantly from deep space are called cosmic background. They need to be measured for each experiment to make sure that they do not become a significant background. When the E05-110 experiment ran, special data were recorded with no target or beam energy to measure the cosmic background. The analysis of these cosmic runs showed that the cosmic background is negligible for our experiment. Figure 4.26 and Figure 4.27 show beta distribution of cosmic run 20034. As can be seen in the figures after all the analysis cuts were applied, only two counts survived. The Cherenkov and shower ADC signals of the same cosmic run are shown in Figure 4.28. Run 20034 was recorded for 18 minutes which is same length for a typical production run. A typical production run has thousands of good events. Since the cosmic background is very small compared to the good events, it can be neglected.

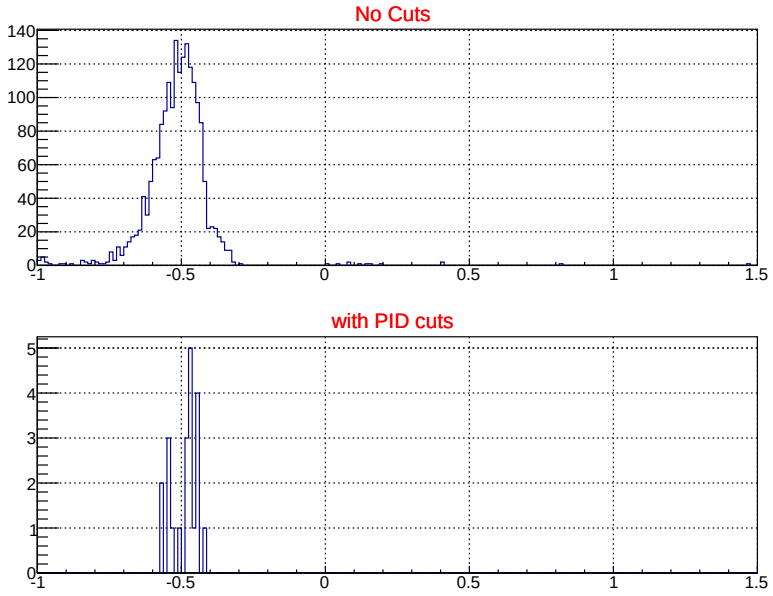

Figure 4.26: Beta spectrum of cosmic run 20034. Top figure is without any analysis cuts and the bottom figure is with all analysis cuts except Cherenkov cut.

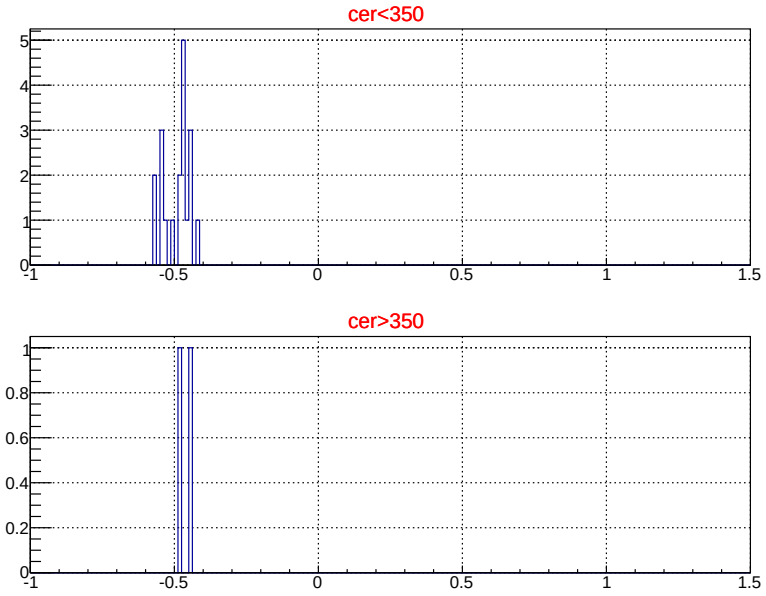

Figure 4.27: Beta spectrum of cosmic run 20034. Top figure is with all analysis cuts except Cherenkov cut and the bottom figure is with all cuts plus Cherenkov cut.

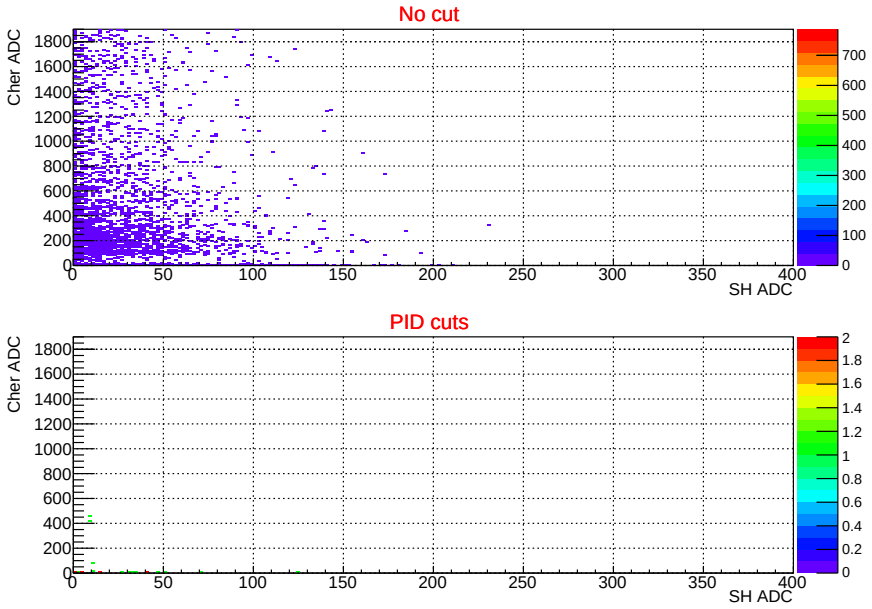

Figure 4.28: Y axis is Cherenkov ADC signal and X axis is shower ADC signal for cosmic run 20034. The top figure has no analysis cuts and the bottom figure is with all analysis cuts except Cherenkov cut.

4.1.2.2 Radiative Corrections

The Rosenbluth equation (Equation 1.10) is formulated within the first order Born approximation which assumes that a single virtual photon is exchanged between the incident electron and the target particle. However, higher order contributions in α due to the emissions of real and virtual photons from the ionization and the Bremsstrahlung in the target, need to also be considered to extract reliable Born cross sections. These corrections are known as the radiative corrections. The radiative corrections are explained in detail in Appendix A.

The Mo, Tsai and Stein [81, 87] equations were used to calculate radiative corrections. These equations used some approximations to integrate the bremsstrahlung function. These approximations were suggested to be less than 1% by Mo and Tsai [81]. The effect of these approximations on the final results was studied using a weighted monte carlo technic with the F1F209 cross section model [88]. The results were found to be less than 1%. The results are explained in Appendix A.

The Mo and Tsai equation requires the radiative corrections due to the elastic scattering, which are known as the radiative elastic tail, to be subtracted first. The elastic radiative tail subtraction procedure is also explained in detail in Appendix A. The subtraction of the radiative elastic tail and the positron background for 120° and $E = 740MeV$ is given in Figure 4.29.

After the elastic radiative tail was subtracted, the radiative corrections due to the inelastic scattering were calculated and corrected for. The inelastic radiative corrections for each scattering angle were calculated separately.

In electron scattering experiments, the incident energy of the electron is not measured right before the scattering vertex and the scattered energy is not measured right after the scattering vertex. The measured values of the incident and the scattered electron energies are different than the actual energy values at the scattering vertex. Therefore, interpolations and extrapolations are needed to calculate cross sections at the vertex energy values.

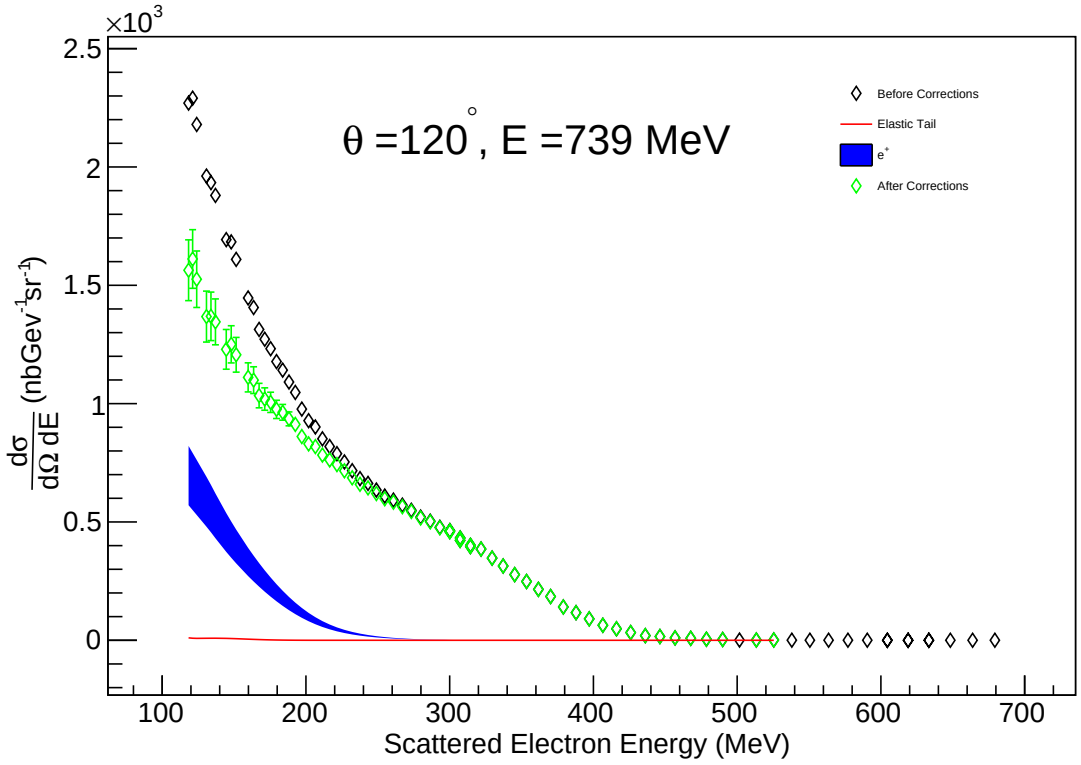

Figure 4.29: The differential cross sections are plotted as a function of the scattered electron energy. The black points are the raw cross sections. The blue band is the positron cross sections and the red line is the radiative elastic tail for $\theta = 120^\circ$ and $E = 740 MeV$. The green points are the raw cross sections after the positron cross sections and the elastic tail were subtracted.

In order to extract cross sections at the correct vertex energies, experiments measure data at many different beam energies for each angle. The E05-110 experiment measured data for 7 different beam energies at 15°, 60° and 90° each and 6 different beam energies at 120°. In addition to the measured data, the F1F209 [88] cross section model was used to generate one spectrum below the lowest measured beam energy spectrum for each angle. The F1F209 model is a fit for the existing inelastic data. The F1F209 spectrum was used to increase the accuracy of the interpolation for the lowest energy. Using the model cross sections below the lowest measured spectrum has less than 0.1% effect on the final cross section. The process of extracting radiatively corrected cross sections is called the unfolding procedure. The FORTRAN code RADCOR.F [89] was used to perform the unfolding procedure for the E05-110 experiment analysis.

The RADCOR.F uses two different scaling functions to perform interpolations. These functions are the quasi-elastic scaling variable y and the invariant mass W. The W interpolation was implemented into the RADCOR.F by the author of this thesis. The y scaling function is defined by [90, 91]:

$$\omega + M_A = (y^2 + 2y\overrightarrow{q} + M^2 + \overrightarrow{q}^2)^{1/2} + (y^2 + M_{A-1})^{1/2} \tag{4.16}$$

The y scaling function aligns the quasi-elastic peaks. Therefore, the y scaling was used up to the quasi-elastic peak. For the region after the peak, W was used. The W scaling aligns the delta peaks. Although the effect of using two different scaling functions is less than 1%, the generalized logistic function (Richard's curve) [92] was used to have a smooth transition between both scaling functions. The ω/E scaling was also used to check the other two functions. The results are shown below:

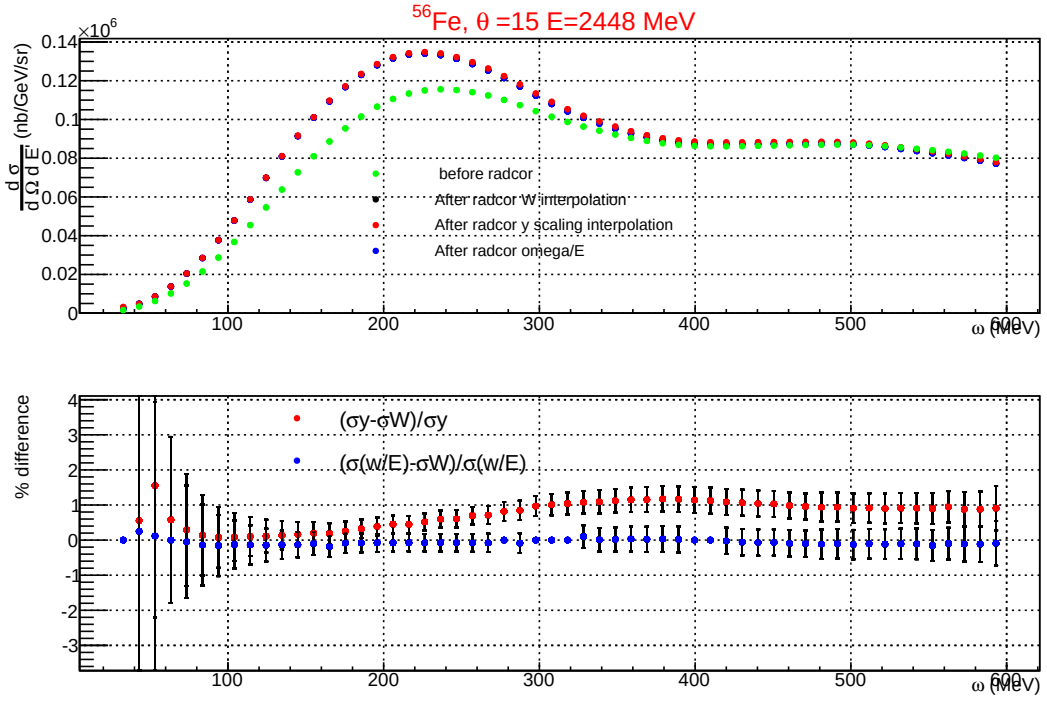

Figure 4.30: The radiative corrections with different scaling functions. The y axis is cross sections and the x axis is the energy loss ω (MeV). In top figure, the green points are the cross sections before radiative corrections, the black points after the radiative corrections with W scaling, red points with y scaling and blue points with ω/E scaling. The bottom figure shows the percent differences between $y - W$ and $\omega/E - W$

The largest radiative corrections for the E05-110 experiment are 20% at 15°. The uncertainty on cross sections due to the radiative corrections is 1%.

4.1.2.3 Elastic Cross Sections and Absolute Normalization

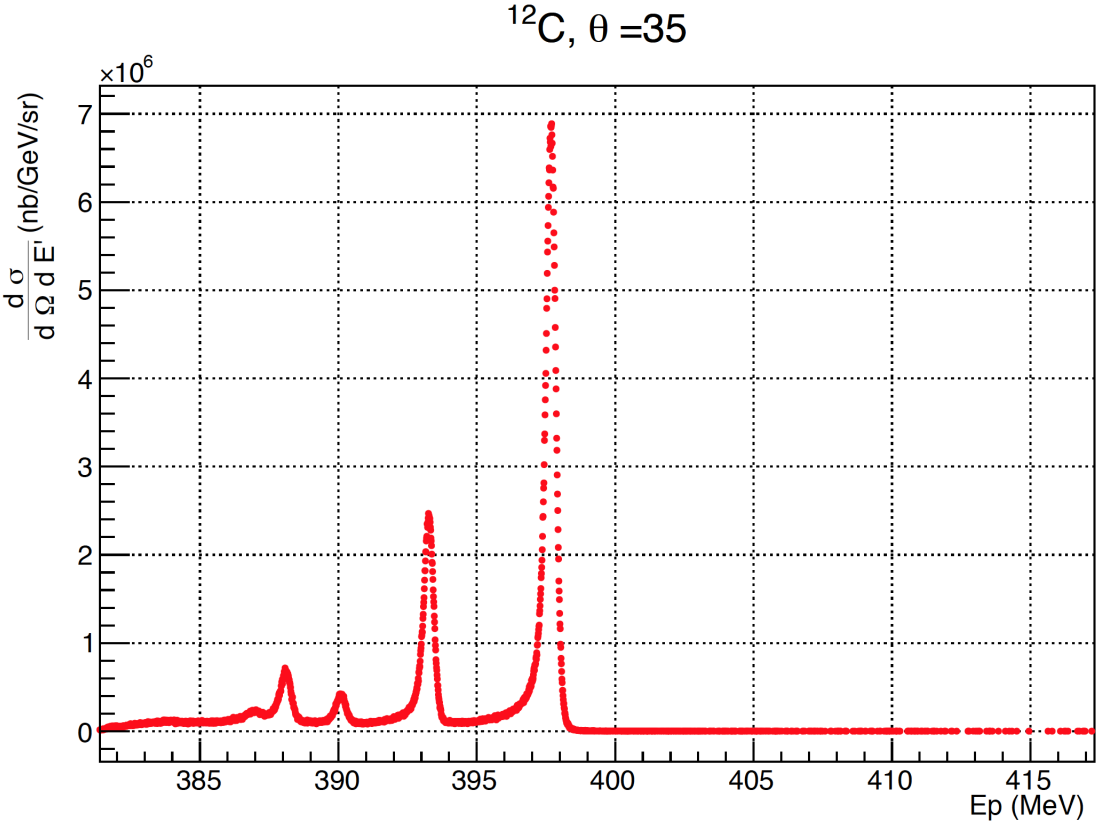

Figure 4.31: Cross sections for elastic and inelastic peaks at $\theta = 35°$ *and* $E = 400 MeV$ for ^{12}C.

Elastic scattering has been studied many times by different experiments. Therefore, the elastic form factors and the cross sections are well known. The E05-110 experiment ran elastic data on ^{12}C at some of the beam energies and angles where the quasi-elastic data were taken. The elastic cross sections and the form factors were extracted from the elastic runs. Comparing our elastic results to the world data can show us how accurate our quasi-elastic cross sections are. A difference in comparison with the world data will require the use of a normalization factor for quasi-elastic data which is equal to the difference. Since two different optics packages were used (low optics for scattered energies below 450 MeV

and high optics for scattered energies above and equal to 450 MeV), the elastic comparison can indicate the quality of optics packages.

The elastic cross sections were extracted by using Equation 4.1 with the same corrections that were used for quasi-elastic cross sections. The radiative corrections for the elastic scattering were calculated by using the Mo and Tsai formula [93] [94]. The elastic radiative corrections formula is given in Appendix A.

The elastic cross sections at a certain scattering angle represent the average cross section for $\theta \pm 20mrad$. Since the cross sections do not change linearly, a center of bin correction, which is called finite acceptance, was calculated. The Phaseshift.f program [95] was used to calculate the finite acceptance correction. The Phaseshift.f calculates cross sections and form factors by using world data for elastic scattering. The cross sections were calculated within $\theta \pm 20mrad$ for a step size of 0.001°. The finite acceptance was calculated by comparing the average cross section to the cross section at the central angle θ (see Figure 4.32).

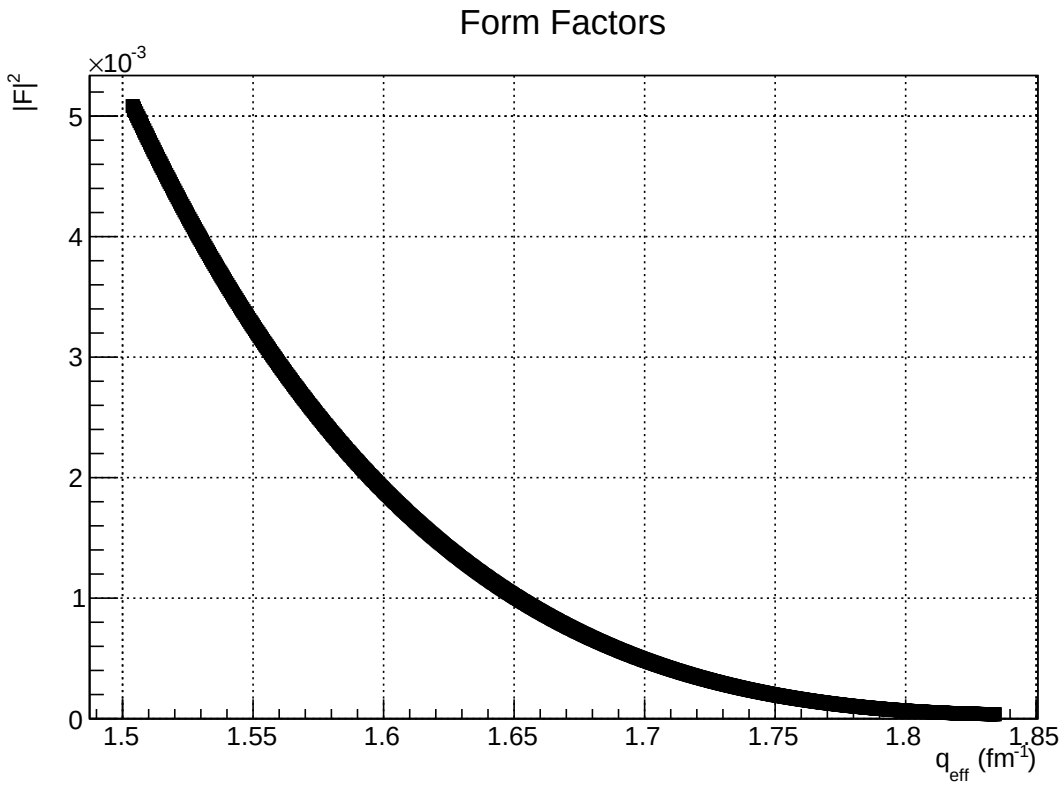

Figure 4.32: Form factors as a function of q^2.

After the cross sections were extracted, the elastic peak was integrated and the form factors were calculated.The results are plotted as a function of the q^2 and compared to the phase shift calculation and McCarthy and Reuter results (see Figure 4.33).

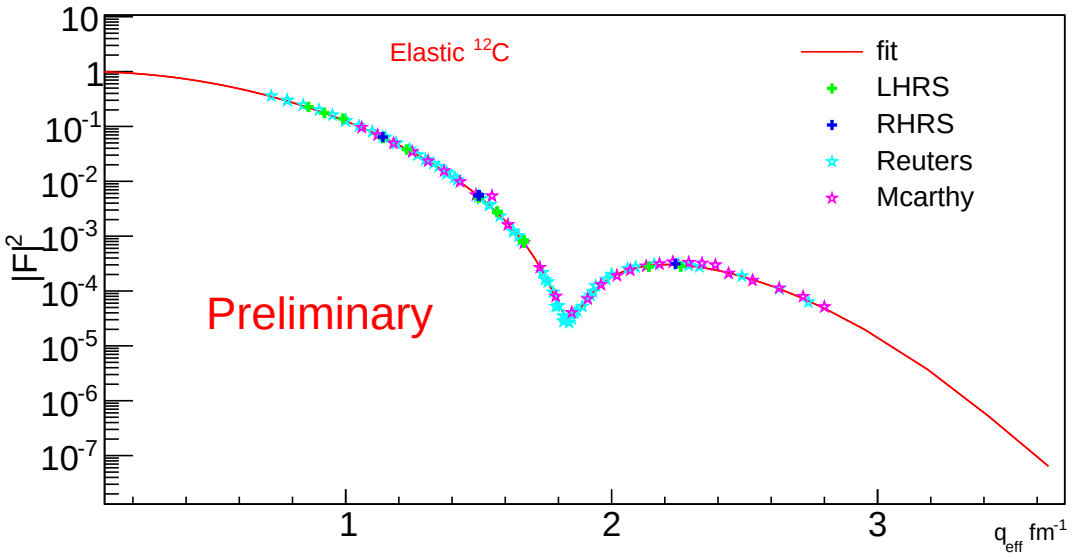

Figure 4.33: Elastic Form factors for the E05-110 experiment ^{12}C target as a function of q^2.

The elastic results have good overall agreement with the world data. The biggest difference found to be 9% at 45° and $E = 740$ MeV. The next largest difference from the world data is 6% at 38° and $E = 645$ MeV . The rest of the data have differences less than 3% from the world data. The comparison with world data does not indicate any systematic patterns for a particular energy or angle. Therefore, no absolute normalization was used in this analsis.

4.1.3 Systematic Errors

The uncertainties on the cross sections are:

- Detector Efficiencies: The uncertainity due to the detector efficiencies is less than 0.2%.

- Dead Time : The uncertainity due to the electronics and detector dead time is less than 0.2%.

- Target Thickness: The uncertainty due to the target thickness is less than 0.2%.

- Radiative Corrections: The uncertainty on the radiative corrections is less than 1%. The uncertainty on the radiative corrections comes from the approximations that were used in the calculation of correction. The F1F209 cross section model was used to test these approximations. The uncertainty due to the radiative corrections on the cross sections is less than 1%.

- Beam Energy, Scattered electron energy and the Scattering angle: The uncertainty due to the beam energy is less than 0.6% for 15° and less than 0.1% for the other angles. The uncertainty due to the scattered electron energy is less than 0.5% for 15° and less than 0.1% for the other angles. The uncertainty due to the scattering angle is less than 0.5% for 15° and less than 0.1% for the other angles. The F1F209 cross section model was used to calculate these uncertainties. Each quantity was generated according to a gaussian distribution . The σ of the gaussian is the uncertainty on each quantity. Then the F1F209 cross sections were calculated according to the gaussian distribution of each quantity. Finally, the cross section results were fitted to a new gaussian and the uncertainties were extracted from the parameters of the fit (see Figure 4.36, Figure 4.34 and Figure 4.35).

- Beam Charge: The uncertainty due to the beam charge is less than 0.3%.

- Acceptance: The uncertainty due to the acceptance is less than 1%.

- e^+e^- background: The uncertainty due to the e^+e^- background is less than 5% at 90° and 120° for low ω. This uncertainty is 0 at 15° and less than 0.1% at 60°.

- π^- background: The uncertainty due to the π^- background is less than 0.1% at 15° and less than 0.5% at other angles.

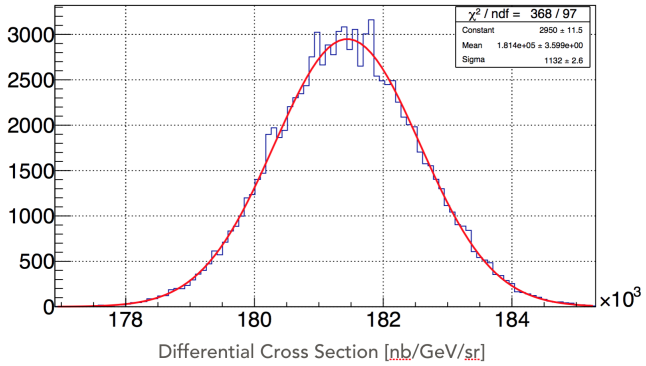

Figure 4.34: Calculation of the uncertainty on the cross sections due to the uncertainty on the beam energy.

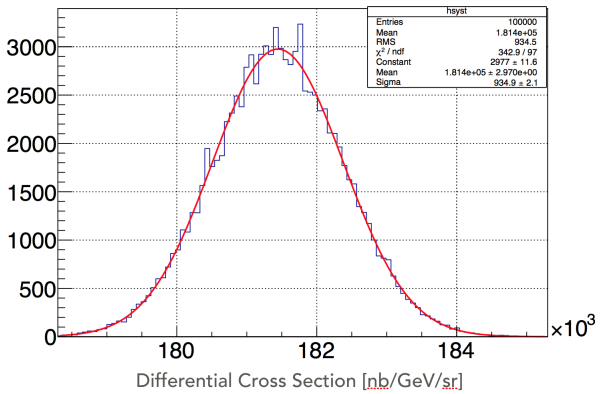

Figure 4.35: Calculation of the uncertainty on the cross sections due to the uncertainty on the scattered electron energy.

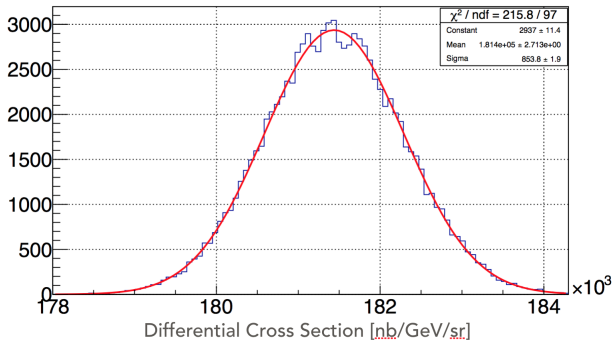

Figure 4.36: Calculation of the uncertainty on the cross sections due to the uncertainty on the scattering angle.

The systematic uncertainities in the cross section calculation are summerized in the Table 4.1.3. The total systematic uncertainity was calculated by the quadratic sum of each

uncertainity. The total systematic uncertainty at low ω region is 1.5% at 15°, 1.58% at 60°, and 1.57% at 90° and 120°. These uncertainties does not include uncertainties due to the e^-e^+ background. At very large ω region, the uncertainties at 90° and 120° are dominated by the uncertainties due to the e^-e^+ background. The total systematic uncertainty at very large ω region is 5.24% at 90° and 120° and same as the low ω region uncertainty for 15° and 60°.

Source	Uncertainity on $\frac{d\sigma}{d\Omega d\omega}$			
	15°	60°	90°	120°
Beam Energy (4×10^{-4})	<0.6	<0.1	<0.1	0.1
Scattered Electron Energy	<0.5	<0.1	<0.1	<0.1
Scattering Angle (0.2 mrad)	< 0.5	<0.1	<0.1	<0.1
Beam Charge	<0.3	<0.3	<0.3	<0.3
Dead Time	< 0.2	<0.2	<0.2	<0.2
Detector Efficiencies	<0.2	<0.2	<0.2	<0.2
e^+e^- Background	0	<0-0.1	<0-5	<0-5
π^- Background	<0.1	<0.5	<0.5	<0.5
Target Density	<0.2	<0.2	<0.2	<0.2
Radiative Corrections	<1	<1	<1	<1
Acceptance	<1	<1	<1	<1
Total without e^+e^- uncertainty	<1.75	1.58	1.57-5.24	1.57-5.24

Table 4.6: Summary of the systematic uncertainties on cross sections(in %)

4.2 Rosenbluth Separation

4.2.1 Rosenbluth Separation

The Rosenbluth [12] formula for the inclusive inelastic electron scattering is given in Equation 1.10. In this equation $\varepsilon = [1 + \frac{2\vec{q}^2}{Q^2} tan^2(\frac{\theta}{2})]^{-1}$ is the polarization of the virtual photon, R_L is the longitudinal response function and R_T is the transverse response function. The Rosenbluth separation method [96] can be used to extract R_L and R_T from Equation 1.10. The Rosenbluth seperation method uses the angle dependence of ε. Thus, measuring cross sections at two or more angles, Equation 1.10 can be solved for R_L and R_T. Equation 1.10 can be re-written as:

$$\begin{aligned} \varepsilon R &= \varepsilon \frac{\frac{d\sigma}{d\Omega}}{\sigma_{Mott}} \\ &= \varepsilon \frac{Q^2}{\vec{q}^4} R_L + \frac{Q^2}{2\vec{q}^2} R_T \end{aligned} \tag{4.17}$$

If εR is plotted versus ε for all available angles, it will give a straight line. If the points for all the available angles are fitted to a first order polynomial, the slope of the polynomial will be:

$$slope = \frac{Q^2}{\vec{q}^4} R_L \tag{4.18}$$

and the intercept will be:

$$intercept = \frac{Q^2}{2\vec{q}^2} R_T \tag{4.19}$$

The uncertainity on each point is very important and small alterations in the uncertainty will greatly change the result. This means the uncertanities should be handled with great care. The E05-110 experiment measured data at 4 different angles ($15^\circ, 60^\circ, 90^\circ$ and 120°).

The slope of these 4 points will give the R_L measurement (see Figure 4.37). The forward (15°) and backward (120°) angles have the biggest impact on the slope.

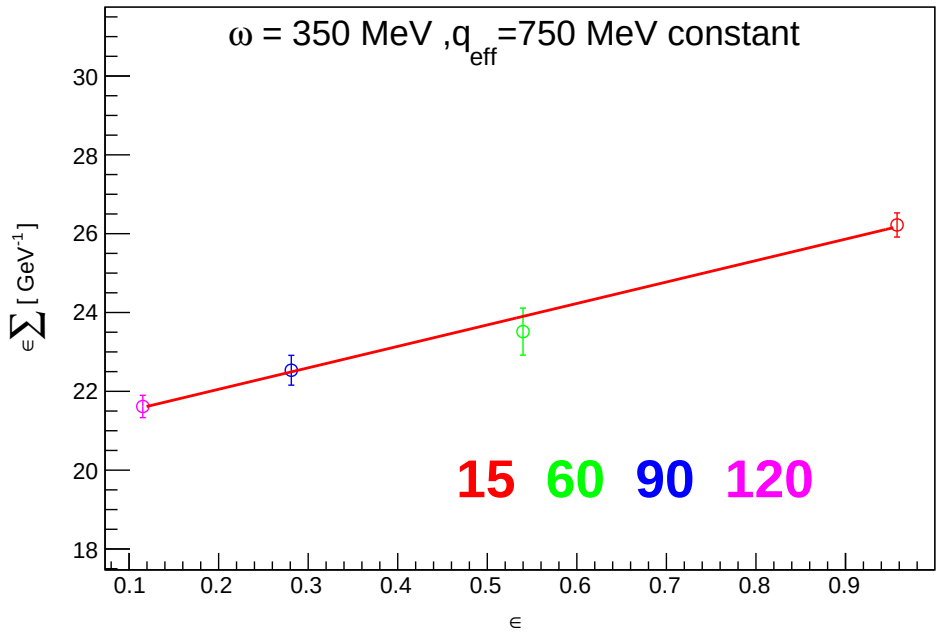

Figure 4.37: Rosenbluth separation at constant $q = 750MeV$ and $\omega = 350MeV$. Y axis is εR and x axis is ε . Each point represents a different angle.

4.2.2 Coulomb Correction

The quasi-elastic inclusive scattering of electrons from a nuclei is formulated by using the plane-wave Born approximation (PWBA) in Equation 1.10. The PWBA assumes that only a virtual photon is exchanged between the target and the electrons and both incoming and scattered electrons are described by plane waves. In the PWBA, the interaction between electrons and the charge of the nucleus is not included. Altough this approximation is valid for light nuclei, it can not be applied to heavy nuclei because of the sizeable nuclear charge [97]. The effective momentum aproximation can be used to include the Coulomb correction due to the nuclear Coulomb field in the PWBA. The effective momentum aproximation requires to a change to the energy of incoming and outgoing electrons by the nuclear

Coulomb potential (V_C) (see Equation 4.20).

$$E_{seff} = E_s - V_C, \tag{4.20a}$$

$$E_{peff} = E_p - V_C \tag{4.20b}$$

Therefore, Q^2 needs to be replaced by $Q^2_{eff} = 4E_{seff}E_{peff}Sin^2(\theta/2)$ and q^2 needs to be replaced by q^2_{eff}. Since E_s and E_p change by an equal amount, ω remains unchanged. The expression for the effective momentum transfer is given below:

$$q_{eff} = q\left(1 - \frac{V_C}{E_s}\right) \tag{4.21}$$

The value of V_C for ^{56}Fe was calculated by P.GUEYE et.al [97] and given below:

$$V_C = -8.9 \pm 0.7 MeV \tag{4.22}$$

4.2.3 Interpolation

The Rosenbluth method is defined at constant q_{eff}. Therefore R_L and R_T have to be extracted along a constant q_{eff} value. Unfortunately, the experimental data can not be measured for a constant q_{eff} value due to the time constraints at the experimental facilities. Instead of measuring the data at constant q_{eff}, it is measured for many constant beam energies at each angle. An interpolation procedure needs to be used in order to separate R_L and R_T at a constant q_{eff}. The interpolation at a specific q_{eff} and ω is done by a constant scaling variable. These scaling variables are W and y scaling. The y scaling variable changes from a negative value to positive value and $y = 0$ corresponds to the location of the quasi-elastic peak. As a result, when the cross sections are plotted as a function of the y scaling, the quasi-elastic peaks are aligned. Thus, the constant y scaling path can be used for interpolation up to the quasi elastic peak. After the quasi-elastic peak invariant mass

W is used. W aligns the delta peaks. The y scaling is defined in Equation 4.16 and W is defined in Equation 1.13.

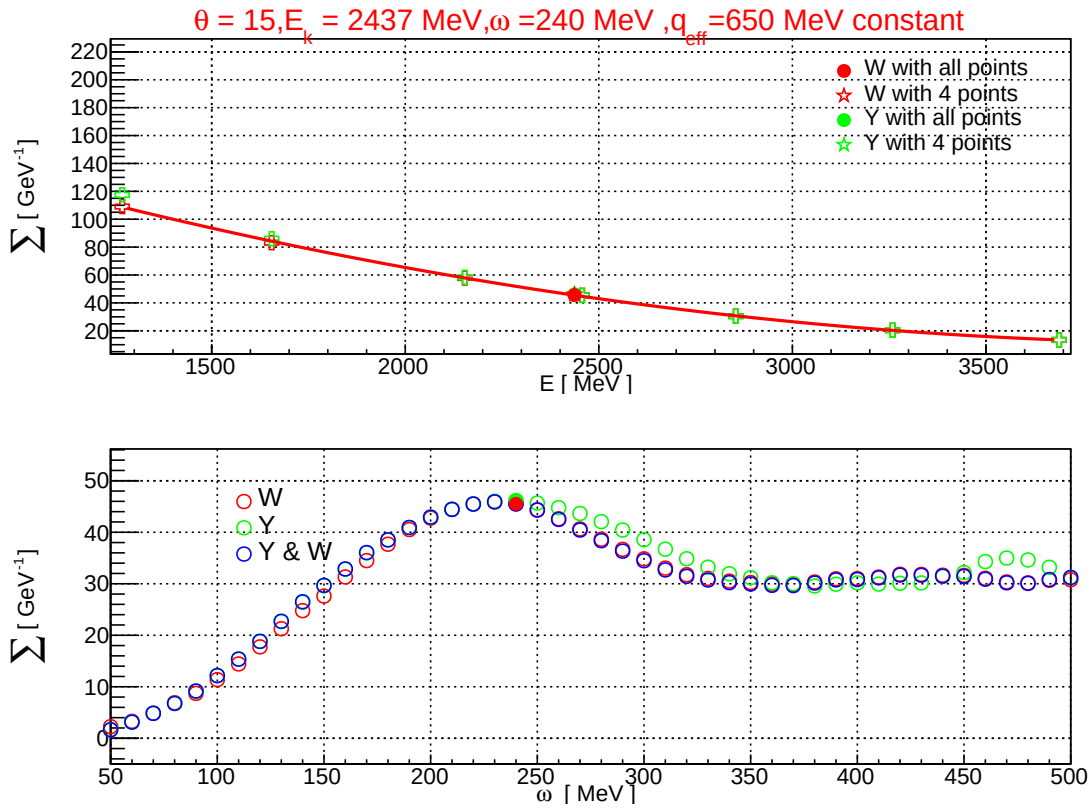

Figure 4.38: Interpolation along constant y and W scaling variables at constant $q = 650MeV$ at 15°. The top figure shows the interpolation with 4 points and all available points at $\omega = 240MeV$. Each point is coming from a different beam energy. The filled circles and stars are the interpolation results. The red color is for W interpolation and green is for y scaling interpolation. The y axis of the top figure is the total response function and the x axis is the beam energy. The bottom figure shows the interpolation at $q = 650MeV$ for whole range of ω with just W (red), just y (green) and W and y together (blue). Blue points use y scaling up to the quasi-elastic peak and after the peak W interpolation was used. The x axis of the bottom figure is ω and the y axis is the total response function.

4.2.4 The Coulomb Sum

$$S_L(\vec{q}) = \frac{1}{Z}\int_{0+}^{\infty} \frac{R_L(\vec{q},\omega)}{\tilde{G}_E^2} d\omega \tag{4.23}$$

The Coulomb sum rule is defined in chapter 2. As seen above, the Coulomb sum is the integral of R_L over the energy loss ω . The upper limit of the integral goes to infinity, however, in an experiment ω can be measured only up to $|\overrightarrow{q}|$. Moreover, reliable experimental data can not be obtained, near the $\omega \sim |\overrightarrow{q}|$ region due to the falling detector efficiencies, radiative corrections and other technical issues [35]. Therefore, the Coulomb sum in the large ω needs to be calculated carefully.

The denominator of the equation includes the nucleon form factors. In this analysis J. Arrington's [98] parametrization was used for the free proton form factor, and Galster's [99] parametrization was used for the neutron electric form factor.

- Proton Form Factor:

$$G_E^p(Q^2) = C(1+Q^2/0.71)^2 \tag{4.24}$$

  where C is the correction to the proton form factor [98].

- Neutron Form Factor:

$$G_E^n(Q^2) = -\mu_n \frac{\tau}{1+5.6\tau} G_E^p(Q^2) \tag{4.25}$$

In order to calculate the Coulomb sum at a constant $|\overrightarrow{q}|$, R_L needs to be extracted for all available angles first. After R_L is obtained, the R_L spectrum can be integrated and the Coulomb sum can be extracted.

CHAPTER 5

RESULTS

The differential raw cross sections and the Born cross sections on the ^{56}Fe target were extracted for the LHRS and RHRS. At 15°, the quasi-elastic peak is the dominant feature of the cross sections at incident energies from 1260 MeV to 2850 MeV. At 3250 MeV incident energy, the quasi-elastic peak starts to become more broad and it eventually disappears at 3680 MeV. At 60°, the quasi elastic peak is dominant at incident energies from 645 MeV to 958 MeV and it starts to disappear at higher energies. At 90° and 120°, the quasi-elastic peak is visible at incident energies from 400 MeV to 645 MeV and it disapepears at higher energies. At the same incident electron energy, the cross sections are largest at the smallest angle and they get smaller as the angle increases. At the same scattering angle, the lowest incident energy has the largest cross sections and it gets smaller as the incident energy increases.

5.1 Cross Sections

5.1.1 Raw Cross Sections

- Acceptance Correction: The cross sections before and after the acceptance corrections were applied are shown for the ^{56}Fe target in Figure 5.1, Figure 5.2, Figure 5.3

and Figure 5.4. The black points are before and the red points are after the acceptance was applied. The red points also have the Kriging smoothing correction applied. The cross sections at 15° get lower after the acceptance correction because of the bin migration which was caused by the optics reconstruction. The bin migration is smaller at $60^\circ, 90^\circ$ and 120° than at 15°. The cross sections shown in Figure 5.1, Figure 5.2, Figure 5.3 and Figure 5.4 also include the Kriging smoothing correction.

- e^-e^+ background and radiative elastic tail Correction:

  The e^-e^+ background and the radiative elastic tail were subtracted from the quasi-elastic cross sections before the radiative corrections were applied. The results of the e^-e^+ background and the radiative elastic tail subtraction for all available angles are shown in Figure 5.5, Figure 5.6, Figure 5.7 and Figure 5.8. The radiative elastic tail and the e^-e^+ background corrections at 15° and 60° kinematics are very small compared to the e^- cross sections. These corrections are negligible at 15° . The radiative elastic tail and the e^-e^+ background corrections at 90° and 120° kinematics are larger compared to the forward angle corrections and they are shown on Figure 5.7 and Figure 5.8. Both the radiative elastic tail and the e^-e^+ background corrections are only important at small scattered electron energies. These corrections become zero at large scattered electron energies. The uncertainty due to the e^-e^+ background dominates the systematic uncertainties at small scattered electron energies.

5.1.2 Born Cross Sections and LHRS-RHRS Comparison

After the raw cross sections were corrected for the acceptance, the e^-e^+ background, and the elastic tail, the radiative corrections were applied and the Born cross sections were extracted for both the LHRS and RHRS. The LHRS and RHRS Born cross sections are compared below in Figure 5.10, Figure 5.12 and Figure 5.13 for $15^\circ, 90^\circ$ and 120°. The

cross sections at 60° are only shown for the LHRS. Unfortunately, the scattered electrons at the RHRS 60° crossed the target frame during the experiment. Therefore, the RHRS cross sections at 60° are not comparable to the LHRS cross sections. The LHRS and RHRS cross sections agree within 5% at most. The biggest difference is at 15°. The agreement between the LHRS and RHRS differential cross sections at 90° and 120° is better and the difference is less than 3%. In this analysis only the LHRS data was used to extract the longitudinal and the transverse response functions. The RHRS data was measured independently from the LHRS data and only used for comparison with the LHRS data.

5.1.2.1 Comparison with the World Data

The only existing data for ^{56}Fe, which has the same kinematics as the E05-110 experiment, is the Saclay data at 90° and $E = 400MeV$. The comparison between the E05-110 and Saclay Born cross sections is shown in Figure 5.14. The LHRS cross sections and Saclay data agree mostly within the uncertainties. The last point at large ω has the largest difference, which is less than 5%. The LHRS cross sections agree better with the Saclay data then the RHRS cross sections.

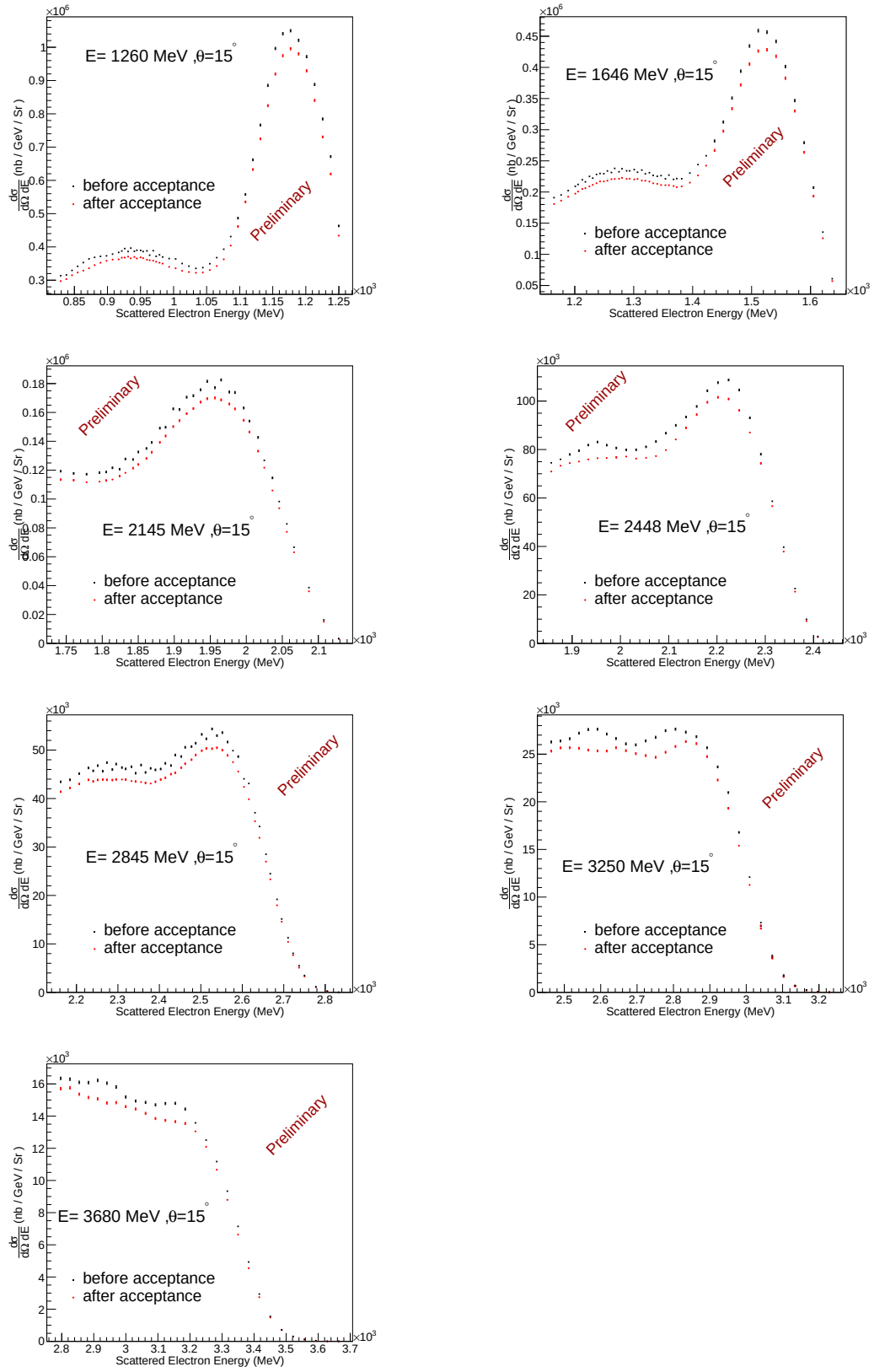

Figure 5.1: The LHRS cross sections before and after acceptance correction as a function of the scattered electron energy (MeV) at $\theta = 15^{\circ}$.

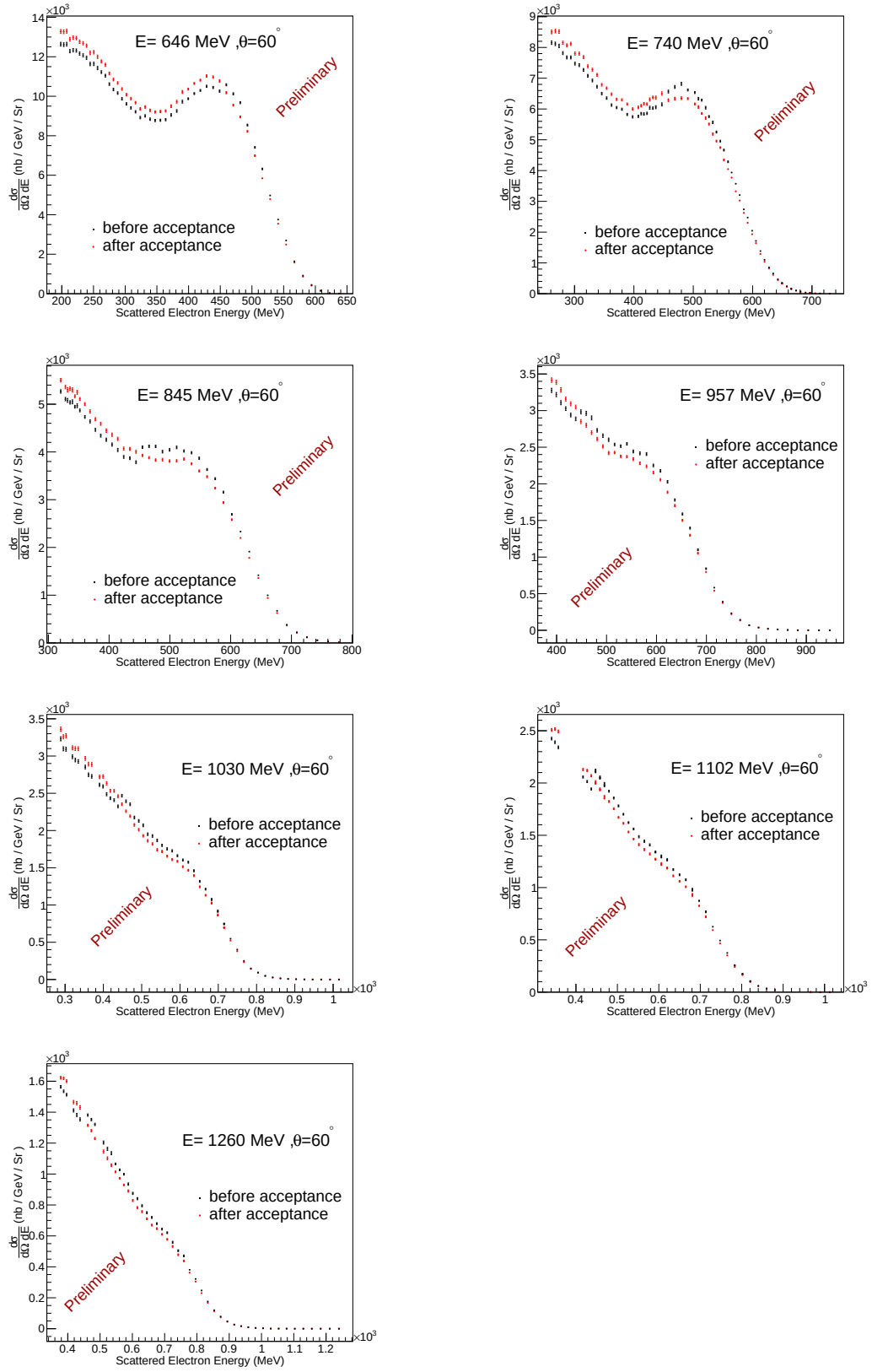

Figure 5.2: The LHRS cross sections before and after acceptance correction as a function of the scattered electron energy (MeV) at $\theta = 60^{\circ}$.

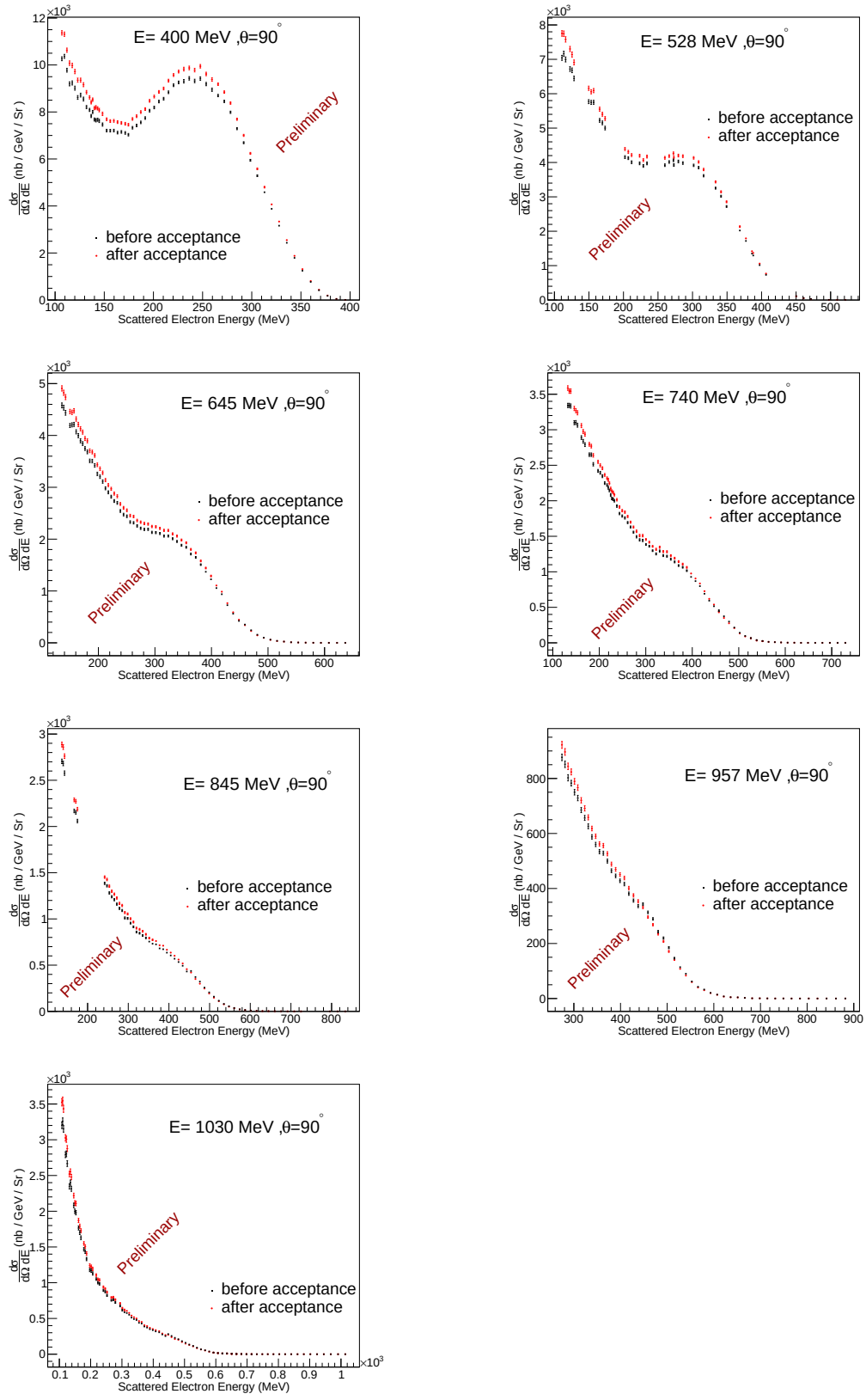

Figure 5.3: The LHRS cross sections before and after acceptance correction as a function of the scattered electron energy (MeV) at $\theta = 90^{\circ}$.

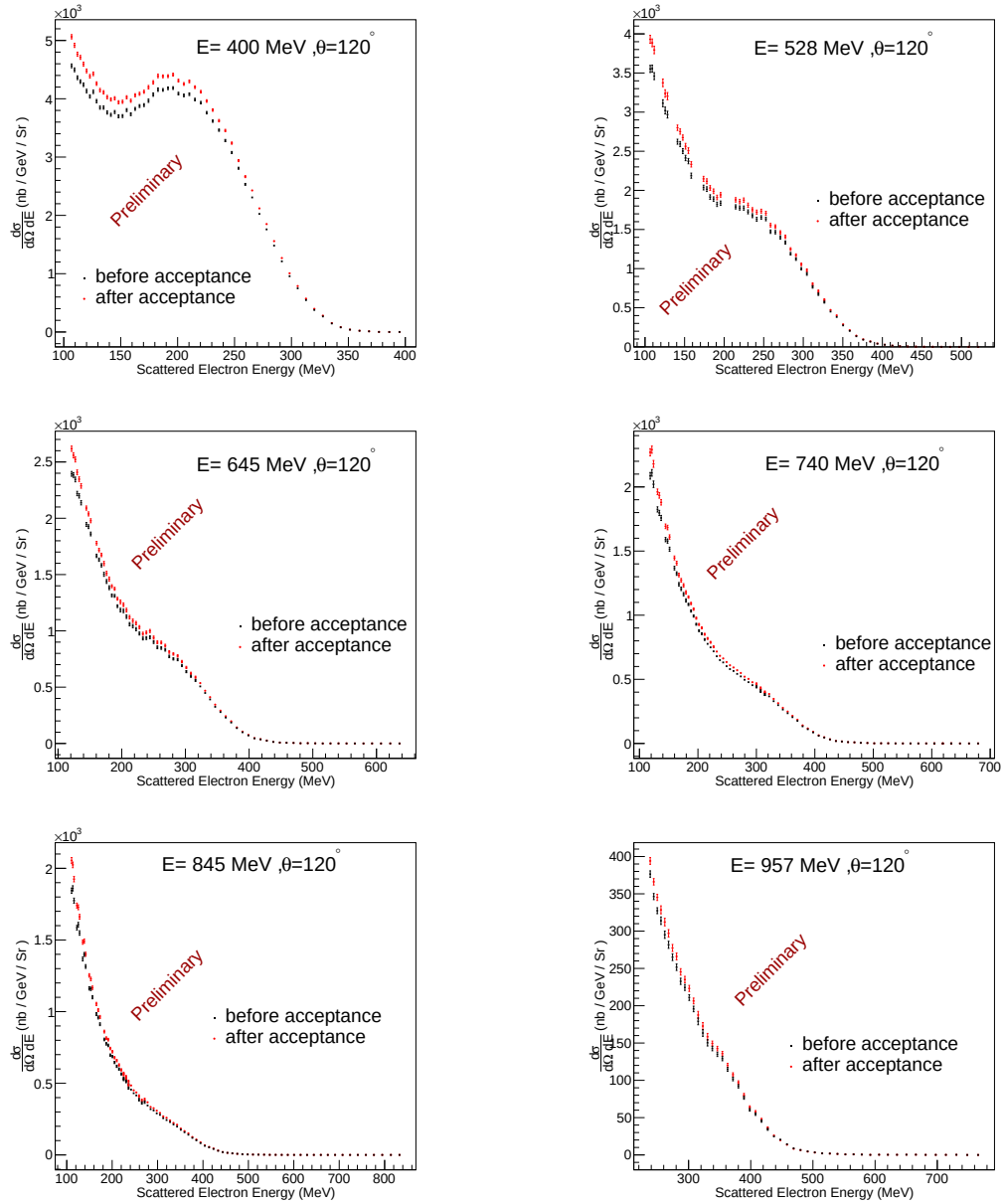

Figure 5.4: The LHRS cross sections before and after acceptance correction as a function of the scattered electron energy (MeV) at $\theta = 120^{\circ}$.

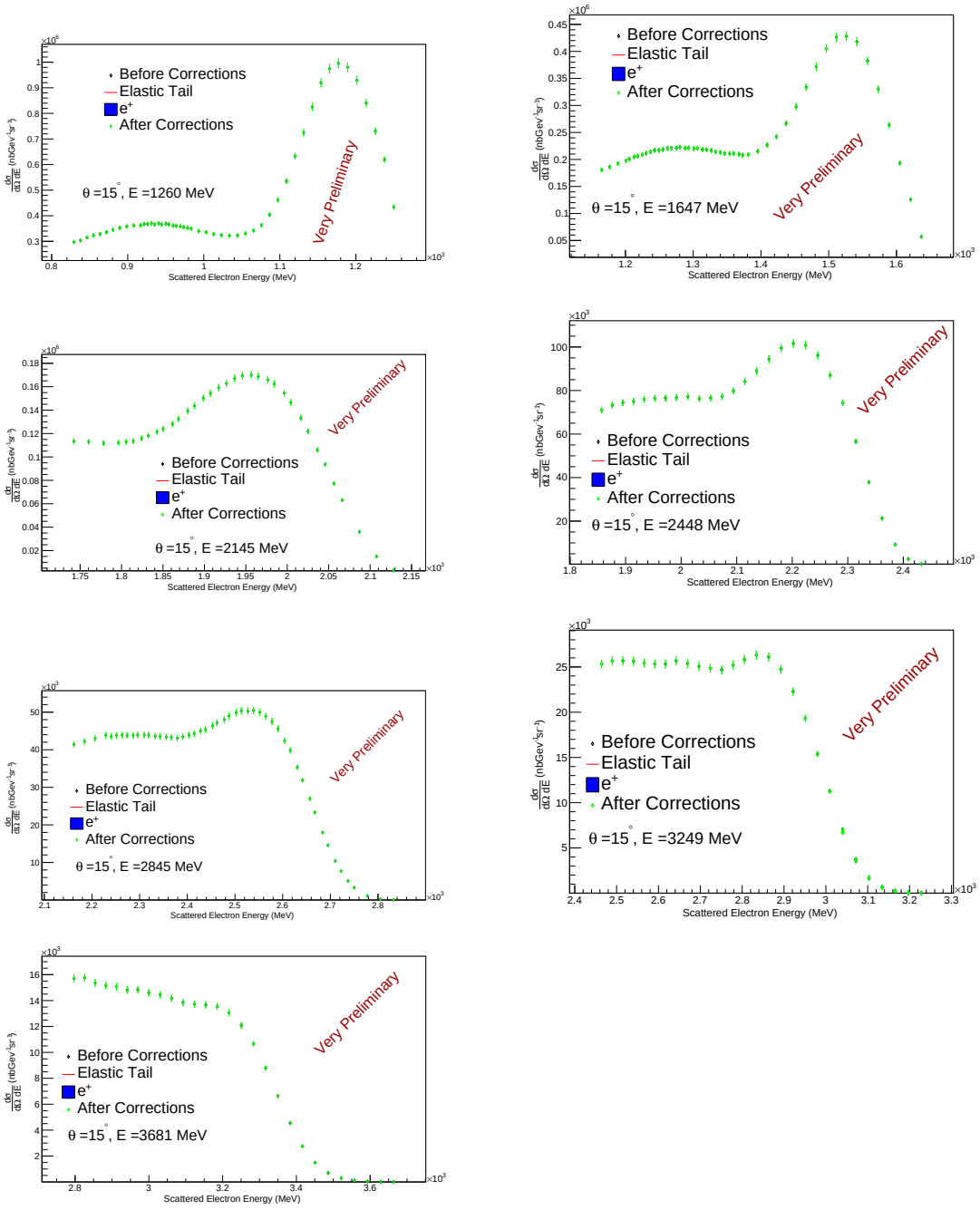

Figure 5.5: The LHRS cross sections as a function of the scattered electron energy (MeV) at $\theta = 15^{\circ}$. The black points are raw cross sections, the blue filled points are $e^{-}e^{+}$ background corrections, the red line is the radiative elastic tail correction and the green points are cross sections after $e^{-}e^{+}$ background and the radiative elastic tail corrections were applied.

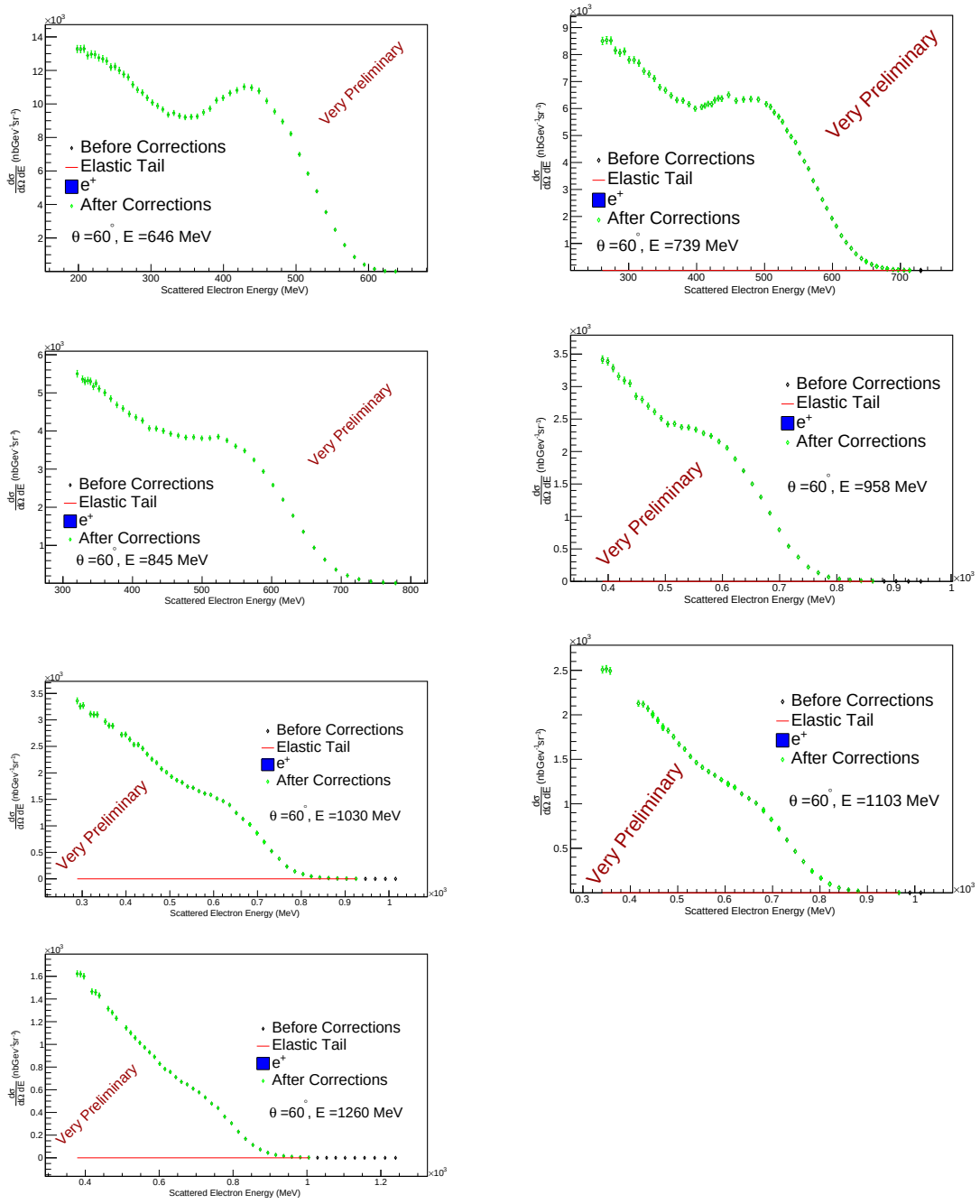

Figure 5.6: The LHRS cross sections as a function of the scattered electron energy (MeV) at $\theta = 60^\circ$. The black points are raw cross sections, the blue filled points are e^-e^+ background corrections, the red line is the radiative elastic tail correction and the green points are cross sections after e^-e^+ background and the radiative elastic tail corrections were applied.

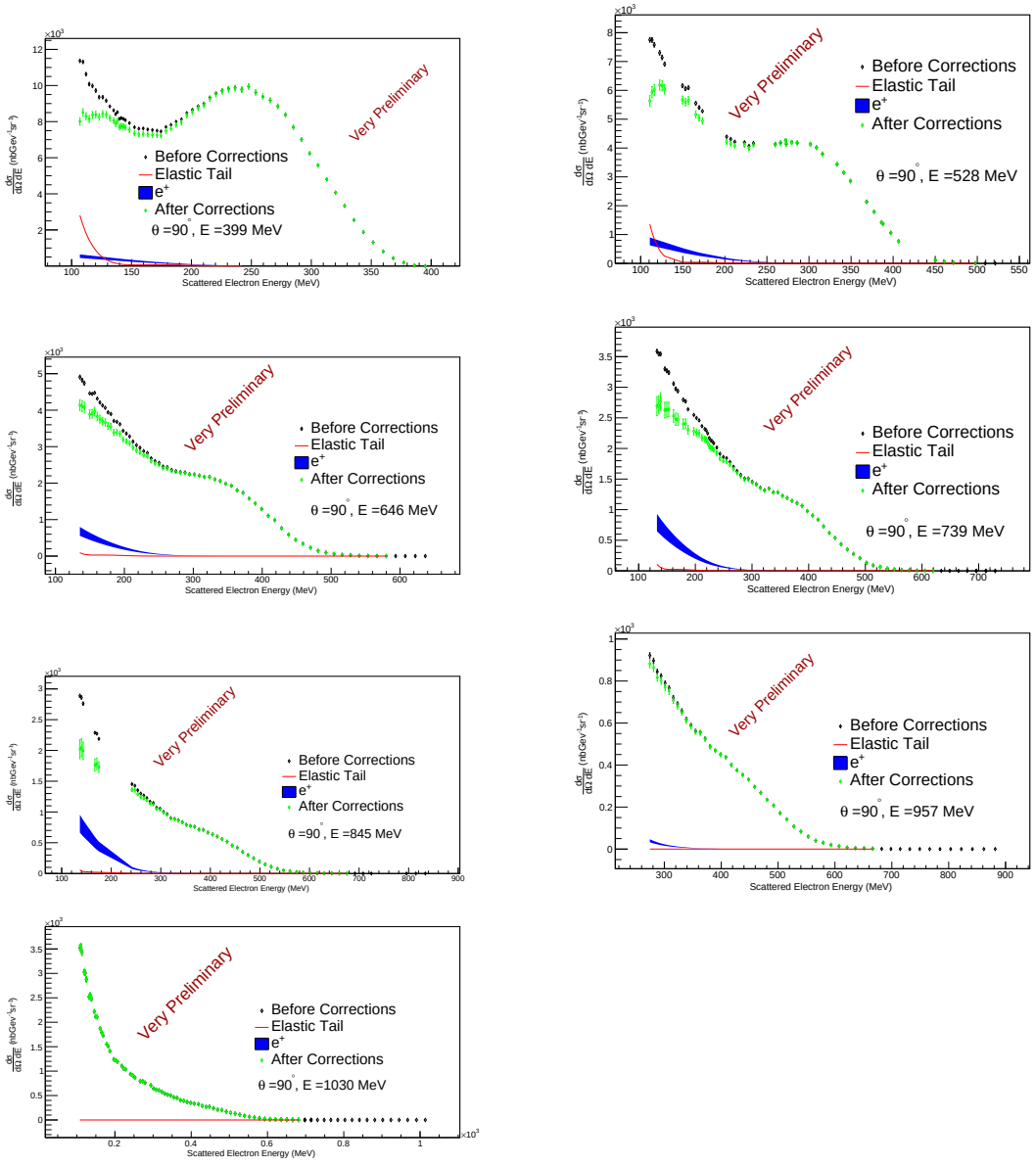

Figure 5.7: The LHRS cross sections as a function of the scattered electron energy (MeV) at $\theta = 90^\circ$. The black points are raw cross sections, the blue filled points are e^-e^+ background corrections, the red line is the radiative elastic tail correction and the green points are cross sections after e^-e^+ background and the radiative elastic tail corrections were applied.

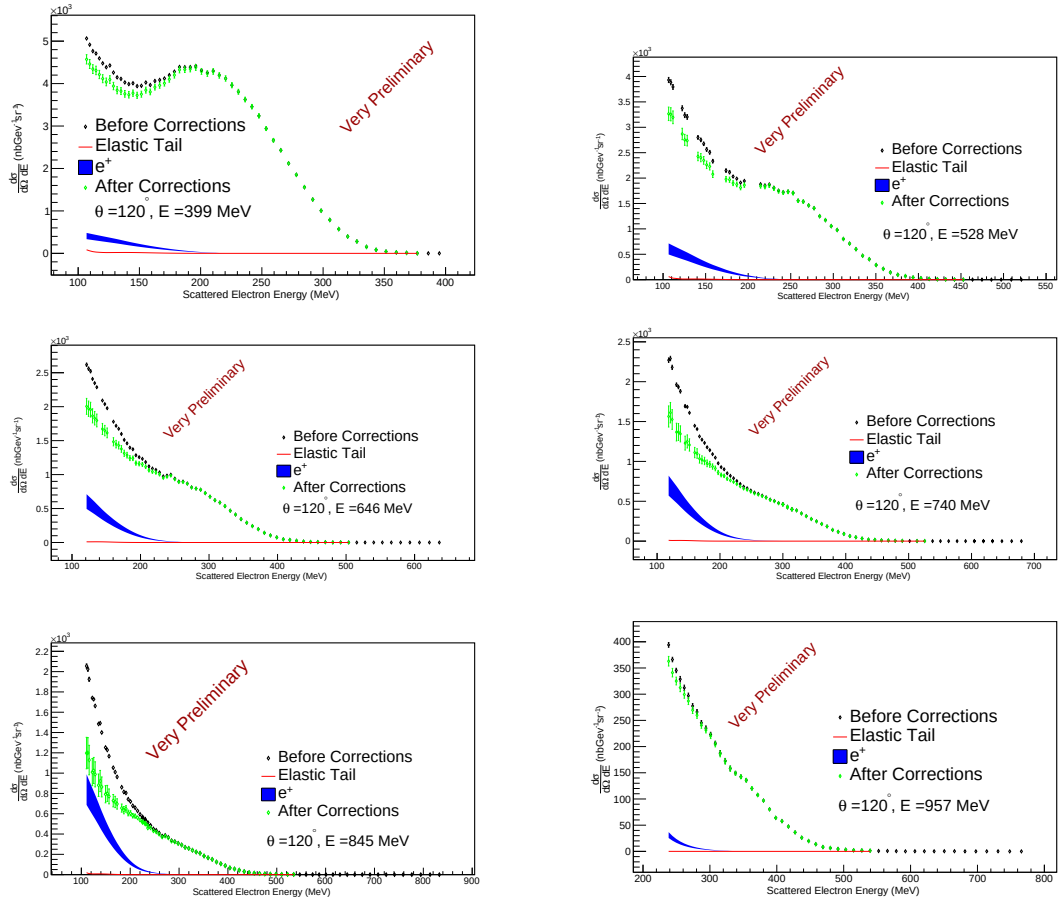

Figure 5.8: The LHRS cross sections as a function of the scattered electron energy (MeV) at $\theta = 120^{\circ}$. The black points are raw cross sections, the blue filled points are $e^{-}e^{+}$ background corrections, the red line is the radiative elastic tail correction and the green points are cross sections after $e^{-}e^{+}$ background and the radiative elastic tail corrections were applied.

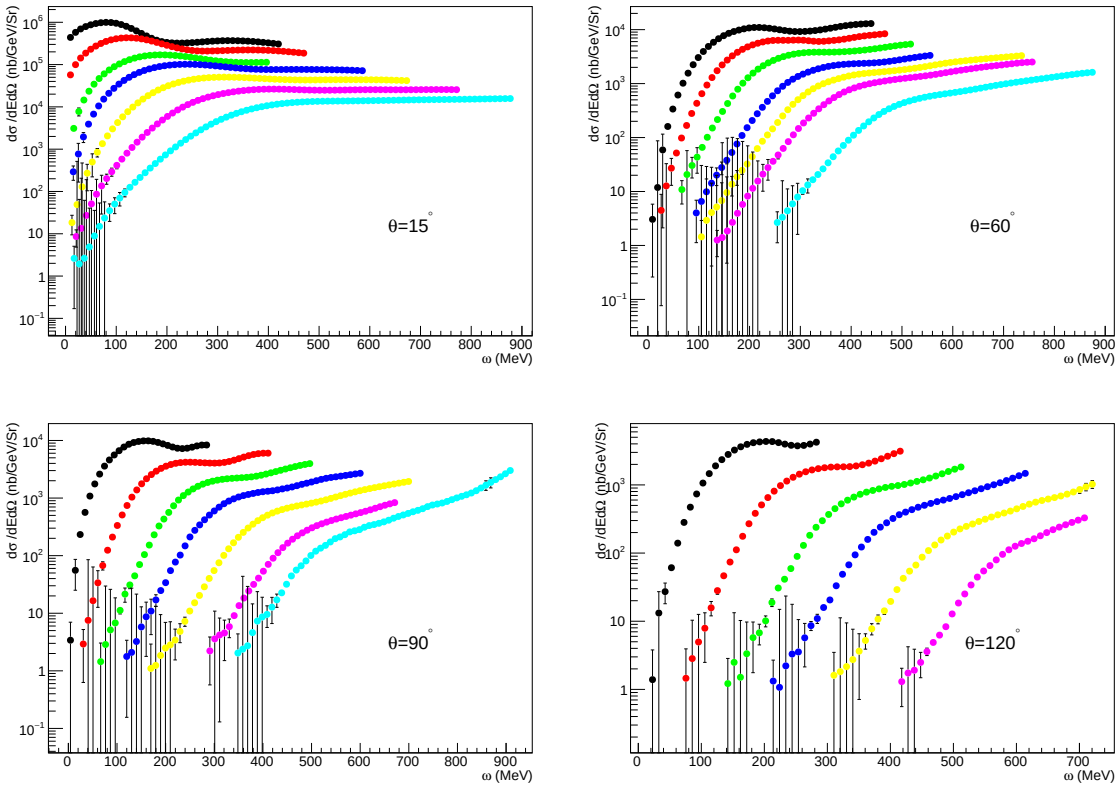

Figure 5.9: The LHRS cross sections as a function of energy loss (MeV) at $\theta = 15^\circ, 60^\circ, 90^\circ$ and 120°. Each color represents a different beam energy.

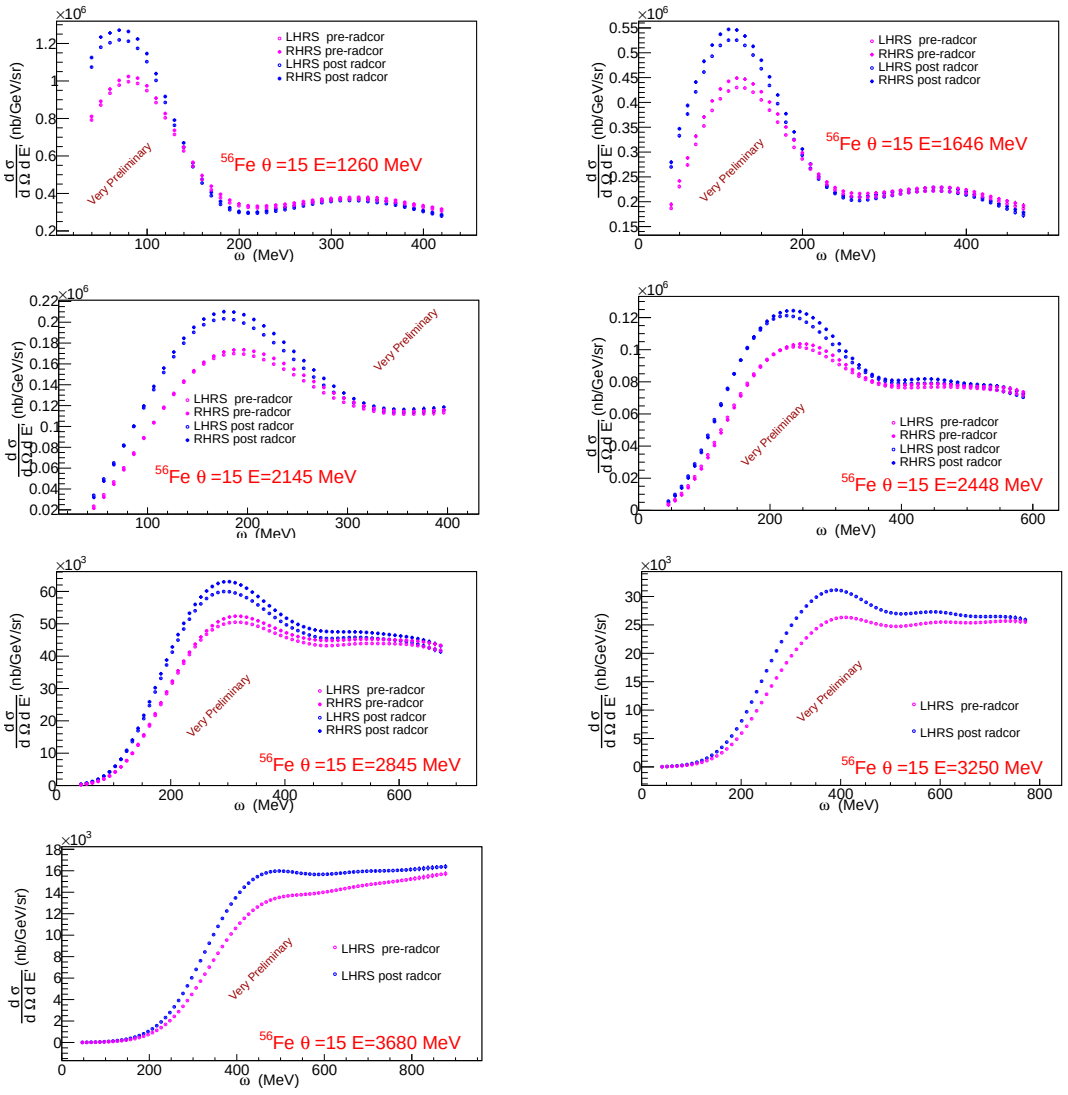

Figure 5.10: The LHRS and RHRS differential cross sections as a function of the energy loss ω at 15° . The pink points are before the radiative corrections were applied and the blue points are after it was applied. The crosses are the RHRS cross sections and the open circless are the LHRS cross sections.

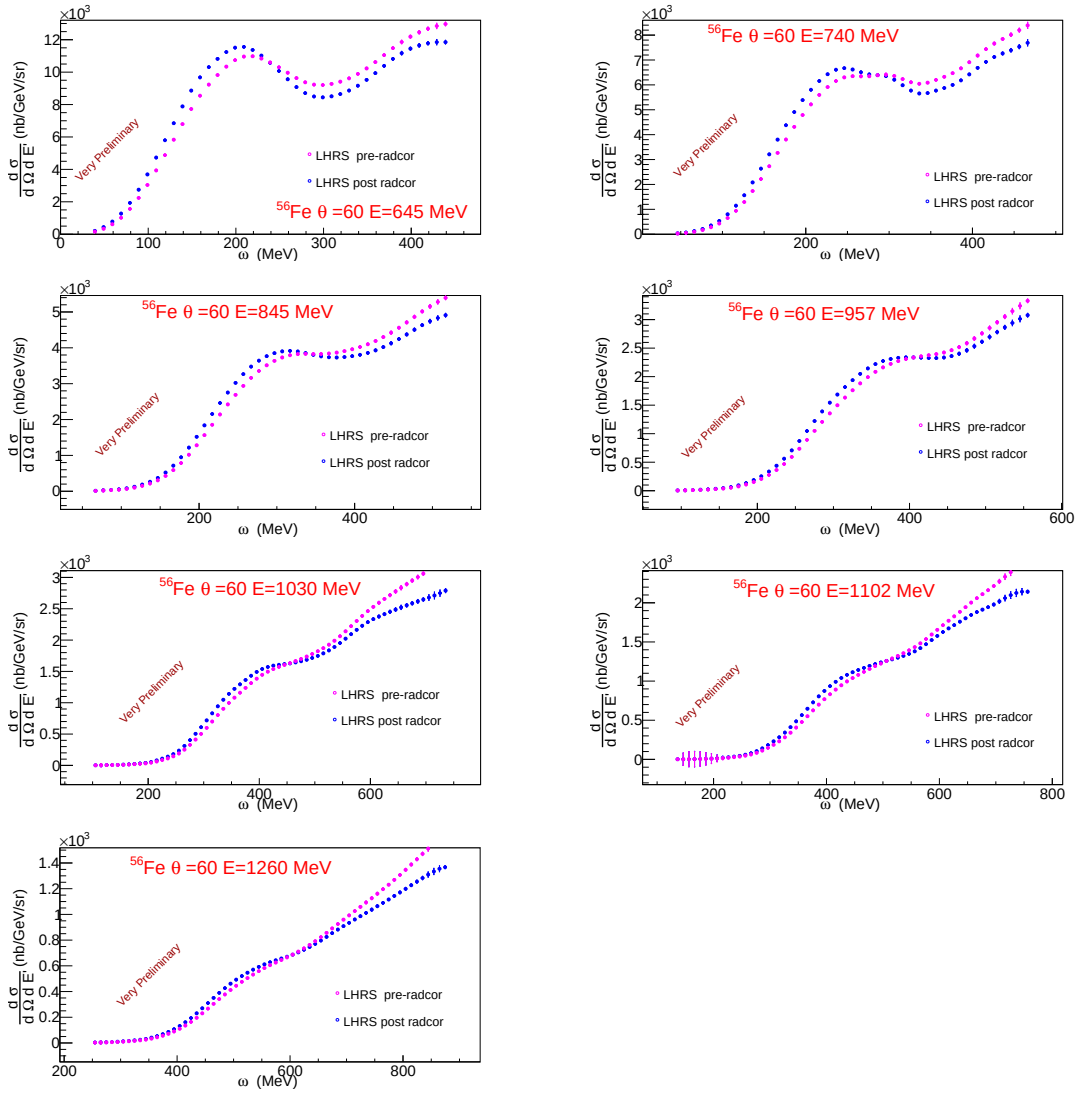

Figure 5.11: The LHRS differential cross sections as a function of the energy loss ω at 60° . The pink points are before the radiative corrections were applied and the blue points are after it was applied.

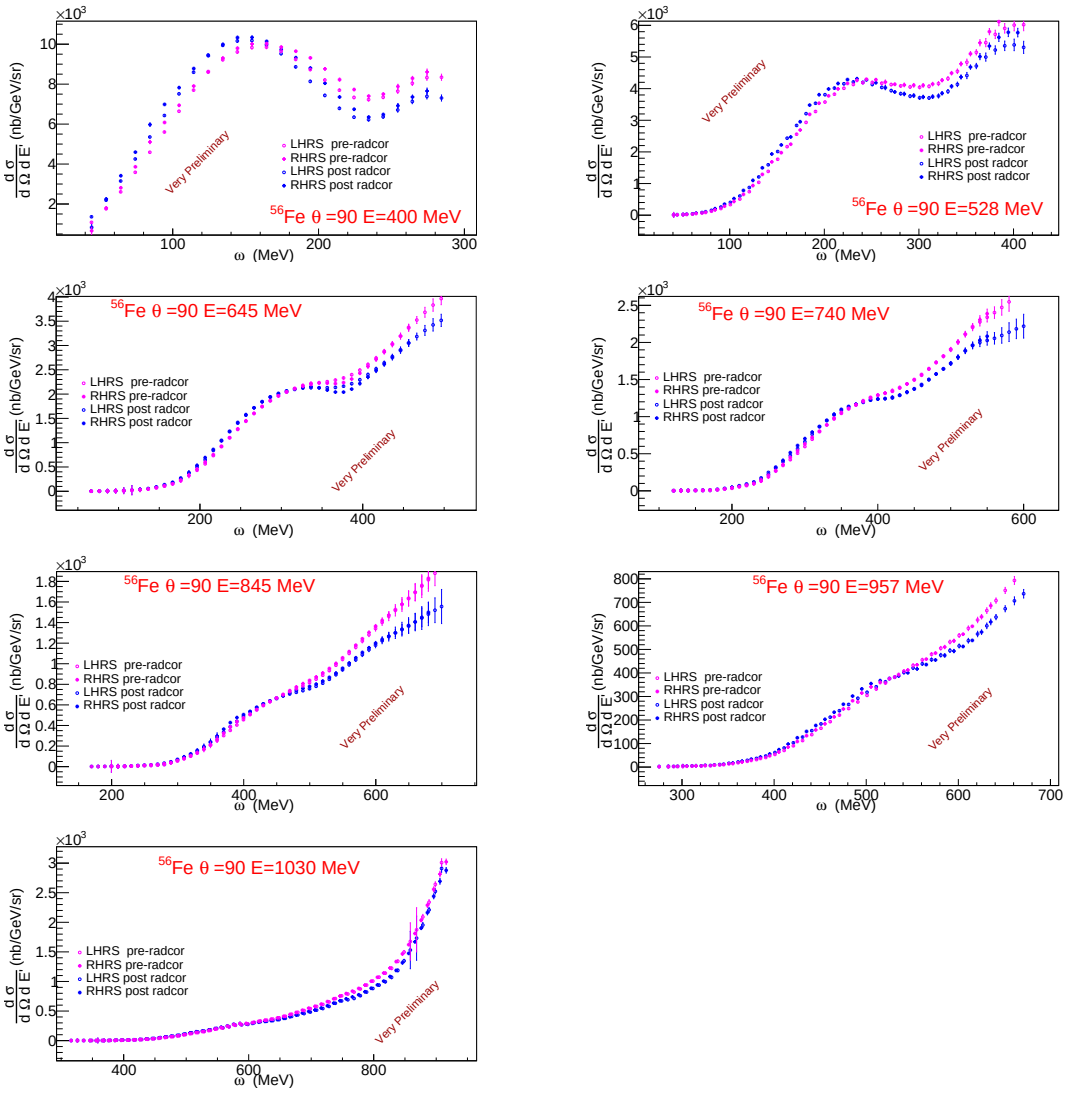

Figure 5.12: The LHRS and RHRS differential cross sections as a function of the energy loss ω at 90° . The pink points are before the radiative corrections were applied and the blue points are after it was applied. The crosses are the RHRS cross sections and the open circless are the LHRS cross sections.

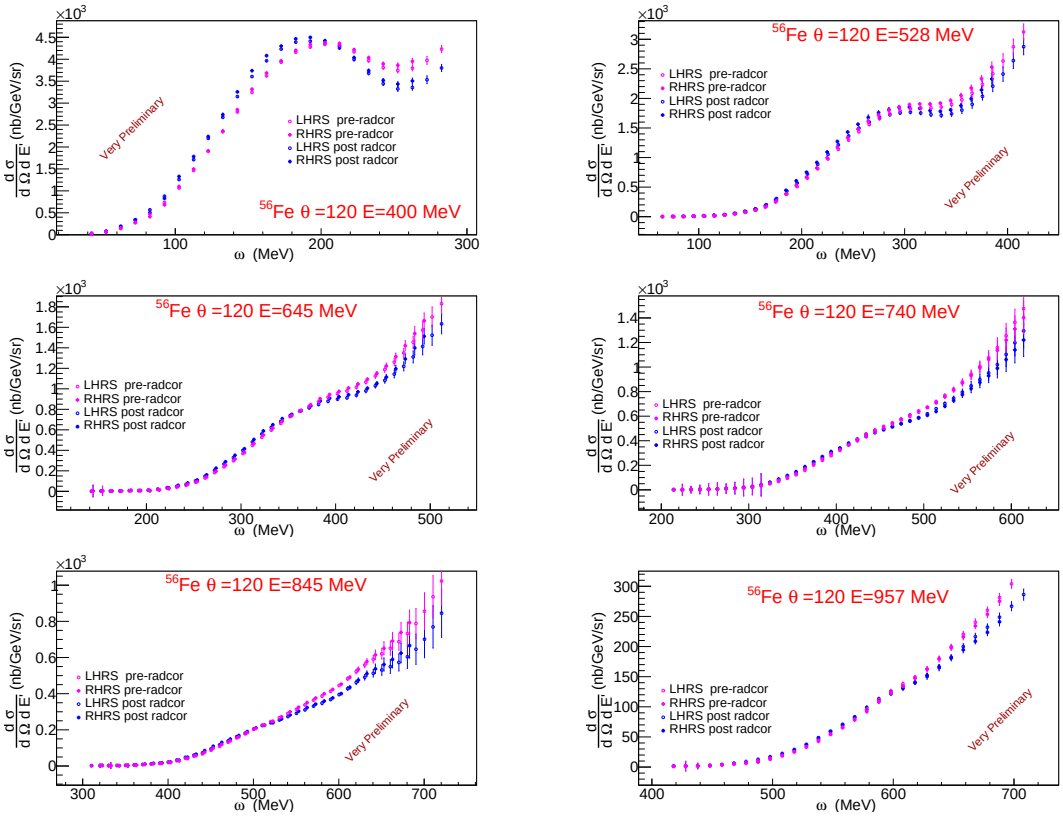

Figure 5.13: The LHRS and RHRS differential cross sections as a function of the energy loss ω at 120° . The pink points are before the radiative corrections were applied and the blue points are after it was applied. The crosses are the RHRS cross sections and the open circless are the LHRS cross sections.

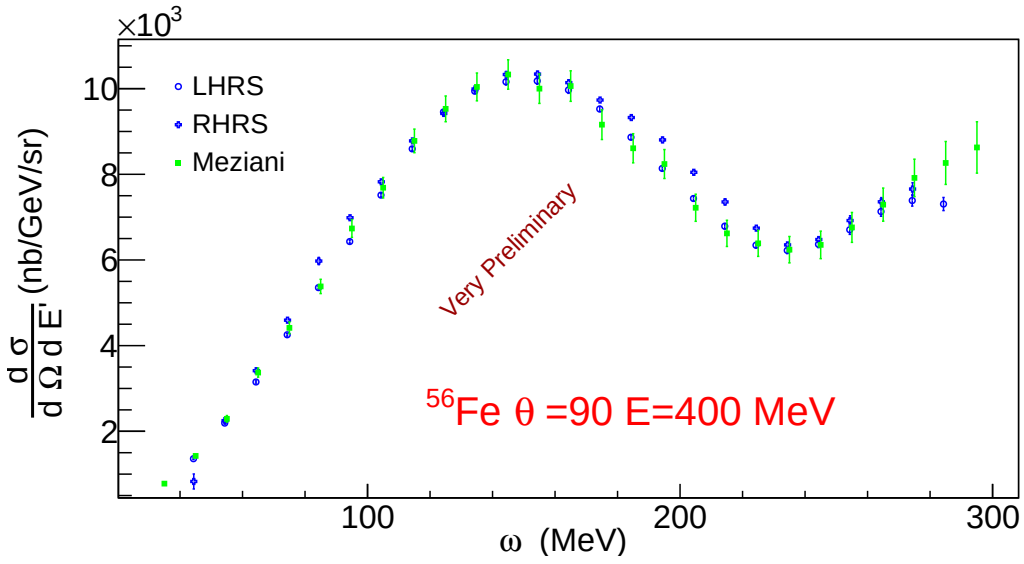

Figure 5.14: The differential cross sections of $56^F e$ at $\theta = 90^\circ$ and $E = 400MeV$ are compared to Saclay [86] data. The blue crosses are the RHRS cross sections the open circles are the LHRS cross sections and the green squares are the Saclay data.

5.2 Rosenbluth Separation and Coulomb Sum Rule

The Rosenbluth separation was performed at constant $|q| = 650MeV$. The method of least squares regression [100] was used for the interpolation along the y scaling variable up to the quasi-elastic peak and then the W variable after the quasi-elastic peak. Linear interpolation method is used for the interpolation between ω values. Figure 5.15 shows the line of constant $|q|$ on the kinematics of the experiment. After the cross sections along the constant $|q|$ were interpolated for each angle, the longitudinal and the transverse response functions R_L and R_T were extracted by a straight line fit. The slope of the straight line is the longitudinal response function times $\frac{Q^4}{\vec{q}^4}$, and the intercept is the transverse response function times $\frac{Q^2}{2\vec{q}^2}$. The preliminary results of the Rosenbluth separation at constant $|q| = 650MeV$ is shown in Figure 5.16 for 4 different ω values. The preliminary results of the Longitudinal and transverse response functions (R_L and R_T) are shown in Figure 5.17. The R_L starts from 0 at low ω and rises and then it falls to 0 again. However, the analysis of the large ω points is still ongoing. Therefore, they are not shown in the preliminary results. On the other hand, R_T starts from 0, then it falls and rises again. The preliminary results only include the statistical uncertainities. The systematic uncertainities are shown as a separate band.

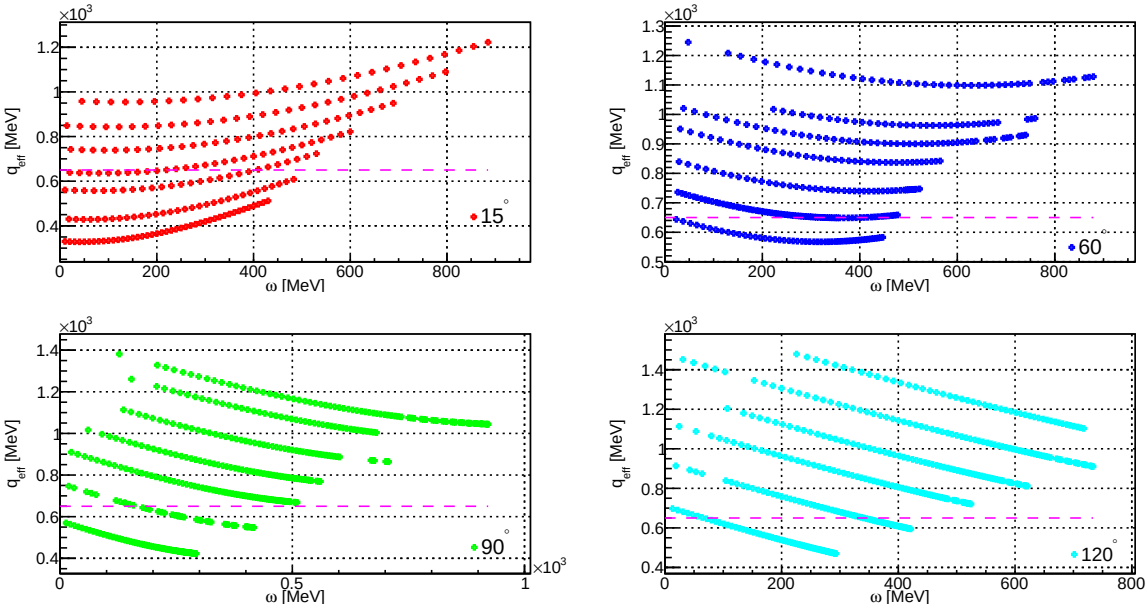

Figure 5.15: Kinematics of the E05-110 experiment. Each figure shows all available spectra at a different angle. Each line represents a different beam energy. Constant $|q| = 650$ MeV (pink) path is shown with dashed lines.

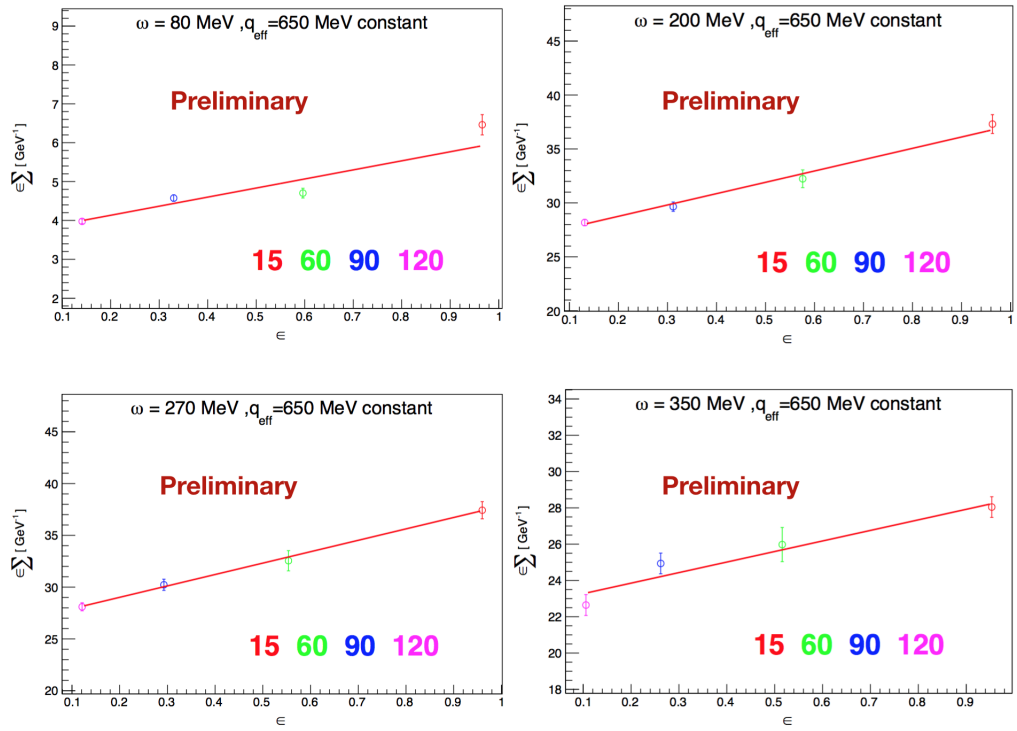

Figure 5.16: The Rosenbluth separation with 4 angles at constant $|q| = 650$ MeV. Each point represents a different angle.

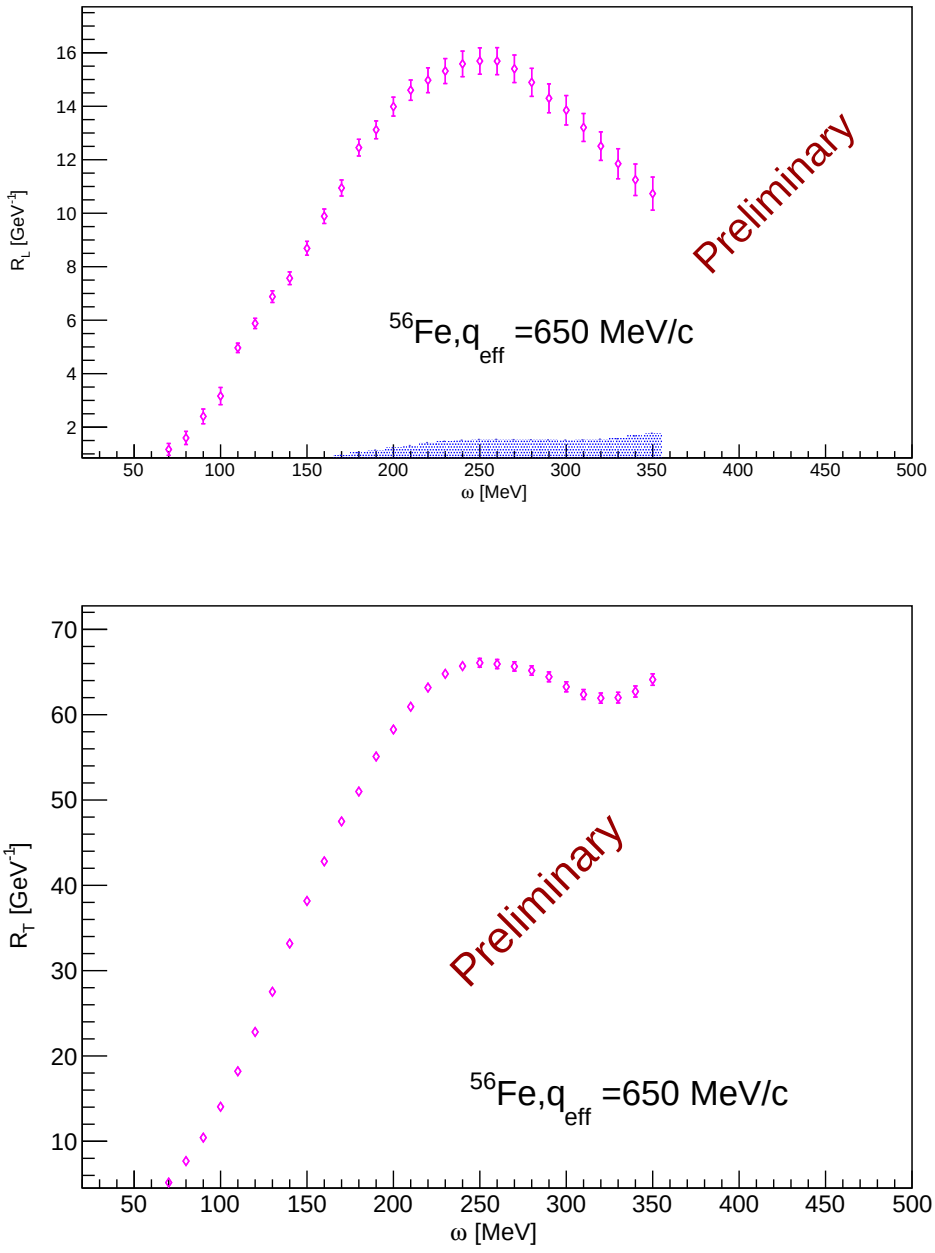

Figure 5.17: R_L and R_T are plotted as a function of electron energy loss ω at $q = 650 MeV$

CHAPTER 6

CONCLUSION

The quasi-elastic scattering data of the E05-110 experiment on ^{56}Fe was analyzed to extract the Coulomb Sum Rule. Cross sections were extracted at four scattering angles $15^{\circ}, 60^{\circ}, 90^{\circ}$ and 120°, at incident energies from $0.4GeV$ to $3.7GeV$ and at scattered electron energies from 0.1 GeV/c to 3.7 GeV/c for both the LHRS and RHRS. The performance of the detectors and other spectrometer apparatus was analyzed. The Cherenkov cut efficiencies were found to be better than 99% for the LHRS and better than 99.5% for the RHRS. The tracking efficiencies are higher than 95%. The dead time correction was found to be less than 10%. The π^- and e^-e^+ backgrounds were calculated and corrected for. The acceptance of the spectrometer was calculated by using the simulation program SAMC.

The preliminary elastic cross sections and form factors of ^{12}C were analyzed and compared to the world data . Since the percent differences between world data and the E05-110 elastic data did not indicate any patterns for a specific angle or energy, no normalization was used in this analysis. The kriging interpolation method was used to smooth the LHRS cross sections and to fill the gaps between the RHRS cross section points. The uncertainties due to the kriging interpolation were propagated with the statistical uncertainities. The radiative corrections were calculated using the Stein formula. The maximum correction was found to be 20% at 15°. After the preliminary Born cross sections were extracted, the LHRS cross sections were compared to the RHRS cross sections. The agreement between

the LHRS and RHRS cross sections was found to be 5% at 15° and less than 3% at other angles. The statistical uncertainties on the cross sections are mostly less than 1%. The statistical uncertainties get large only at low ω points. However, the large ω points were mostly not used for the extraction of R_L.

A preliminary Rosenbluth separation was performed to extract the longitudinal and transverse response functions at constant $|q| = 650$ MeV with 4 angles. To account for the Coulomb distortion, the effective momentum approximation was used. The 4 points that were used for the Rosenbluth separation align well with each other at ω values close the quasi-elastic peak. At large ω values the quality of the straight line fit gets worse. The study on these points is still ongoing. Therefore, they were not included in the preliminary extraction of the R_L.

The previous measurements of the Coulomb Sum at low momentum transfers show a large quenching of the longitudinal response function. There is only one data point [43] at large momentum transfer. However, this point has large uncertainties. The E05-110 experiment results is expected to fill the gaps in the large momentum transfers and indicate whether the Coulomb Sum Rule is quenched or not. However, results of this analysis are very preliminary and it is very early to make a decision on whether the quenching exists or not.

More experimental studies are required to extraxt the Coulomb Sum Rule. The systematic uncertainties need to be improved. The agreement between the LHRS and RHRS needs to be understood better than 1%. The Coulomb Sum needs to be extracted at larger momentum transfers. The Coulomb Sum needs to be extracted also for ^{12}C,^{4}He and ^{208}Pb targets to study the medium dependency of the results.

REFERENCES

[1] L. W. Alvarez and F. Bloch, Phys. Rev. **57**, 111 (1940), URL https://link.aps.org/doi/10.1103/PhysRev.57.111.

[2] M. Gell-Mann, Phys. Lett. **8**, 214 (1964).

[3] G. Zweig, Tech. Rep., CERN (1964), 8182/TH 401.

[4] J.-P. Chen, Ph.D. thesis, University of Virginia (1990).

[5] J. D. Walecka, *Electron Scattering for Nuclear and Nucleon Structure* (Cambridge, 2004).

[6] R. Hofstadter, Rev. Mod. Phys. **28**, 214 (1956), URL https://link.aps.org/doi/10.1103/RevModPhys.28.214.

[7] T. W. Donnelly, , and J. D. Walecka, Annual Review of Nuclear Science **25**, 329 (1975), http://dx.doi.org/10.1146/annurev.ns.25.120175.001553, URL http://dx.doi.org/10.1146/annurev.ns.25.120175.001553.

[8] O. Benhar, D. Day, and I. Sick, Rev. Mod. Phys. **80**, 189 (2008), URL https://link.aps.org/doi/10.1103/RevModPhys.80.189.

[9] R. Hofstadler, *The Electron-Scattering Method and its Application to the Structure of Nuclei and Nucleons* (1961), URL https://www.nobelprize.org/

nobel_prizes/physics/laureates/1961/hofstadter-lecture.pdf.

[10] K. Foster, *Electron Scattering: Form Factors and Nuclear* (2011), URL http://www.physics.uoguelph.ca/~garrettp/teaching/PHY-7160/Lecture1KyleFoster.pdf.

[11] D. J. R. Dr. Walter Greiner, *Quantum Electrodynamics* (Springer, 2009).

[12] M. N. Rosenbluth, Phys. Rev. **79**, 615 (1950), URL https://link.aps.org/doi/10.1103/PhysRev.79.615.

[13] F. Halzen and A. D. Martin, *Quarks and Leptons* (John Wiley and Sons, 1984).

[14] A. Meucci, M. Vorabbi, C. Giusti, F. D. Pacati, and P. Finelli, Phys. Rev. **C87**, 054620 (2013), 1302.3390.

[15] C. Horowitz and J. Piekarewicz, Nuclear Physics A **511**, 461 (1990), ISSN 0375-9474, URL http://www.sciencedirect.com/science/article/pii/037594749090105U.

[16] J. Aubert, G. Bassompierre, K. Becks, C. Best, E. Bhm, X. de Bouard, F. Brasse, C. Broll, S. Brown, J. Carr, et al., Physics Letters B **123**, 275 (1983), ISSN 0370-2693, URL http://www.sciencedirect.com/science/article/pii/0370269383904379.

[17] J. Morgenstern and Z. E. Meziani, Phys. Lett. **B515**, 269 (2001), nucl-ex/0105016.

[18] T. D. Forest, Nuclear Physics A **414**, 347 (1984), ISSN 0375-9474, URL http://www.sciencedirect.com/science/article/pii/0375947484906079.

[19] G. Orlandini and M. Traini, Reports on Progress in Physics **54**, 257 (1991), URL http://stacks.iop.org/0034-4885/54/i=2/a=002.

[20] R. Rosenfelder, Annals of Physics **128**, 188 (1980), ISSN 0003-4916, URL http://www.sciencedirect.com/science/article/pii/0003491680900597.

[21] A. Dellafiore and M. Traini, Nuclear Physics A **344**, 509 (1980), ISSN 0375-9474, URL http://www.sciencedirect.com/science/article/pii/0375947480904042.

[22] J. Lightbody, Physics Letters B **33**, 129 (1970), ISSN 0370-2693, URL http://www.sciencedirect.com/science/article/pii/0370269370902807.

[23] S. Stringari, Phys. Rev. C **29**, 1482 (1984), URL https://link.aps.org/doi/10.1103/PhysRevC.29.1482.

[24] A. Dellafiore and D. Brink, Nuclear Physics A **286**, 474 (1977), ISSN 0375-9474, URL http://www.sciencedirect.com/science/article/pii/0375947477905966.

[25] F. Dellagiacoma, G. Orlandini, and M. Traini, Nuclear Physics A **393**, 95 (1983), ISSN 0375-9474, URL http://www.sciencedirect.com/science/article/pii/0375947483900660.

[26] S. D. Drell and C. L. Schwartz, Phys. Rev. **112**, 568 (1958), URL https://link.aps.org/doi/10.1103/PhysRev.112.568.

[27] K. W. McVoy and L. Van Hove, Phys. Rev. **125**, 1034 (1962), URL https://link.aps.org/doi/10.1103/PhysRev.125.1034.

[28] R. Altemus, A. Cafolla, D. Day, J. S. McCarthy, R. R. Whitney, and J. E. Wise, Phys. Rev. Lett. **44**, 965 (1980), URL https://link.aps.org/doi/10.1103/PhysRevLett.44.965.

[29] M. Deady, C. F. Williamson, J. Wong, P. D. Zimmerman, C. Blatchley, J. M. Finn, J. LeRose, P. Sioshansi, R. Altemus, J. S. McCarthy, et al., Phys. Rev. C **28**, 631 (1983), URL https://link.aps.org/doi/10.1103/PhysRevC.28.631.

[30] A. Hotta, P. J. Ryan, H. Ogino, B. Parker, G. A. Peterson, and R. P. Singhal, Phys. Rev. C **30**, 87 (1984), URL https://link.aps.org/doi/10.1103/PhysRevC.30.87.

[31] M. Deady, C. F. Williamson, P. D. Zimmerman, R. Altemus, and R. R. Whitney, Phys. Rev. C **33**, 1897 (1986), URL https://link.aps.org/doi/10.1103/PhysRevC.33.1897.

[32] C. C. Blatchley, J. J. LeRose, O. E. Pruet, Zimmerman, P. D., C. F. Williamson, and M. Deady, Phys. Rev. C **34**, 1243 (1986), URL https://link.aps.org/doi/10.1103/PhysRevC.34.1243.

[33] S. A. Dytman, A. M. Bernstein, K. I. Blomqvist, T. J. Pavel, B. P. Quinn, R. Altemus, J. S. McCarthy, G. H. Mechtel, T. S. Ueng, and R. R. Whitney, Phys. Rev. C **38**, 800 (1988), URL https://link.aps.org/doi/10.1103/PhysRevC.38.800.

[34] K. Dow, S. Dytman, D. Beck, A. Bernstein, I. Blomqvist, H. Caplan, D. Day, M. Deady, P. Demos, W. Dodge, et al., Phys. Rev. Lett. **61**, 1706 (1988), URL https://link.aps.org/doi/10.1103/PhysRevLett.61.1706.

[35] P. Barreau, M. Bernheim, J. Duclos, J. Finn, Z. Meziani, J. Morgenstern, J. Mougey, D. Royer, B. Saghai, D. Tarnowski, et al., Nuclear Physics A **402**,

515 (1983), ISSN 0375-9474, URL http://www.sciencedirect.com/science/article/pii/0375947483902178.

[36] Z. E. Meziani, P. Barreau, M. Bernheim, J. Morgenstern, S. Turck-Chieze, R. Altemus, J. McCarthy, L. J. Orphanos, R. R. Whitney, G. P. Capitani, et al., Phys. Rev. Lett. **52**, 2130 (1984), URL https://link.aps.org/doi/10.1103/PhysRevLett.52.2130.

[37] Z. E. Meziani, P. Barreau, M. Bernheim, J. Morgenstern, S. Turck-Chieze, R. Altemus, J. McCarthy, L. J. Orphanos, R. R. Whitney, G. P. Capitani, et al., Phys. Rev. Lett. **54**, 1233 (1985), URL https://link.aps.org/doi/10.1103/PhysRevLett.54.1233.

[38] C. Marchand, P. Barreau, M. Bernheim, P. Bradu, G. Fournier, Z. Meziani, J. Miller, J. Morgenstern, J. Picard, B. Saghai, et al., Physics Letters B **153**, 29 (1985), ISSN 0370-2693, URL http://www.sciencedirect.com/science/article/pii/0370269385914352.

[39] A. Zghiche, J. Danel, M. Bernheim, M. Brussel, G. Capitani, E. D. Sanctis, S. Frullani, F. Garibaldi, A. Gerard, J. L. Goff, et al., Nuclear Physics A **572**, 513 (1994), ISSN 0375-9474, URL http://www.sciencedirect.com/science/article/pii/0375947494903999.

[40] D. T. Baran, B. F. Filippone, D. Geesaman, M. Green, R. J. Holt, H. E. Jackson, J. Jourdan, R. D. McKeown, R. G. Milner, J. Morgenstern, et al., Phys. Rev. Lett. **61**, 400 (1988), URL https://link.aps.org/doi/10.1103/PhysRevLett.61.400.

[41] J. P. Chen, Z. E. Meziani, D. Beck, G. Boyd, L. M. Chinitz, D. B. Day, L. C. Dennis, G. Dodge, B. W. Filippone, K. L. Giovanetti, et al., Phys.

Rev. Lett. **66**, 1283 (1991), URL https://link.aps.org/doi/10.1103/PhysRevLett.66.1283.

[42] Z.-E. Meziani, J. P. Chen, D. Beck, G. Boyd, L. M. Chinitz, D. B. Day, L. C. Dennis, G. E. Dodge, B. W. Fillipone, K. L. Giovanetti, et al., Phys. Rev. Lett. **69**, 41 (1992), URL https://link.aps.org/doi/10.1103/PhysRevLett.69.41.

[43] J. P. Chen, Z. E. Meziani, D. Beck, G. Boyd, L. M. Chinitz, D. B. Day, L. C. Dennis, G. Dodge, B. W. Filippone, K. L. Giovanetti, et al., Phys. Rev. Lett. **66**, 1283 (1991), URL https://link.aps.org/doi/10.1103/PhysRevLett.66.1283.

[44] R. Schiavilla, D. Lewart, V. Pandharipande, S. C. Pieper, R. Wiringa, and S. Fantoni, Nuclear Physics A **473**, 267 (1987), ISSN 0375-9474, URL http://www.sciencedirect.com/science/article/pii/037594748790145X.

[45] J. V. Noble, Phys. Rev. Lett. **46**, 412 (1981), URL https://link.aps.org/doi/10.1103/PhysRevLett.46.412.

[46] A. Fabrocini and S. Fantoni, Nuclear Physics A **503**, 375 (1989), ISSN 0375-9474, URL http://www.sciencedirect.com/science/article/pii/0375947489902418.

[47] J. Jourdan, Physics Letters B **353**, 189 (1995), ISSN 0370-2693, URL http://www.sciencedirect.com/science/article/pii/0370269395005815.

[48] G. D. Dang and N. Van Giai, Phys. Rev. C **30**, 731 (1984), URL http://link.aps.org/doi/10.1103/PhysRevC.30.731.

[49] G. D. Dang and P. Van Thieu, Phys. Rev. C **28**, 1845 (1983), URL http://link.aps.org/doi/10.1103/PhysRevC.28.1845.

[50] S. Fantoni and V. Pandharipande, Nuclear Physics A **473**, 234 (1987), ISSN 0375-9474, URL http://www.sciencedirect.com/science/article/pii/0375947487901448.

[51] C. R. Chinn, A. Picklesimer, and J. W. Van Orden, Phys. Rev. C **40**, 790 (1989), URL http://link.aps.org/doi/10.1103/PhysRevC.40.790.

[52] L. S. Celenza, A. Harindranath, and C. M. Shakin, Phys. Rev. C **33**, 1012 (1986), URL http://link.aps.org/doi/10.1103/PhysRevC.33.1012.

[53] L. S. Celenza, A. Harindranath, C. M. Shakin, and A. Rosenthal, Phys. Rev. C **32**, 650 (1985), URL http://link.aps.org/doi/10.1103/PhysRevC.32.650.

[54] P.J. and Mulders, Nuclear Physics A **459**, 525 (1986), ISSN 0375-9474, URL http://www.sciencedirect.com/science/article/pii/0375947486901594.

[55] I. Sick, Physics Letters B **157**, 13 (1985), ISSN 0370-2693, URL http://www.sciencedirect.com/science/article/pii/037026938591202X.

[56] B. F. Wehrberger K., Springer-few body systems **5** (1992), URL https://link.springer.com/chapter/10.1007/978-3-7091-7617-7_52.

[57] X. Ji, Physics Letters B **219**, 143 (1989), ISSN 0370-2693, URL http://www.sciencedirect.com/science/article/pii/0370269389903651.

[58] I. C. Cloët, W. Bentz, and A. W. Thomas, Phys. Rev. Lett. **116**, 032701 (2016), URL https://link.aps.org/doi/10.1103/PhysRevLett.116.032701.

[59] Z.-E. M. S. Choi, J.-P.Chen, CSR Experiment Proposal, PR-05-110, http://hallaweb.jlab.org,andthereferencestherein.

[60] J. Alcorn et al., Nucl. Instrum. Meth. A **522**, 294 (2004).

[61] C. Leeman, D. Douglas, and G. Krafft, Nucl. Part. Sci. **51** (2001).

[62] D. Flay, Ph.D. thesis, Temple University (2014).

[63] D.W.Higinbotham and T.Keppel, Tech. Rep., Jefferson Lab (2016), URL http://hallaweb.jlab.org/index/safety-docs/2014-Fall-Run/Standard-Equipment-Manual.pdf.

[64] C. Yan, P. Adderley, R. Carlini, C. Cuevas, W. Vulcan, and R. Wines, Nuclear Instruments and Methods in Physics Research Section A: Accelerators, Spectrometers, Detectors and Associated Equipment **365**, 46 (1995), ISSN 0168-9002, URL http://www.sciencedirect.com/science/article/pii/0168900295005048.

[65] N. Liyanage, Tech. Rep., Jefferson Lab (2002), JLab-TN-02-012, URL http://hallaweb.jlab.org/publications/Technotes/files/2002/02-012.pdf.

[66] H. Yao, Ph.D. thesis, Temple University (2008).

[67] *User's guide to the hall a cryotarget*, URL https://userweb.jlab.org/~ckeith/Atarg/ATARG_MAN.html.

[68] D. Meekins, *Hall a Target Configuration* (2007), URL https://hallaweb.jlab.org/dvcslog/CSR/150814_111924/Hall_A_Target_Configuration.pdf.

[69] *Hall a hrs*, URL http://jlab.org.

[70] K. Fissum et al., Tech. Rep., Jefferson Laboratory (2000), jLab-TN-00-016.

[71] K. Fissum, W. Bertozzi, J. Chen, D. Dale, H. Fenker, J. Gao, A. Gavalya, S. Gilad, C. Leathers, N. Liyanage, et al., Nuclear Instruments and Methods in Physics

Research Section A: Accelerators, Spectrometers, Detectors and Associated Equipment **474**, 108 (2001), ISSN 0168-9002, URL //www.sciencedirect.com/science/article/pii/S0168900201008750.

[72] V. Lindenstruth and I. Kisel, Nuclear Instruments and Methods in Physics Research Section A: Accelerators, Spectrometers, Detectors and Associated Equipment **535**, 48 (2004), ISSN 0168-9002, proceedings of the 10th International Vienna Conference on Instrumentation, URL http://www.sciencedirect.com/science/article/pii/S0168900204015748.

[73] T. F. C Bromberg, A Das, *Introduction to Nuclear and Particle Physics* (World Scientific, 1994), 2nd ed.

[74] *Shower calorimeter overview*, URL http://hallaweb.jlab.org/document/OPMAN-old/node167.html.

[75] *Daq*, URL https://www.jlab.org/div_dept/consortium/07Series/DAbbott.pdf.

[76] S. Lewis, Tech. Rep., Lawrence Berkeley National Laboratory (1998), URL http://www.epics.org/overview.pdf.

[77] *ROOT: C++ Data Analysis Framework*, http://root.cern.ch/drupal/.

[78] *ROOT/C++ Analyzer for Hall A*, http://hallaweb.jlab.org/podd/.

[79] Y. Oh, Ph.D. thesis, Seoul National University (2013).

[80] A. Deur, Tech. Rep., Jefferson Lab (2000), jLab-TN33, URL http://hallaweb.jlab.org/physics/experiments/he3/g2/temp/document.html.

[81] L. Mo and Y. Tsai, Rev. Mod. Phys. **41**, 205 (1969).

[82] C. Patrignani et al. (Particle Data Group), Chin. Phys. **C40**, 100001 (2016).

[83] J. LeRose, *Snake transfer functions*, https://hallaweb.jlab.org/news/minutes/tranferfuncs.html.

[84] C. Rasmussen and C. K. I. Williams, *Gaussian Processes for Machine Learning* (MIT Press, 2006).

[85] J. O'CONNELL and J. J.W. LIGHTBODY, *Epc.f*.

[86] Z.-E. Meziani, Ph.D. thesis, Universite de Paris (1984).

[87] S. Stein et al., Phys. Rev. D **12**, 1884 (1975).

[88] P. E. Bosted and V. Mamyan (2012), 1203.2262.

[89] K. Slifer, Tech. Rep., Temple University (2003), jLab-TN44, URL http://hallaweb.jlab.org/physics/experiments/he3/g2/temp/document.html.

[90] I. Sick, D. Day, and J. S. McCarthy, Phys. Rev. Lett. **45**, 871 (1980), URL https://link.aps.org/doi/10.1103/PhysRevLett.45.871.

[91] C. Ciofi degli Atti, E. Pace, and G. Salmè, Phys. Rev. C **43**, 1155 (1991), URL https://link.aps.org/doi/10.1103/PhysRevC.43.1155.

[92] *The richards curve*, URL http://www.pisces-conservation.com/growthhelp/index.html?richards_curve.htm.

[93] Y.-S. Tsai (1971), SLAC-PUB-0848.

[94] Y.-S. Tsai, Phys. Rev. **122**, 1898 (1961), URL https://link.aps.org/doi/10.1103/PhysRev.122.1898.

[95] J.Ravenhal, *ravenhal.f* (1986).

[96] F. Weissbach, K. Hencken, D. Trautmann, and I. Sick, Phys. Rev. C **80**, 064605 (2009), URL https://link.aps.org/doi/10.1103/PhysRevC.80.064605.

[97] P. Guèye, M. Bernheim, J. F. Danel, J. E. Ducret, L. Lakéhal-Ayat, J. M. Le Goff, A. Magnon, C. Marchand, J. Morgenstern, J. Marroncle, et al., Phys. Rev. C **60**, 044308 (1999), URL https://link.aps.org/doi/10.1103/PhysRevC.60.044308.

[98] J. Arrington, C. D. Roberts, and J. M. Zanotti, Journal of Physics G: Nuclear and Particle Physics **34**, S23 (2007), URL http://stacks.iop.org/0954-3899/34/i=7/a=S03.

[99] S. Galster, H. Klein, J. Moritz, K. Schmidt, D. Wegener, and J. Bleckwenn, Nuclear Physics B **32**, 221 (1971), ISSN 0550-3213, URL http://www.sciencedirect.com/science/article/pii/055032137190068X.

[100] P. R. Bevington and D. Robinson, *Data Reduction and Error Analysis* (McGraw-Hill Higher Education, 2003).

[101] J. Schwinger, Phys. Rev. **74**, 1439 (1948), URL https://link.aps.org/doi/10.1103/PhysRev.74.1439.

[102] J. Schwinger, Phys. Rev. **75**, 651 (1949), URL https://link.aps.org/doi/10.1103/PhysRev.75.651.

[103] J. Schwinger, Phys. Rev. **76**, 790 (1949), URL https://link.aps.org/doi/10.1103/PhysRev.76.790.

[104] L. C. Maximon and D. B. Isabelle, Phys. Rev. **133**, B1344 (1964), URL https://link.aps.org/doi/10.1103/PhysRev.133.B1344.

[105] H. Theissen, *Springer Tracts In Modern Physics Volume 65* (Springer, 1972).

[106] R. Zielinski, Tech. Rep., University of New Hampshire (2014).

[107] J. Maxwell, Tech. Rep., Univ. of Virginia (2011).

[108] R. Altulmus and J. Wise, *rosetail.f, fortran analysis code*.

[109] *Nuclei charge density archive*, http://www.faculty.virginia.edu/ncd/download.htm.

[110] R. Early, Nuclear Instruments and Methods **109**, 93 (1973), ISSN 0029-554X, URL http://www.sciencedirect.com/science/article/pii/0029554X73904540.

[111] G. Miller, Ph.D. thesis, Stanford University (1971).

[112] D. Yennie, S. Frautschi, and H. Suura, Annals of Physics **13**, 379 (1961), ISSN 0003-4916, URL http://www.sciencedirect.com/science/article/pii/0003491661901518.

[113] *World quasi-elastic cross sections on iron*, URL http://galileo.phys.virginia.edu/~dbd/Data-archive/Fe/Fe-index.php.

APPENDIX A

RADIATIVE CORRECTIONS

The cross section formula that was shown in Equation 1.10 is defined in the Born approximation. The Born aproximation assumes that a single virtual photon exchanges between the incident electron and the struck proton. However, higher order contributions (in α, the fine structure constant) have to be calculated and corrected for. All of these corrections are studied well in the Quantum Electrodynamic Theory and called the radiative corrections. Julian Schwinger was one of the first people who treated radiative corrections for the inelastic electron scattering experiments [101–103]. The Feynmann diagrams for the radiative corrections are shown in Figure A.1.

In an inclusive electron scattering experiment the energy of electrons can not be measured exactly at the scattering vertex. For incident electrons it is measured before electrons reach the scattering vertex, and for scattered electrons it is measured far away from the scattering vertex. Electrons loose energy when they go through the target material due to the Bremsstrahlung radiation and the ionization (Landau straggling) [104]. Thus, the energy of electrons right before and after the scattering vertex differs from the measured energies.

To extract a reliable Coulomb Sum Rule, the Born cross sections at the scattering vertex has to be calculated first. The incoming and scattered energies at the scattering vertex can be calculated by using the radiative corrections. When the energies at the scattering vertex are known, the corresponding cross sections can be extracted by using an interpolation and

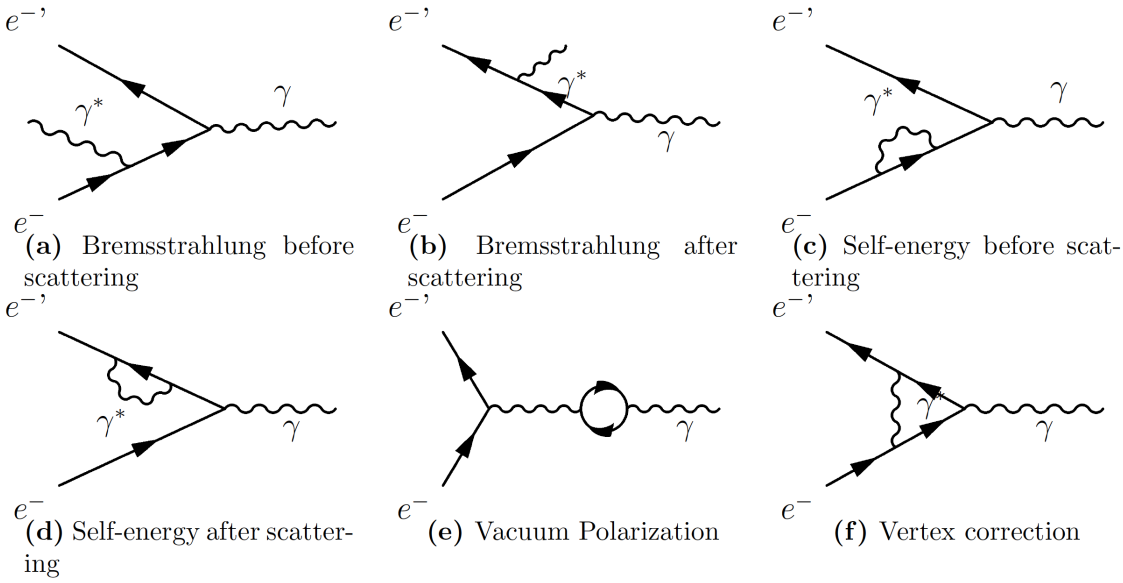

Figure A.1: Feynmann diagrams for radiative corrections. Figure from [66]

extrapolation procedure from the measured spectra. Thus, measuring more spectra will allow the extraction of more reliable Born cross sections. However, it is not possible to collect data at every single beam energy and momentum setting during an experiment due to time limitations. The number of spectra to be measured for the radiative corrections must be planned before running the experiment.

The radiative corrections have contributions from four different effects: radiation at the scattering vertex (internal), radiation before scattering (external before), radiation after scattering (external after) and energy loss due to the ionization (Landau straggling) [105]. The ionization loss is considered to happen before and after scattering. The Bremsstrahlung emission of the electron when passing through the medium before and after the scattering is called the external radiative corrections and the Bremsstrahlung emission during the collision is called internal radiative corrections. The internal radiative corrections are proportional to T, while both the ionization and the external corrections are proportional to T^2 [81].

The radiative corrections can be as high as 20% for our kinematic settings. Thus, it is important to calculate the radiative corrections accurately. We will follow Mo and Tsai

[81] and Stein [87] formula in this analysis which requires the elastic radiative tail due to the elastic scattering from the target nucleus to be subtracted, before the quasi-elastic radiative corrections are done. Therefore, the radiative elastic tail calculation is explained first.

A.1 Elastic Tail

According to Isabelle, *"The elastic radiative tail appears because of the emission of real hard photons, and is an extension of the elastic scattering peak"* [104].

Stein further explains, *"The elastic form factor is a rapid function of q^2, so this process affects mainly very lowE' region of each line where hard photons can be radiated, yielding an effective q^2 that is small"* [87].

In the E05-110 experiment analysis, Rosetail.f Fortran code was used to extract the elastic radiative tail. The Fortran code follows the Mo and Tsai [81] formula which has three parts: internal, external and multiple photon correction. The formula can be written as:

$$\sigma_{\text{el.tail}} = (\sigma_{\text{int}} + \sigma_{\text{ext}} + \sigma_{\text{coll}})F_{\text{soft}} \tag{A.1}$$

Here σ_{int} ,σ_{ext}, σ_{coll} and F_{soft} define internal Bremsstrahlung, external Bremsstrahlung, collisional loss and soft photon correction, respectively. [106]

A.1.1 External Correction

The external radiative correction takes into account the bremsstrahlung and the ionization loss in the target and the target window. As it can be seen in the figure Figure A.2 thicknesses tb and ta refer to the radiation lengths before and after scattering. The tb and ta have unit of radiation lengths x_0. The effect of the external bremmstrahlung can be approximated by assuming that the scattering took place at exactly half path length. This approximation

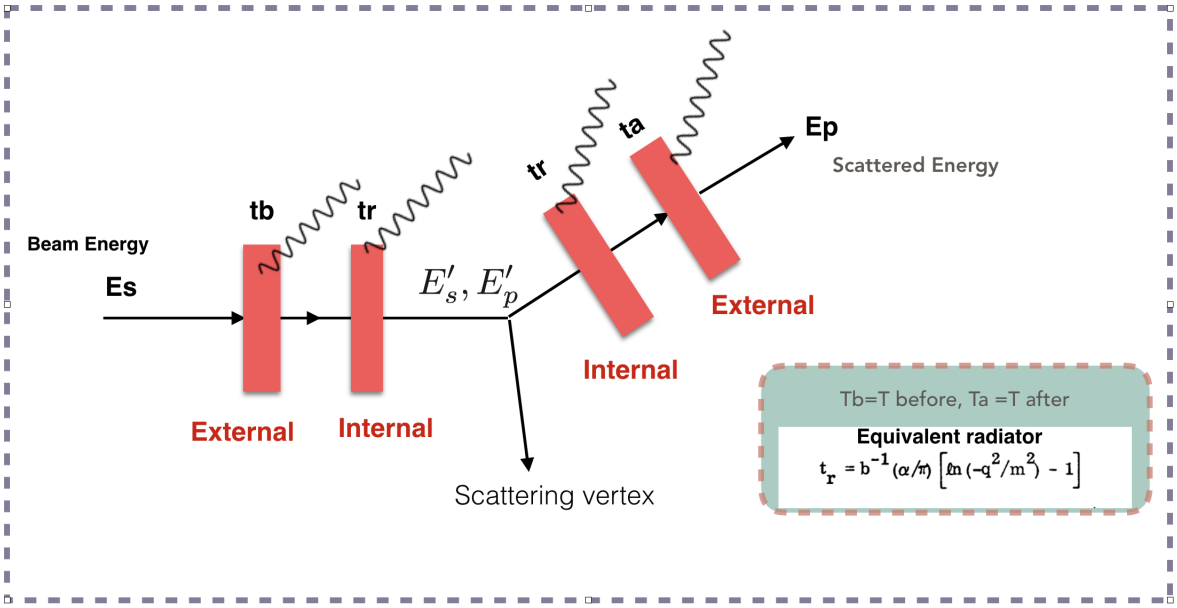

Figure A.2: Radiative Corrections Procedure.

is done in order to avoid the integration with respect to the path of the electron [81].

A.1.2 Internal Correction

The exact calculation of the Internal correction accounts for one-photon exchange and single-photon emission by integrating over kinematic factors and the elastic structure functions $W_1^{el}(q^2)$ and $W_2^{el}(^2)$ [107]. The effect of the internal bremsstrahlung is roughly the same as that given by two external radiators with one placed before and one after scattering, each of thickness (equivalent radiator method) [81]:

$$t_r = b_{-1}(\alpha/\pi)[ln(-q^2/m^2) - 1] \tag{A.2}$$

A.1.3 Multiple Photon Correction

The cross sections for single photon emission from both the internal and external effects are corrected to account for the multiple soft-photon emission by multiplying:

$$F_{soft} = (\frac{\omega_s}{E_s})^{b(t_b+t_r)}(\frac{\omega_p}{E_p+\omega_p})^{b(t_a+t_r)}, \quad \text{(A.3)}$$

where t_r is the thickness of an equivalent radiator used to take into account the internal soft-photon emission [106].

A.1.4 Elastic Tail Correction Procedure

The rosetail.f [108] uses the form factors as an input to calculate the elastic tail. Another fortran code ravenshift.f is used to calculate the form factors for Fe^{56} with the charge densities which were calculated by using the Fourier-Bessel coefficients [109]. The form factors for Fe^{56} at 120° data, which were extracted from the Fourier-Bessel coefficients, are shown in the figure Figure A.4. The rosetail.f code was used to extract the radiated elastic tail cross sections. These cross sections were subtracted from the experimental cross sections before the radiative corrections were applied. The elastic tail correction is very small for high E' (scattered energy). However, it gets larger for low E', and at lowest E' it can be as large as 22%.

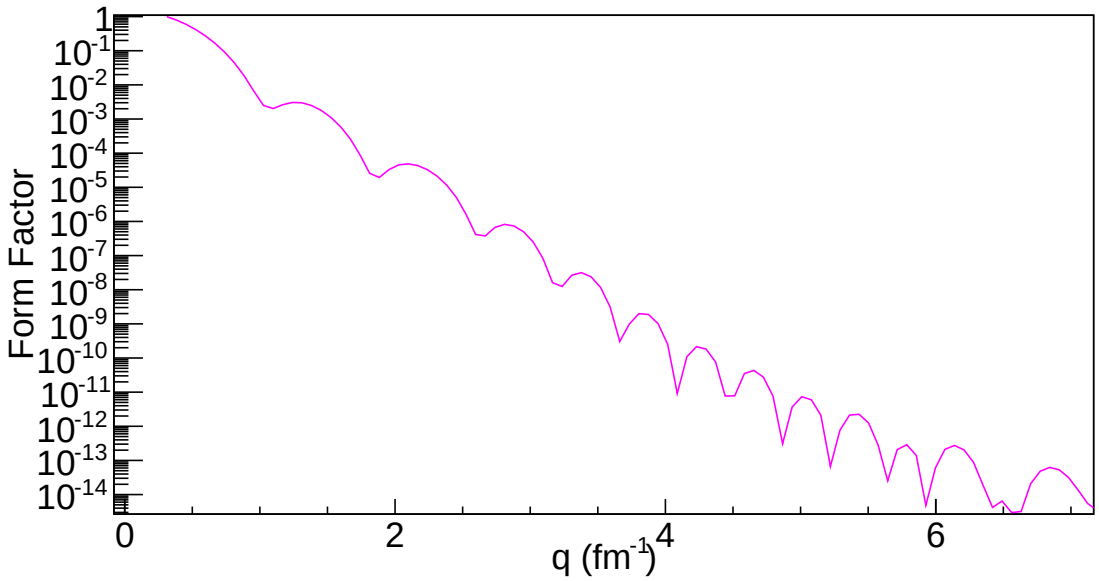

Figure A.3: The form Factors which were extracted from the Fourier -Bessel coefficients for Fe^{56} at $\theta = 120°$.

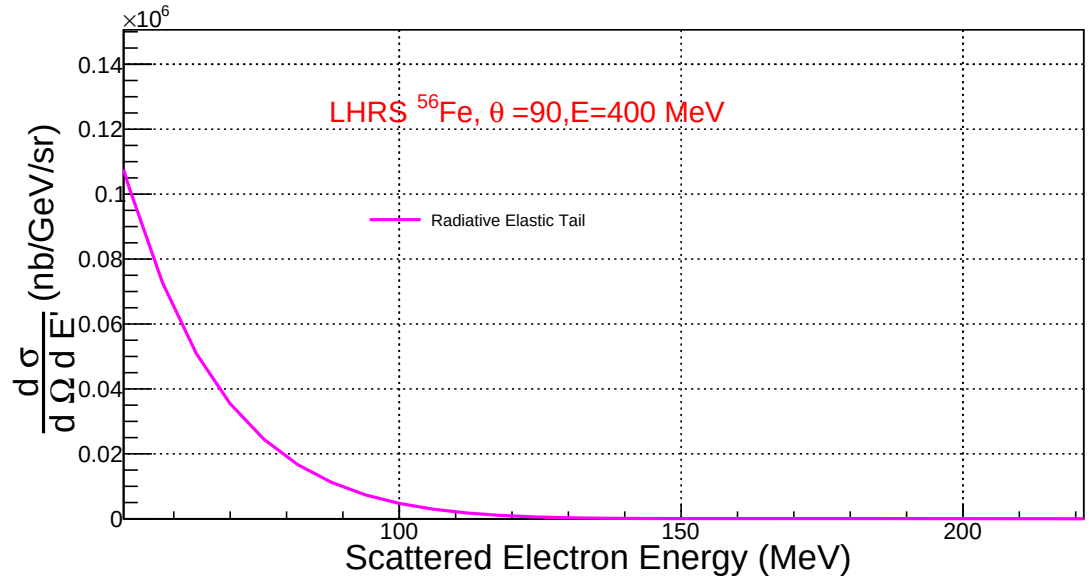

Figure A.4: The radiative elastic tail for Fe^{56} at 90° and E = 400 MeV (incident).

A.2 Quasielastic Radiative Corrections

The radiative corrections for the quasi-elastic data were calculated by Stein formula [87]. The Stein formula is based on the work of Mo and Tsai [81, 110, 111]. This formula uses some approximations to integrate the bremsstrahlung probability function (Equation A.5) over the target thickness, the scattered electron energy and the incident electron energy (see Equation A.4). The first approximation is the angle peaking approximation which assumes the emitted photon direction to be same as the incident or the scattered electron direction. The angle peaking approximation reduces the thickness integral to T/2, where T is the target thickness in units of the radiation lengths. The target thicknesses for the E05-110 experiment are given Figure A.6.

$$\sigma_{exp} = \int_0^T \frac{dt}{T} \int_{E_{smin}}^{E_s} dE'_s \int_{E_p}^{E_{pmax}} dE'_p I(E_s, E'_s, t)\sigma_r(E'_s, E'_p)I(E'_p, E_p, T-t) \tag{A.4}$$

$$I(E_s, E_p, t) = bt(1+0.5772bt)(\frac{\Delta E}{E})^{bt-1}\frac{1}{E}(1-\frac{\Delta E}{E}+\frac{3}{4}(\frac{\Delta E}{E})^2) \tag{A.5}$$

To calculate the internal bremsstrahlung, the equivalent radiator approximation, which uses two radiators one before and one after scattering, was used. The equivalent radiator thickness is given in Equation A.2. Finally, the energy peaking approximation is used to reduce the double integral on E_s and E_p to two linear integrals. The Stein formula is given below in Equation A.6:

$$\begin{aligned}\sigma_{exp} = (\frac{R\Delta}{E_s})^{b(t_b+t_r)}(\frac{\Delta}{E_p})^{b(t_a+t_r)}(1-\frac{\xi}{(1-b(t_a+t_b+2t_r))\Delta})\sigma^{eff}(E_s,E_p) \\ + \int_{E_{smin}}^{E_s-R\Delta}\sigma^{eff}(E_s',E_p)(\frac{E_s-E_s'}{E_pR})^{b(t_a+t_r)}(\frac{E_s-E_s'}{E_s})^{b(t_b+t_r)} \\ x\Big[\frac{b(t_b+t_r)}{E_s-E_s'}\phi(\frac{E_s-E_s'}{E_s})+\frac{\xi}{2(E_s-E_s')^2}\Big]dE_s' \\ + \int_{E_p+\Delta}^{E_{pmax}}\sigma^{eff}(E_s,E_p')(\frac{E_p'-E_p}{E_p'})^{b(t_a+t_r)}(\frac{(E_p'-E_p)R}{E_s'})^{b(t_b+t_r)} \\ x\Big[\frac{b(t_a+t_r)}{E_s-E_s'}\phi(\frac{E_s-E_s'}{E_s})+\frac{\xi}{2(E_s-E_s')^2}\Big]dE_s'\end{aligned} \tag{A.6}$$

where t_a and t_b are the target material thickness after and before scattering respectively. The t_r is the equivalent radiator thickness for the internal radiative corrections. E_{smin}, E_{pmax} and R are given below:

$$E_{smin} = \frac{E_p}{1-\frac{E_p(1-Cos\theta)}{M}} \tag{A.7}$$

$$E_{pmax} = \frac{E_s^{prime}}{1-\frac{E_s'(1-Cos\theta)}{M}} \tag{A.8}$$

$$R = \frac{M-2E_sSin^2(\frac{\theta}{2})}{M-E_pSin^2(\frac{\theta}{2})} \tag{A.9}$$

$$b \approx 1.357 \tag{A.10}$$

$$\xi = \frac{\pi m}{2\alpha}\frac{t_a+t_b}{Z+\eta}ln(183/Z^{1/3}) \tag{A.11}$$

$$\eta = ln(1440Z^{-2/3})/ln(183/Z^{-1/3} \tag{A.12}$$

σ_{eff} is related to the Born cross section by:

$$\sigma_{eff} = F(Q^2)\sigma_{Born}(E_s, E_p) \tag{A.13}$$

where the F factor is all other corrections which are independent of Δ. The F is given below:

$$F(Q^2) = 1 + 0.5772b(t_a + t_b) + \frac{2\alpha}{\pi}\left[\frac{-14}{9} + \frac{13}{12}ln(\frac{-q^2}{m^2})\right] - \frac{\alpha}{2\pi}ln^2(\frac{E_s}{E_p}) + \frac{\alpha}{\pi}\left[\frac{\pi^2}{6} - \phi(Cos^2\frac{\theta}{2})\right] \tag{A.14}$$

where $\phi(x)$ is the Spence function:

$$\phi(x) = \int_0^x \frac{-ln|1-y|}{y}dy \tag{A.15}$$

In the F function, $b(t_a + t_b)$ term is the normalization factor in the external bremsstrahlung, the second term is the vacuum polarization plus the noninfrared part of the vertex correction, the third term is the correction to the peaking approximation in the internal bremsstrahlung and the last term is the Schwinger correction [81]. The biggest contribution comes from the second term in the F factor.

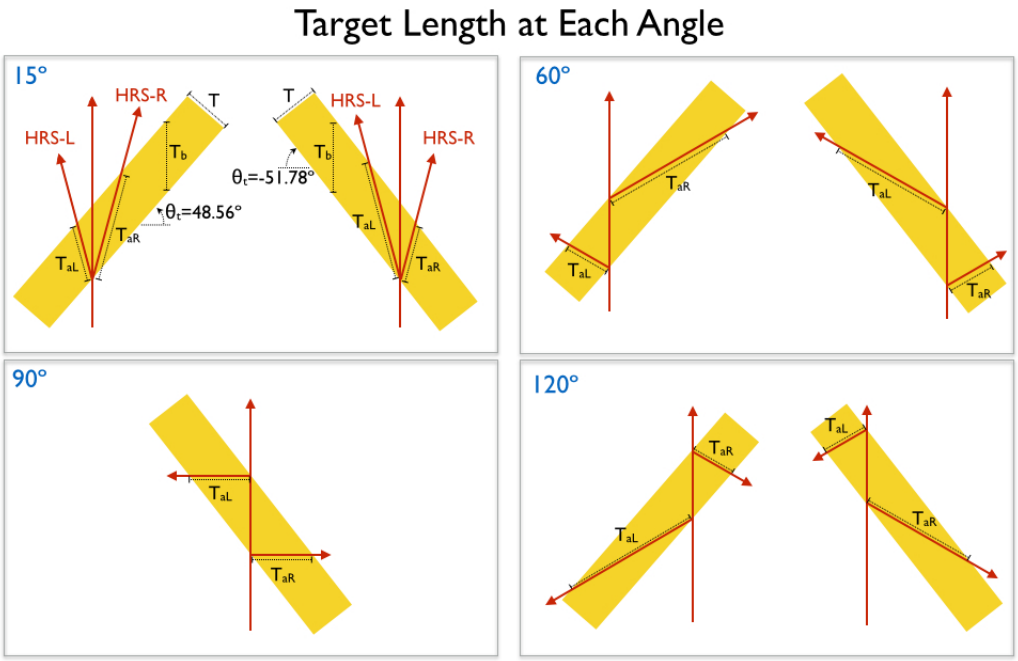

Figure A.5: Calculation of the target thicknesses at each angle for the E05-110 experiment. Figure Yoomin Oh [79]

1/2 Target Length Before/After Scattering at Each Kinematics

HRS angle (degrees)	Target Rotation (θ_{ccw}=48.56°) (θ_{cw}=-51.78°)	$T_b/(2X_0)$ ($\times10^{-3}$)	$T_{aL,R}/(2X_0)$ ($\times10^{-3}$)	$T_b/(2X_0)$ ($\times10^{-3}$)	$T_{aL,R}/(2X_0)$ ($\times10^{-3}$)	@ Beam Energy (MeV)
		^{56}Fe (X_0=13.84 g/cm^2)		^{12}C (X_0=42.70 g/cm^2)		
15	CCW	5.584	4.435 8.333	1.584	1.258 2.354	1260, 2145, 2448, 2845, 3250, 3680
	CW	5.997	9.411 4.632	1.692	2.655 1.307	1646
60	CCW	5.584	3.771 11.61*	1.584	1.069 3.293*	646, 740, 845, 957,1260
	CW	5.997	10.00* 3.749	1.692	2.821* 1.058	1030, 1102
90	CW	5.997	4.723	1.692	1.333	All
120	CCW	5.584	11.61 3.771*	1.584	3.293 1.069*	740
	CW	5.997	3.749* 10.00	1.692	1.058* 2.821	400, 528, 646, 845, 957

$T_{ccw}(^{56}Fe)$ = 0.1023 g/cm^2, $T_{cw}(^{56}Fe)$ = 0.1027 g/cm^2; $T_{ccw}(^{12}C)$ = 0.0895 g/cm^2, $T_{cw}(^{12}C)$ = 0.0894 g/cm2.

* In normal situation t_a gets longer as t_b gets shorter, but at these kinematics, t_a grows as t_b does. See the figures.

Figure A.6: Target thicknesses for E05-110 iron and carbon targets. Figure Yoomin Oh [79]

A.3 Elastic Radiative Corrections

The radiative corrections to the elastic peak is a well-known subject. Schwinger [101–103] calculated the radiative corrections first and found the relation between the measured cross section and the Born cross section to be:

$$\frac{d\sigma}{d\Omega_{exp}} = (1+\delta)\frac{d\sigma}{d\Omega_{Born}} \tag{A.16}$$

where δ is the radiative corrections. In the case where the energy loss $\Delta E \to 0$, $(1+\delta)$ can be replaced by e^{δ} [112] to take into account higher order corrections.

In this analysis the elastic radiative corrections were calculated by the formula of Mo and Tsai which consists of the external and internal terms [93, 94].

The internal term is:

$$\begin{aligned}
\delta_{int} = -\frac{\alpha}{\pi}\Big(&\frac{28}{9} - \frac{13}{6}ln(\frac{Q^2}{m_e^2}) + (ln(\frac{Q^2}{m_e^2}) - 1 + 2Zln(\frac{E_i}{E_f})) \\
&x\Big[2ln(\frac{E_i}{\Delta E} - 3ln(\frac{E_i}{E_f}))\Big] \\
&-\phi(\frac{E_f - E_i}{E_f}) - Z^2 ln(\frac{E_t}{M_t}) + Z^2 ln(\frac{M_t E_f}{E_i \Delta E})(\frac{1}{\beta_t} ln(\frac{1+\beta_t}{1-\beta_t}) - 2) \\
&+\frac{Z^2}{\beta_t}\Big[\frac{1}{2}ln(\frac{1+\beta_t}{1-\beta_t})ln(\frac{E_t + M_t}{2M_t}) - \phi[-(\frac{E_t - M_t}{E_t + M_t})^{} 1/2(\frac{1+\beta_t}{1-\beta_t})^{1/2}]\Big] \\
&-Z\Big[\phi(-\frac{E_t - E_f}{E_f}) - \phi(\frac{M_t(E_t - E_f)}{2E_i E_t - M_t E_f}) + \phi(\frac{2E_i(E_t - E_f)}{2E_i E_f - M_t E_f}) \\
&ln\Big|\frac{2E_i E_t - M_t E_f}{E_f(M_t - 2E_i)}\Big| ln(\frac{M_t}{2E_i})\Big] \\
&-Z\Big[\phi(-\frac{M_t - E_i}{E_i}) - \phi(\frac{M_t - E_i}{E_i}) + \phi(\frac{2(M_t - E_i)}{M_t}) ln\Big|\frac{M_t}{2E_i - M_t}\Big| ln(\frac{M_t}{2E_i})\Big] \\
&+Z\Big[\phi(-\frac{M_t - E_f}{E_f}) - \phi(\frac{M_t - E_f}{E_f}) + \phi(\frac{2(M_t - E_f)}{M_t}) ln\Big|\frac{M_t}{2E_f - M_t}\Big| ln(\frac{M_t}{2E_f})\Big] \\
&+\frac{Z^2}{\beta_t}\Big[\phi[(\frac{E_t - M_t}{E_t + M_t})^{1/2}(\frac{1-\beta_t}{1+\beta_t})^{1/2}] - \phi[(\frac{E_t - M_t}{E_t + M_t})^{1/2}] \\
&+\phi[-(\frac{E_t - M_t}{E_t + M_t})^{1/2}]\Big)
\end{aligned} \tag{A.17}$$

where E_t is the final energy of the target nucleus and ΔE is the E_f cutoff of the elastic tail.

The external term is:

$$\delta_{ext} = -\left[bt_b ln(\frac{E_p^2}{E_s \Delta E}) + bt_a ln(\frac{E_p}{\Delta E})\right] \tag{A.18}$$

where t_b and t_a are the target material thicknesses before and after scattering.

$$\delta = \delta_{int} + \delta_{ext} \tag{A.19}$$

The radiative corrections for the elastic Carbon data was calculated by the equations given above and the results found to be around 30%.

APPENDIX B

KRIGING INTERPOLATION

The Kriging interpolation method is also known as the Gaussian process regression. According to Rasmussen and Williams, *A Gaussian process is collection of random variables, any finite number of which have a joint Gaussian distribution. A Gaussian process is completely specified by its mean function and covariance function [84].*

The Kriging interpolation method was used in this analysis to smooth the LHRS spectra and to fill the gaps in the RHRS spectra. The Kriging interpolation was also used for the Rosenbluth separation to interpolate cross sections at constant $|q|$. The result of the Rosenbluth separation from the Kriging interpolation was used only for comparison with the least square method interpolation.

The Algorithm, which was used in this analysis, is given below [84]:

$input : X(inputs), y(targets), k(covariancefunction), \sigma_n^2(noiselevel), x_*(testinput)$

$L := cholesky(K + \sigma_n^2 I)$

$\alpha := L^T / (L/y)$

$\overline{f}_* := k_*^T \alpha$

$v := L/k_*$

$\mathbb{V}[f_*] := k(x_*, x_*) - v^T v$

$logp(y|X) := -\frac{1}{2} y^T \alpha - \sum_i logL_{ii} - \frac{n}{2} log2\Pi$

$return \quad f_*(mean), \mathbb{V}[f_*](variance), logp(y|X)$

APPENDIX C

QUASI-ELASTIC WORLD CROSS SECTIONS ON ^{56}Fe

The existing experimental cross sections on ^{56}Fe from different experiments are listed as a function of energy loss (ν) below [113]. Each plot shows cross sections at different kinematics for different experiments. The kinematics of the experiments are written on the top of the histogram. The labels on the top of each plot are the Z, A, Energy (GeV), angle (degrees), the 4-momentum transfer at the top of the quasielastic peak (x=1) and the citation, respectively.

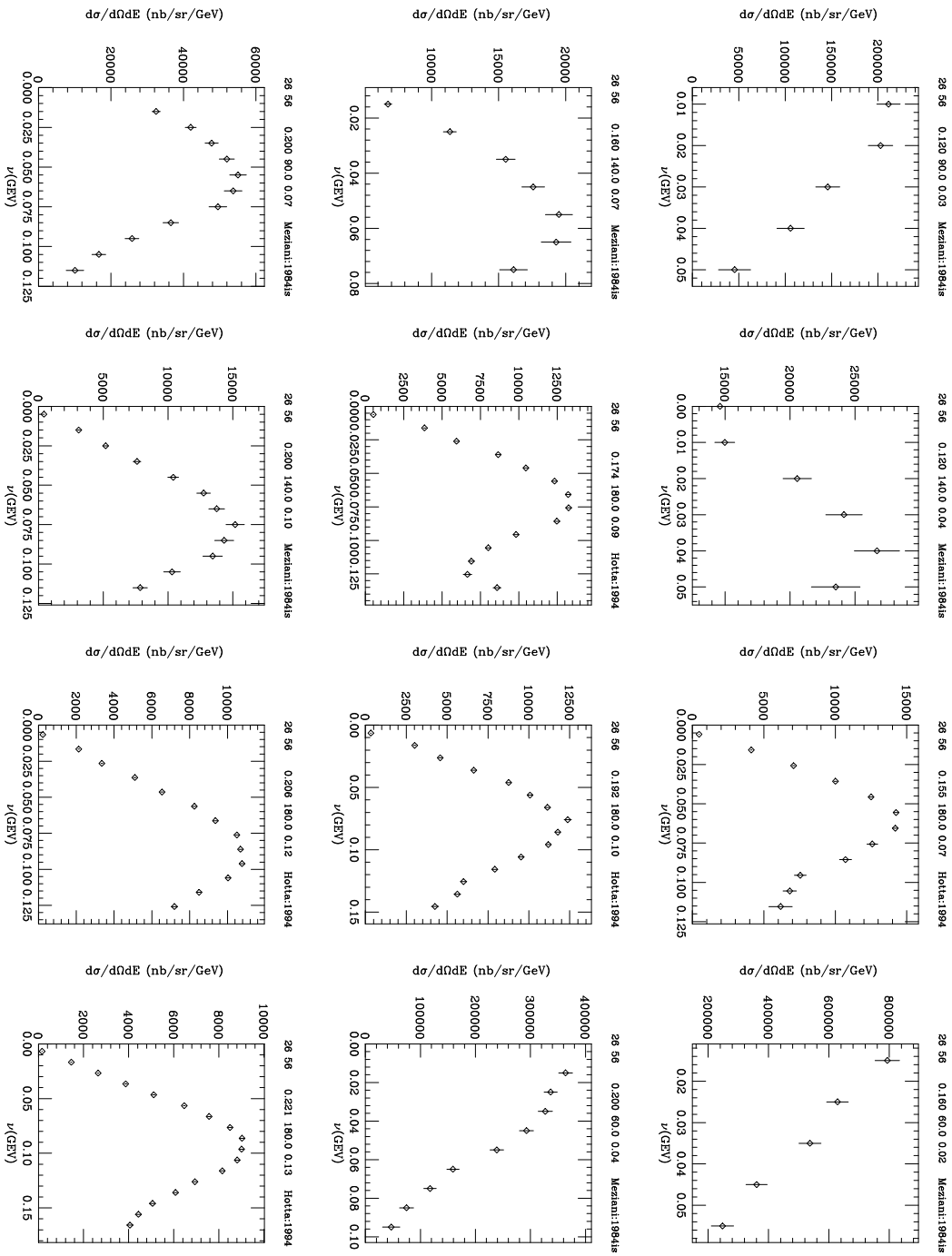

Figure C.1: Quasi-elastic World Cross Sections on ^{56}Fe [113]

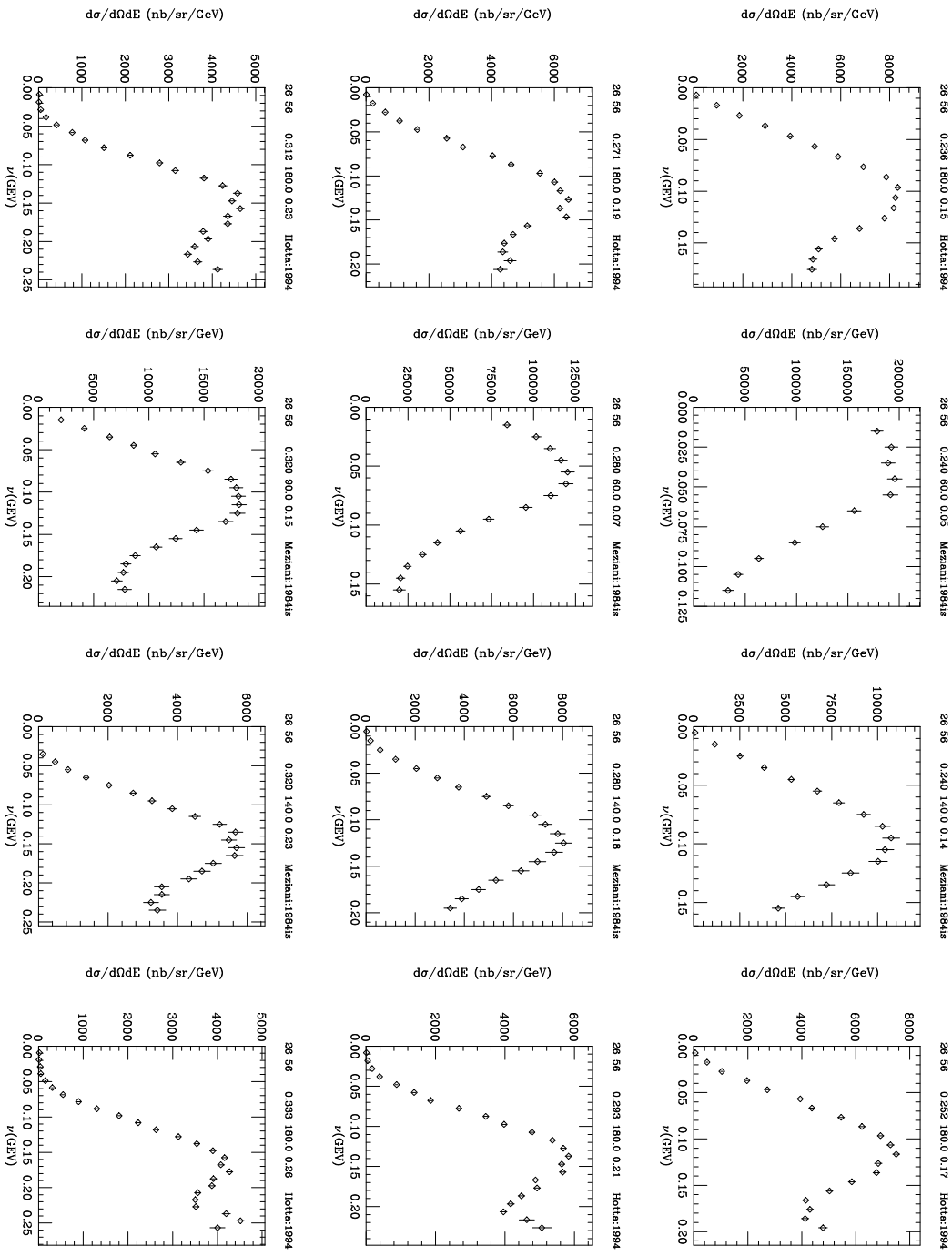

Figure C.2: Quasi-elastic World Cross Sections on ^{56}Fe [113]

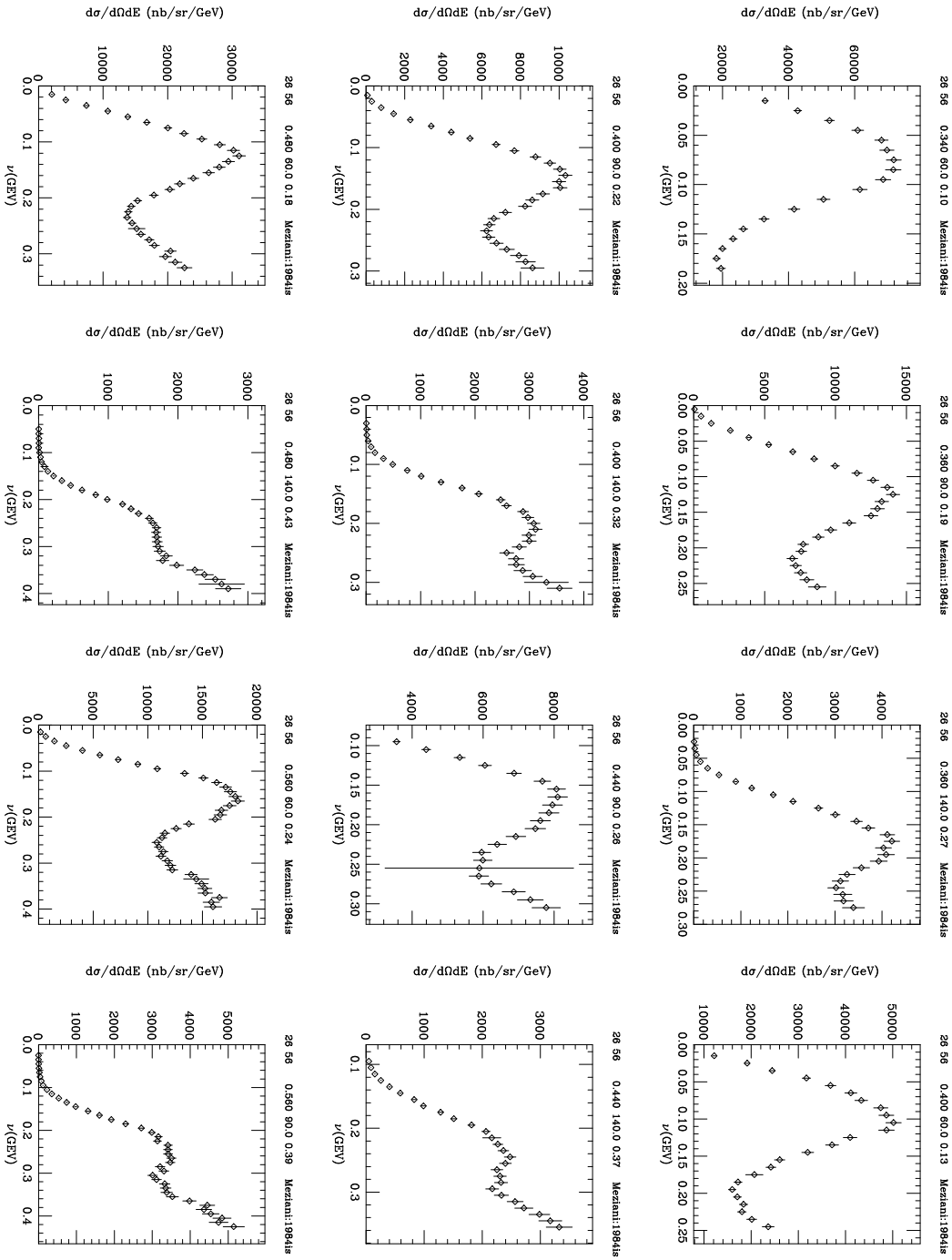

Figure C.3: Quasi-elastic World Cross Sections on ^{56}Fe [113]

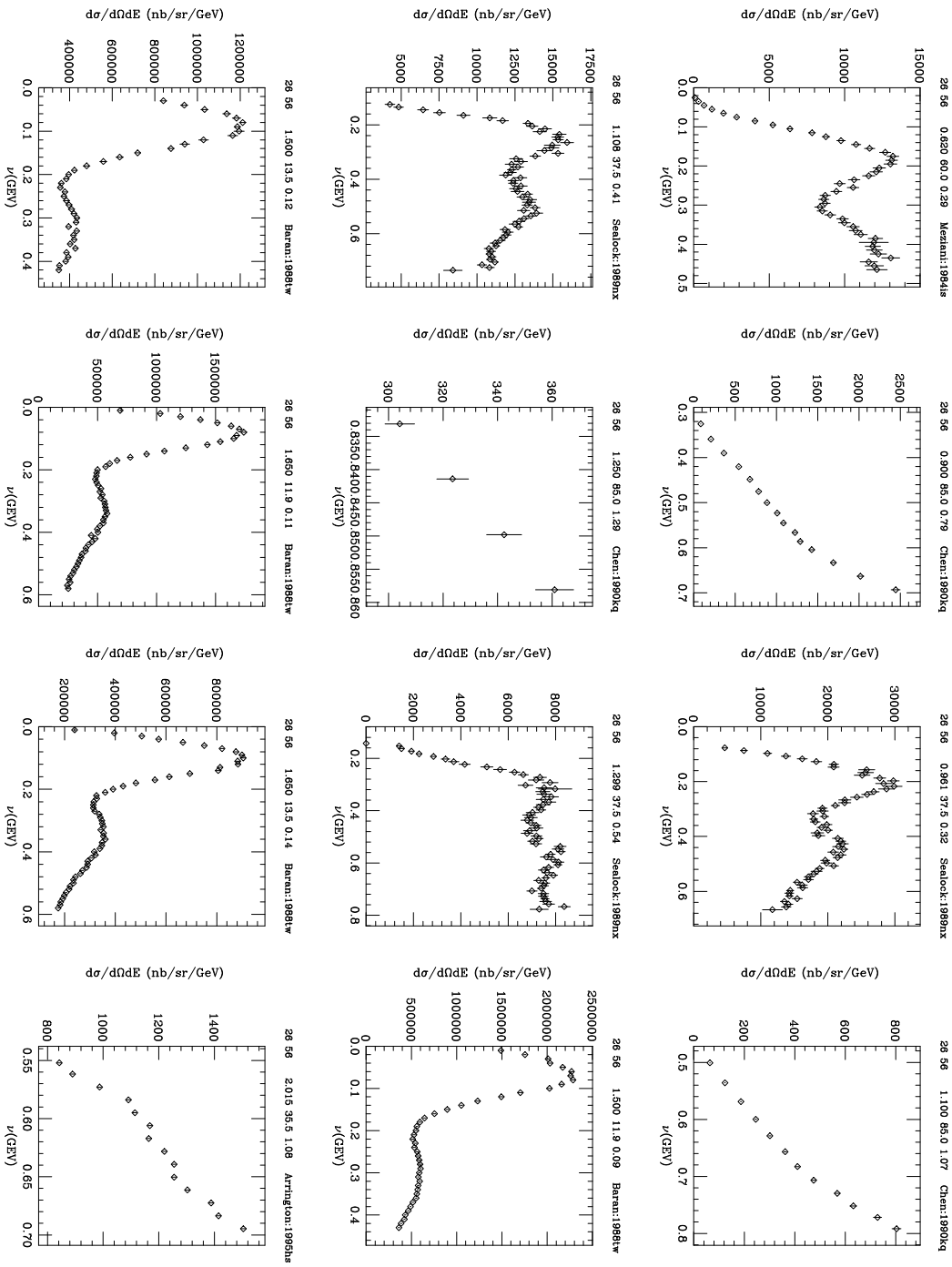

Figure C.4: Quasi-elastic World Cross Sections on ^{56}Fe [113]

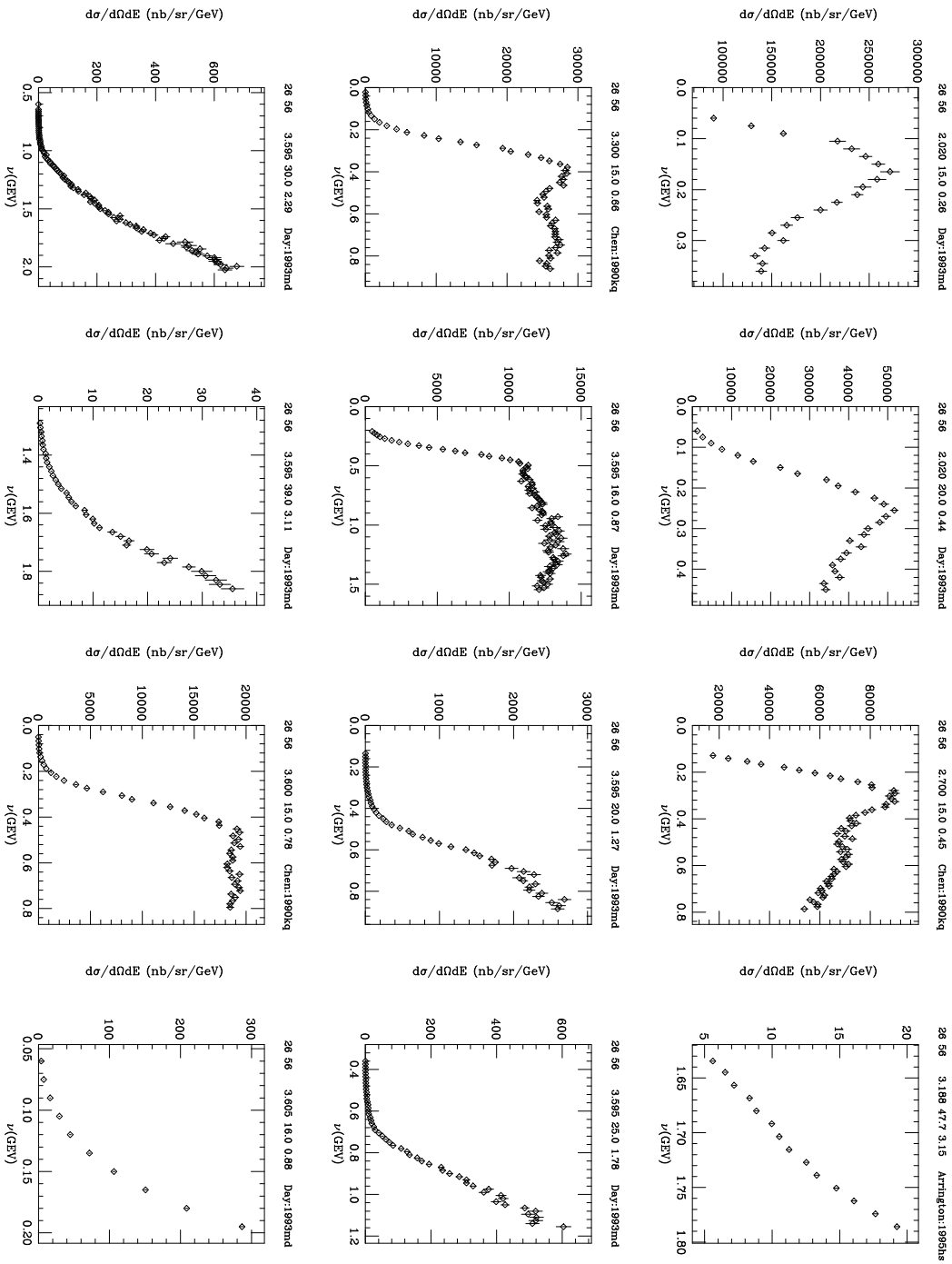

Figure C.5: Quasi-elastic World Cross Sections on ^{56}Fe [113]

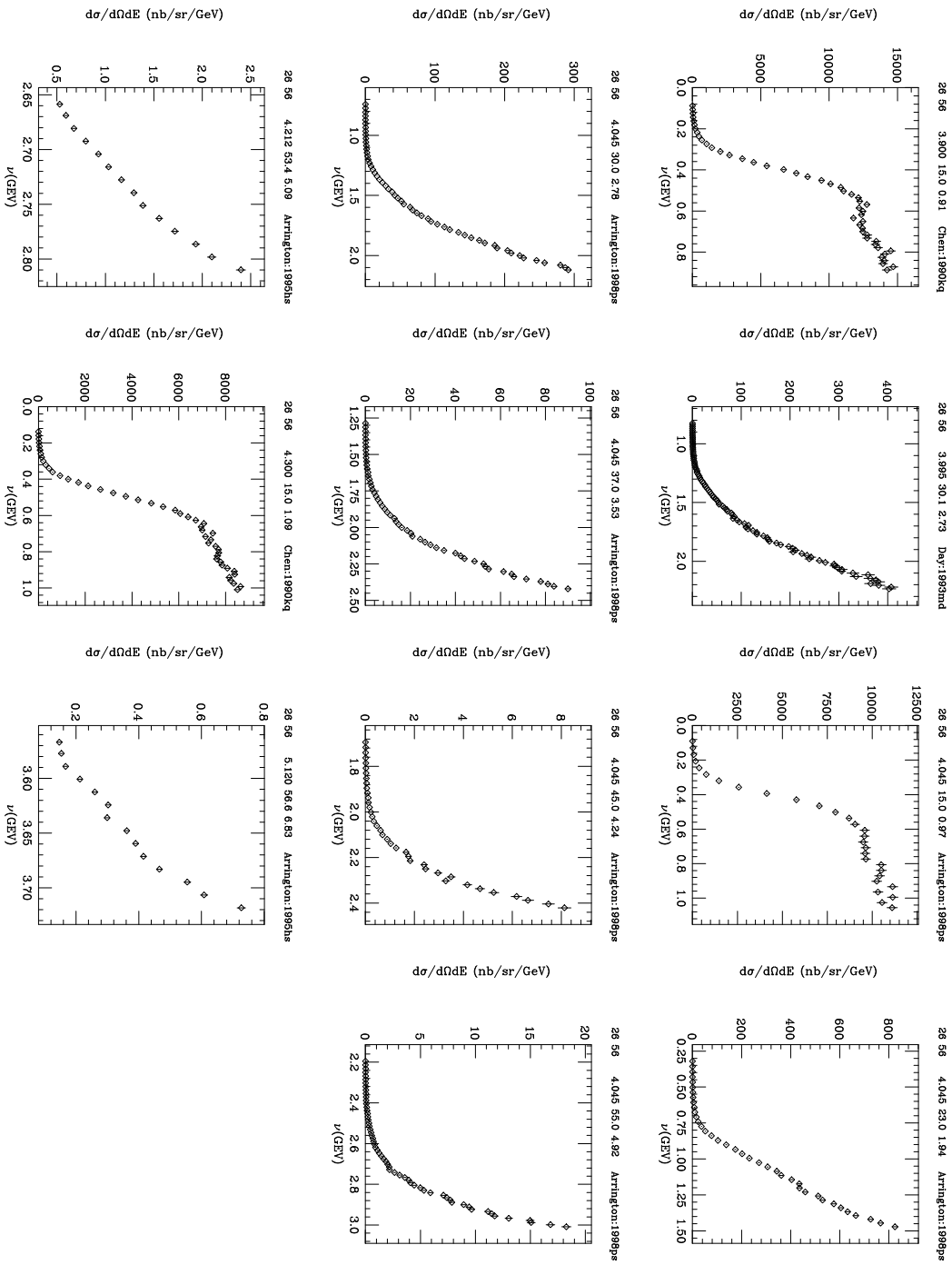

Figure C.6: Quasi-elastic World Cross Sections on ^{56}Fe [113]